UNIWERSYTET ŚLĄSKI W KATOWICACH
WYDZIAŁ MATEMATYKI, FIZYKI I CHEMII

INSTYTUT FIZYKI IM. AUGUSTA CHEŁKOWSKIEGO

KATARZYNA BALIN

REACTION OF EUROPIUM AND SOME TRANSITION METALS DEPOSITED AS ULTRATHIN FILMS

A thesis submitted for the degree of Doctor of Philosophy
in the Faculty of Mathematics, Physics and Chemistry
at University of Silesia

Work done under the supervision of
Prof. dr hab. Jacek Szade

Katowice, 2011

Acknowledgements

I would like to express my sincere gratitude to my supervisors Prof. dr hab. Jacek Szade and Prof. Zbigniew Celinski for their support and useful criticisms during my PhD. Special gratitude for introducing me the world of surface science and thin film physics and providing broad perspectives of scientific development. Their advices, attention and patience had been invaluable and much appreciated.

I owe my deepest gratitude to Prof. A. Gibaud for the possibility of carrying out the X-ray diffraction measurements at Condensed Matter Physics Laboratory of University of Main. The work described in this thesis could not have been done without the assistance of Anna Nowak who performed the X-ray diffraction studies. I would also like to extend appreciations to all members of the Center for Magnetism and Magnetic Nanostructures at University of Colorado at Colorado Springs especially to Andrew Hutchison and Ian Harward for the precious advices and technical support at the beginning of my research. I am indebted to all members of the Solid State Physics Department, in particular dr A. Chrobak and dr A. Guzik for their help in SQUID measurements.

This work was supported by National Science Foundation grants (DMR0605629 and DMR0907053), I also sincerely thank the University of Silesia for awarding me the "UPGOW" scholarship.

Abstract

Formation of rare earth (RE) and transition metal (TM) binary compounds, RE_xTM_y, with different stoichiometry is well known [1]. Such compounds have been extensively studied during the last two or three decades, especially their magnetic properties. These compounds are interesting not only from a basic physics point of view but also from an applications standpoint. Certain important features occur in RE_xTM_y thin films, such as large perpendicular magnetic anisotropy, a high Curie temperature, and a high coercive field makes these materials a promising candidate for potential applications in magneto-optical recording and/or permanent magnets used in on-wafer actuators and sensors.

The aim of our work was to examine, over a wide range of Eu-TM (TM = Mn, Fe, Cr) concentrations, formation of ordered compounds or alloys in the form of thin films, and to determine their basic physical properties. A Molecular Beam Epitaxy systems equipped with XPS and RHEED, were used to prepare Eu-TM films. A series of 2-30nm thick Eu-TM films have been grown at room temperature by co-deposition or in multilayers form on MgO, GaAs or Si substrates with a 50 nm thick Mo buffer layer. We carried out electronic and crystallographic characterization of their properties using X-ray photoemission spectroscopy (XPS) and diffraction measurements. The magnetic and transport properties were investigated with the help of a SQUID magnetometer and a 4-point probe over a wide temperature range.

Relative changes in the Eu 4*d*/(Mn, Fe, Cr) 2*p* photoemission line area ratio, as well as chemical shifts of core levels monitored during the annealing process indicate mixing between europium and transition metals. The intermixing of the layers was also confirmed by the XRR measurements, where a formation of the uniform film from the point of view of electronic density was observed. The diffraction measurements indicate that the mixing of Eu-TM layers was the most efficient for the Eu/Mn system where a new Eu-Mn compound has been formed - $EuMn_2$ exhibiting magnetic ordering at temperatures below 40K. Indication of formation of additional two intermetallic phases was found in the Eu-Mn system. The magnetic properties of Eu-Mn and Eu-Cr systems result mainly from the occurrence of divalent europium in samples, whereas in the case of the Eu-Fe system they are dominated by the presence of iron aggregated probably in nanoparticles.

Contents

1. Introduction

1.1 General introduction

Over the last few decades the thin films became very important branch of material science and technology. The thin films, within the meaning of low-dimensional systems or in more precise meaning the layers of a material with the thickness of nanometers or less, will be the subject of this work. An increasing interest in thin films is determined mainly by their possible applications resulting from the properties of the thin films. The discovery of the new materials, phenomena and improvement of experimental techniques allowed for the development of new nanostructured, advanced materials. The electrical, magnetic, optical, thermal or mechanical properties of thin films are different when comparing to the corresponding bulk materials and usually are strongly influenced by the surface and the interface effects. Unique, characteristic for thin films properties and phenomena have been observed and already applied in variety of devices. Giant and tunnel magnetoresistive effect [1, 2], the exchange bias [3, 4, 5] or perpendicular magnetic anisotropy [6, 7] are among the most important effects.

The ability for engineering advanced materials, such as thin films, with desired properties and specific functionality, is the main goal of many investigations and allows to extensive use of that kind of materials in many different fields. Therefore nowadays three important areas: the thin film fabrication, their characterization and exploration for further applications have been intensively developed. Modern growth techniques, such as Molecular Beam Epitaxy, Sputtering techniques, Chemical Solution Deposition (Sol-Gel), Pulsed Laser Deposition allow for precise and controlled fabrication of the thin films. Nevertheless the choice of technique depends more likely on kind of desired structure. In this work, for the fabrication of high quality and high purity layers, the Molecular Beam Epitaxy (MBE) technique was

applied, mainly due to strong influence of the growth condition on the properties of deposited film. Therefore, characteristic for the MBE, precise control of surface composition and morphology, low growth rate, low growth temperature, *in-situ* control of crystal growth at atomic level had a crucial influence on the choice of this method.

Characterization of fabricated films can be realized through the use of different methods. Starting from the microscopic imaging of the surface of the film where optical microscopy, Scanning Electron Microscopy (SEM), Scanning Probe Microscopies (Scanning Tunneling Microscopy - STM, Atomic Force Microscopy - AFM) can be applied. Across techniques which allow to characterize the internal structure of the film such as the Reflection High Energy Electron Diffraction (RHEED) or X-ray diffraction (XRD). Through spectroscopic techniques used to determine the elemental composition or chemical states of the film, among which the X-ray Photoelectron Spectroscopy is in the forefront. Or even through techniques for determining the optical, mechanical, magnetic or electrical properties of the film.

Determination of the nature and properties of novel, advanced materials in the thin film form can be used for the development of new devices or new technologies for future applications. As the result of earlier investigations the thin films can be and are used as an integral part of many products or devices in various kinds of applications such as in microelectronics, optics (as anti-reflection coatings), data storage, read-heads of modern hard disk drives, magnetic sensors, gas sensors, protection communication, optical electronics, catalysis, corrosion protection, energy generation and many other purposes.

We found the Eu-TM system as a good candidate for extensive research containing both: fabrication in a thin film form advanced, novel materials and characterization of its physical properties.

The thesis is divided into four sections. The first section – Introduction includes the literature review of the Rare Earth (RE) and Transition Metals (TM) binary compound, also the motivation and the scope of the research will be here introduced. In the second section experimental details will be presented, this chapter contains description of both film preparation and applied research techniques. Experimental results will be presented and discussed in third part of this thesis; this chapter will be divided into separate sections where the Eu-Mn, Eu-Fe, and Eu-Cr systems will be respectively considered. In the last part the partial conclusions will be collected and common summary will be presented.

1.2 Review of the rare earth – transition metals binary compounds

Formation of rare earth (RE) and transition metal (TM) binary compounds, RE_xTM_y, with different stochiometries is well known [8]. RE_xTM_y compounds, with different stoichiometries have been extensively studied during the last decades, especially from the point of view of their interesting magnetic properties [9-13]. These kinds of compounds are interesting not only from a basic physics point of view but also from an applications standpoint. Certain important features occurring in RE_xTM_y thin films, such as large perpendicular magnetic anisotropy[14, 15], a high Curie temperature, and a high coercive field [16] make these materials a promising candidate for potential applications in for example magneto-optical recording, hydrogen storage, or even permanent magnets used in on-wafer actuators and sensors.

Crystallographic structures of the RE-TM known bulk compounds will be presented. Described in this part crystal structures, of known rare earth-*3d* transition metal bulk compounds, are typical for rare earth-transition metal compounds. The information about compositions and crystallographic structures of known RE-TM binary compounds have been collected in Table 1, formation of stable bulk compound have been marked with a star (★).

The typical feature for all structures, due to some geometrical and energetical restrictions, is formation of closely packed structures. Due to this fact there are certain characteristics which enable grouping and classifying of RE-TM compounds. The RE-TM compounds may be classified for example according to the percentage content of RE or TM elements (see Table 1), in such case few different groups can be mention: (a) compounds rich in Rare Earth – RE more than 50 at %, (b) compounds having strong directional bonds, such as $RCo_{1-\delta}$, and R_2Co_3, (c) compounds rich in *3d* transition metals - TM between 66 at % and 90 at %, compounds having more than 90 at% TM. Common feature for the group (a) is formation of trigonal prisms with one RE atom at each corner, where TM atoms are the centers of the prism. The kind of realized TM-TM linkage in this group: isolated atoms (RE_3TM, RE_5TM_2, RE_7TM_3), pairs and groups of TM atoms (RE_8TM_5, Er_3Ni_2), chains of 4TM atoms (Yb_3Co_2, Dy_3Ni_2), infinite chains (TbNi) is other important feature in this group. But in this work the attention was mostly paid to the group (c) which consist the largest number of compounds and which can be obtained by alternate stacking of $RETM_2$ and $RETM_5$ layers.

Table 1 Compounds appearing in RE-TM systems and their crystal structures [17].

RE_xTM_y	TM at.%	CRYSTAL STRUCTURE	SPACE GROUP	RARE EARTH	TRANSITION METAL				
					Mn	Fe	Co	Ni	Zn
RE_3TM	25	orthorhombic	Pnma	RE			★	★	
RE_5M_2	28.6	monoclinic	C2/c	Pr,Nd,Sm			★		
RE_7TM_3	30	hexagonal	$P6_3mc$	La, Ce, Pr, Nd				★	
		monoclinic	$P2_1/c$	Gd, Tb, Dy, Ho, Er			★		
$RE_{12}TM_7$	36.8	trigonal	R-3	Ho, Er				★	
		monoclinic	C2/m	Tb, Dy, Ho				★	
RE_4TM_3	42.8	hexagonal	$P6_3/m$	Gd, Tb, Dy, Ho, Er, Tm, Lu,			★		
		orthorhombic	Pnma	Tb, Dy, Ho, Er, Tm, Yb, Lu				★	
RETM	50	cubic		RE					★
		monoclinic	$P2_1/c$	Tb				★	
RE_2TM_3	60	orthorhombic	Cmca	La			★	★	
		cubic	Fd3m	RE		★	★	★	
		cubic	Fd3m	Gd, Tb, Dy, Ho	★				
$RETM_2$	66.6	orthorhombic		RE					★
		hexagonal	$P6_3/mmc$	Pr, Nd, Sm, Ho, Er, Tm, Lu	★				
		hexagonal	$P6_3/mmc$	Ce				★	
		trigonal	R-3m	Sm, Gd, Tb, Dy, Ho, Er, Tm		★			
		trigonal	R-3m	Ce, Pr, Nd, Sm, Gd, Tb, Dy, Ho, Er, Tm, Yb, Lu			★		
$RETM_3$	75	trigonal	R-3m	La, Ce, Pr, Nd, Sm, Gd, Tb, Dy, Ho, Er, Tm, Yb,				★	
		orthorhombic		Ce, Pr, Nd, Sm, Eu, Gd, Tb, Dy, Ho, Er, Tm, Lu					★
		trigonal	R-3m	La, Ce, Pr, Nd, Sm, Gd			★		
RE_2TM_7	77.7	trigonal	R-3m	Pr, Nd, Sm, Gd, Tb, Dy, Ho, Er				★	
		hexagonal	$P6_3/mmc$	La, Ce, Pr, Nd, Sm, Gd, Tb, Dy				★	
RE_5TM_{19}	79.2	trigonal	R-3m	La, Ce, Pr, Nd			★		
		hexagonal	$P6_3/mmc$	Sm			★		
RE_6TM_{23}	79.3	cubic	Fm3m	Nd, Sm, Gd, Tb, Dy, Ho, Er, Tm, Yb, Lu	★				
		cubic	Fm3m	Gd, Tb, Dy, Ho, Er, Tm, Yb, Lu		★			
$RETM_5$	83.3	hexagonal	P6/mmm	RE			★	★	
		hexagonal	P6/mmm	La, Ce, Eu, Gd, Dy, Ho, Er, Lu					★
		trigonal	R-3m	Ce, Pr, Nd, Sm, Gd, Tb		★	★		
		trigonal	R-3m	Dy, Ho			★		
		hexagonal	$P6_3/mmc$	Ce, Gd, Tb, Dy, Ho, Er, Tm, Yb, Lu		★			
RE_2TM_{17}	89.5	hexagonal	$P6_3/mmc$	Ce, Sm, Gd, Tb, Dy, Ho, Er, Tm, Yb, Lu			★		
		hexagonal	$P6_3/mmc$	RE				★	
		hexagonal	$P6_3/mmc$	Ce, Pr, Nd, Sm, Eu, Gd, Tb, Dy, Er, Tm, Yb, Lu					★
$RETM_{12}$	92.3	tetragonal	I4/mmm	Nd, Gd, Tb, Dy, Ho, Er	★				
		tetragonal	I4/mmm	Sm, Gd, Tb, Dy, Ho, Er, Tm					★
$RETM_{13}$	92.9	cubic	Fm3c	La			★		★
		tetragonal	I4/mmm	Yb					★

Figure 1 represents the relation between the crystallographic structures (group c) of the different known RE-TM compounds. As it can be seen if in the cubic close packed structure (Cu) of a *3d* metal two specific TM atoms are replaced by an RE-atom, a cubic $RETM_2$ structure is formed (*$MgCu_2$*-type). A different stacking sequence results in the hexagonal *$MgZn_2$* structure which is formed with some $RETM_2$ compounds ($REMn_2$ where R = Sc, Pr, Nd, Sm, Er, Tm and Lu).

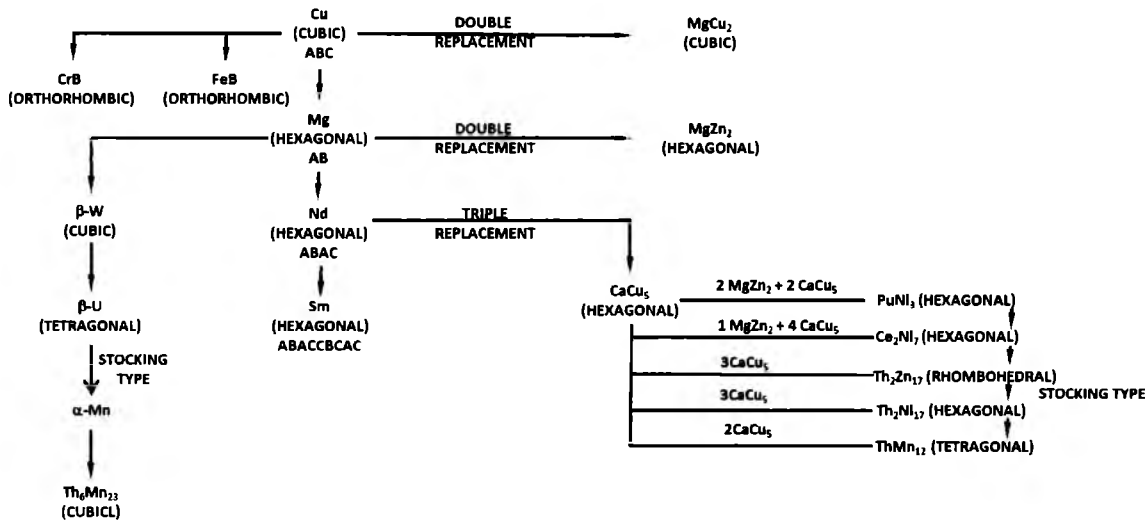

Figure 1.1 The relation between the structures of the various RE-TM compounds. (18)

If in a hexagonal close packed 3d-metal basis lattice instead of three 3d atoms one RE-atom is fitted in, then the structure of the $RETM_5$ compounds is formed (*$CaCu_5$*-type). As it is realized for example in the RE(Ni, Co) systems. The majority of other RE-TM structures rich in TM atoms can be deduced from that *$CaCu_5$* structure.

- The $PuNi_3$ structure is formed when two *$CaCu_5$* layers and two *$MgZn_2$* layers are put above each other. This structure is observed in RE compounds with Fe, Ni, Co.
- The RE_2Co_7 compounds can be formed from nine *$CaCu_5$* cells placed one above the other.
- In a similar style, by the combination of *$CaCu_5$* cells, the structures of *Th_2Zn_{17}* and *Th_2Ni_{17}* can be formed. The *Th_2Ni_{17}* is formed by a layering of three *$CaCu_5$* layers, but with a c-axis doubled.
- Similarly the structures with the composition RE_2TM_7 can be build up.
- Also the $RETM_{12}$ compounds (crystallized in *$ThMn_{12}$* structure type) can be deduced from the *$CaCu_5$* type by a combination of two basis lattices of the *$CaCu_5$* structure.

The structure type *Th_6Mn_{23}*, observed for example in RE-Mn and RE-Fe systems, is another type of structure which is important for the RE-TM intermetallic compounds. This structure cannot be deduced from the *$CaCu_5$* structure, it can be formed by multiple replacements of TM atoms as occurs for example in the case of RE_6Mn_{23} where the multiple replacements begin form the α-Mn cell. In this structure the RE-atoms possess one crystallographically equivalent atom position, while four groups of TM possess four different crystallographic atomic positions.

Also the compounds of the type *CrB* and *FeB* are observed in the RE-TM systems, for example in RE-Ni system. These structures can also be deduced from the cubic close packed structure. Both *Th_6Mn_{23}* and *CrB* or *FeB* structure types can be considered as close packed structures and can be deduced from closed packed hexagonal *Mg* or cubic *Cu* structure type.

Table 2 summarizes the crystallographic data for selected RE-TM compounds; particular attention was paid to the compounds of transition metals with europium.

Table 2 Summary of crystallographic data for selected compounds [19].

	RE-TM	Structure type	Space group	Lattice parameter [nm]
RE_2TM	$CuEu_2$			
RETM	EuCu	ClC_8	Pm-3m (221)	a=0.3479
	EuZn	ClC_8	Pm-3m (221)	a=0.3808
	CuGd	ClC_8	Pm-3m (221)	a=0.3502
	CuGd	ClC_8	Pm-3m (221)	a=0.353
$RETM_2$	Cu_2Eu	$CeCu_2$	Immm (74)	a=0.4434; b=0.7250; c=0.7553
	$EuZn_2$	$CeCu_2$	Imma (74)	a=0.4728; b=0.7650; c=0.7655
	$EuNi_2$	$MgNi_2$	$P6_3/mmc$ (194)	a=0.5390; c=1.749; γ=120
	$EuFe_2$	$MgZn_2$	$P6_3/mmc$ (194)	a=0.5889; c=0.9624; γ=120
	Cu_2Gd	$CeCu_2$	Imma (74)	a=0.4328; b=0.6878; c=0.734
	Cu_2Sm	$CeCu_2$	Imma (74)	a=0.4355; b=0.6929; c=0.372
	$DyMn_2$		Fd-3m (227)	a=0.759
	$GdMn_2$		Fd-3m (227)	a=0.7758
$RETM_5$	Cu_5Eu	$CaCu_5$	P6/mmm (191)	a=0.5180; c=0.4070; γ=120
	$EuNi_5$	$CaCu_5$	P6/mmm (191)	a=0.492; c=0.3961; γ=120
	$EuZn_5$	$CaCu_5$	P6/mmm (191)	a=0.5454; c=0.4285; γ=120
	Cu_5Gd	$CaCu_5$	P6/mmm (191)	a=0.5036; c=4102; γ=120
$RETM_6$	$GdCu_6$		Pnma (62)	a=0.8315; b=0.5983; c=0.9949
	Cu_6Sm		Pnma (62)	a=0.806; b=0.5034; c=1.049
RE_2TM_{17}	Eu_2Ni_{17}	$Ni_{17}Th_2$	$P6_3/mmc$ (194)	a=0.835; c=0.806; γ=120
	$Cu_{12}Sm_2$		R-3m (166)	a=0.9; c=1.204; γ=120
$RETM_{11}$	$EuZn_{11}$	$BaCd_{11}$	$I4_1/amd$ (141)	a=1.072; c=0.6877; γ=120
$RETM_{12}$	$GdMn_{12}$		I4/mmm (139)	a=0.872
$RETM_{13}$	$EuZn_{13}$	$NaZn_{13}$	Fm-3c (226)	a=1.2216
$RETM_{28}$	$EuMn_{28}$	Mn	I-43m (217)	a=0.899

The electronic structure of the RE-TM system is the next important subject of extensive research. Interesting properties of RE-TM compounds results from the presence in the compounds of both $4f$ and $3d$ atoms. The existence of localized electrons with low binding energy gives rise to interesting magnetic properties and many-body phenomena that are heavily influenced by the presence of surfaces and interfaces.

In case of RE-TM intermetallic compounds a crucial role is played by the phenomena of valance fluctuation but also heavy fermion properties resulting from the interaction between highly correlated f electrons and delocalized conduction electrons. To obtain valuable information such as the valence or possible surface valance transitions of the elements the study of core levels via X-ray photoelectron spectroscopy (XPS) is fundamental.

The phenomena of surface valance transition especially in thin film physics is of great interest of many research. Johansson [20] calculated the surface valence states for the rare earth elements, and found out that a divalent surface is more favorable than a divalent bulk. The surface valance transitions, caused by decrease of cohesive energy due to reduced coordination at the surface as compared to the bulk, was firstly observed by Wertheim and Crecelius [21] as a existence of divalent surface layer of samarium ions on the top of the trivalent Sm metal. For Sm pure metal, the trivalent $4f^5$ bulk configuration is paramagnetic, while the divalent $4f^6$ surface configuration is diamagnetic [21, 22]. The same effects appeared for many trivalent and mixed-valent compounds of Sm, Tm, and Yb.

Similarly for the europium; in the pure metallic state Eu atoms reveal a divalent $4f^7$ configuration (see Table 3 where the total angular momentum J and gyromagnetic ratio g have been given for selected RE) - both in the bulk and on its surface. However, considering intermetallic compounds or other alloys where europium is in trivalent state $EuPd_3$, $EuPd_5$, $EuNi_5$, EuF_3, $EuPt_5$ the surface accordingly to Johansson's calculation is divalent [23, 24, 25].

Table 3 Theoretical ionic properties for selected trivalent rare earths.

	Pm^{3+}	Sm^{3+}	Eu^{3+}	Eu^{2+}	Gd^{3+}
Ground state	$^5I_4$	$^6H_{5/2}$	$^7F_0$	$^8S_{7/2}$	$^8S_{7/2}$
J	4	5/2	0	7/2	7/2
g	3/5	2/7	-	2	2

Both electronic and crystallographic structures; including the distances between atoms or the symmetry properties of the position of a single atom play an important role in understanding the further properties of the material. In particular **the magnetic properties** of the material

are strongly correlated with its electronic and crystallographic structure. Depending on the type of rare earth, the binary compounds RE_xTM_y exhibit different types of magnetic ordering such as antiferromagnetism ($NdMn_2$, $EuZn_5$), ferrimagnetism (Sm_2Co_{17}), ferromagnetism ($DyMn_2$), or more complicated magnetic ordering types [26-29]. The magnetic properties of binary intermetallic compounds between rare earth and transition metals is rather complex but have been intensively studied mostly because of the possibility of their use in various technical applications.

In case of intermetallic RE-TM compounds different types of magnetic moments and interactions between them must be considered. In RE-TM intermetallic compounds three principal types of interaction can be distinguished; the RE-RE interaction, TM-TM and RE-TM. The magnetic interactions between RE ions are rather weak, arise by means of indirect interactions and take place through the conduction electrons (RKKY).

The magnetic moments of TM atoms are rather sensitive to their environment, the electron concentration, as well as to the magnetic interactions in the system. Exchange interaction between the rare-earth and the transition-metal moments is particularly important for the magnetic properties of these compounds. Additionally, a magnetic frustration, resulting from the crystallographic structure or magnetic interactions can be observed in some of the RE-TM systems [30]. Consequently, a large variety of magnetic behaviors in the RE-TM system can be seen:

- Compounds where the 3*d* transition metal atoms do not carry a magnetic moment. Here two possibilities can be realized:
    - When RE atom is nonmagnetic, the compounds are Pauli paramagnets. Such behavior exhibit for example YCo_2, $LuCo_2$, YNi_5, YNi_2 compounds,
    - When the RE atoms carry a magnetic moment, the compounds can be ferromagnetic, antiferromagnetic, or show more complex magnetic structure,
- Compounds in which the magnetization of TM elements is driven by the 4*f* rare earth magnetic moment
    - The class of RCo_2 compounds is one of good representatives of this group. Here Co magnetic moment can be induced or via an external magnetic field, or via substituting, for example Lu or Y in paramagnetic (Lu, Y)Co_2 by a magnetic rare earth. In such system the crystallographic structure is not being changed but the magnetic properties will be determined not only by local

effects upon the magnetic 3*d* ions but can also be described by an average electronic parameter such as the density of states at the Fermi level.

- Compounds with a strange magnetic behavior.
    - For example the Y_9Co_7 at low temperatures is a superconductor and at higher ones is a ferromagnet
- Compounds in which TM atoms have a magnetic moment sustained by the 3*d* band.
    - This class contains the greatest number of RE-TM compounds. These systems may be ordered ferromagnetically, ferrimagnetically, or show a more complex type of magnetic ordering.

Among RE-TM systems, compounds with the manganese – RE-Mn have been widely studied in terms of the type of rare earth, or the arrangement of the Mn atoms in the lattice, and how these variables impact the magnetic properties. For example, compounds with stoichiometry $REMn_2$ for RE = Y, Yb, Lu are paramagnetic, for RE = Pr, Nd, Sm, Gd, Tb are antiferromagnetic and for RE = Gd, Tb, Dy, Ho, Er, Tm are ferromagnetic [31]. The magnetic properties of RE_xMn_y also strongly depend on the distance between manganese atoms, where the critical value of Mn-Mn distance is 2.67Å [32]. For compounds with Mn-Mn distance smaller than the critical value, additional antiferromagnetic interaction was observed.

In RE–Fe binary alloys, the Curie temperature is influenced by the kind of RE atoms through the interaction between RE and TM elements which is proportional to the magnitude of RE spin. The Curie temperature is the highest for Gd-Fe with the largest RE spin, and it decreases in the order of Tb-Fe, Dy-Fe. Interesting properties presents also a class of RE_2Fe_{17} compounds; Lu_2Fe_{17}, shows a transition, upon raising the temperature, from ferromagnetism to helimagnetism [33,34, 35]. For Y_2Fe_{17} a collinear spin structure is observed [33]. Ce_2Fe_{17} is a helimagnet below the ordering temperature but, in contrast to Lu_2Fe_{17} it does not become ferromagnetic at low temperatures. As in case of manganese the Fe-Fe distances and number of nearest neighbors appears to strongly influence the exchange interactions in the RE_2Fe_{17} system.

Complexity, within the meaning of the variety of compounds with a different stoichiometries, in the RE-Tm system increase further when taking into consideration the RE-TM not as a bulk compounds but as a thin films. Here detailed understanding of surface phenomena in addition to understanding the magnetic properties of bulk RE-TM compounds may explain occurring phenomena.

1.3 Motivation and Scope

Rather chemically active europium was chosen as a good candidate for the study of binary RE-TM system in the thin film form. Formation of stable bulk compounds between Eu and variety of elements is well known; $EuRh_5$, $EuNi_5$, $EuPd_5$, $EuPt_5$, $EuCu_5$, $EuAg_5$ [36], $EuAg_5$, $EuRh_2$, $EuPd_5$, $EuPt_5$ [37], EuPd, $EuAg_5$, $EuAu_5$, $EuPd_3$, $EuPt_5$ [38], $EuNi_2$, $EuNi_5$, Eu_2Ni_{17} [b5], Eu_2O_3 [39], EuS, EuSe, EuTe [40] etc. Europium may exist in two valence states, Eu^{2+} or Eu^{3+}. Metallic europium is divalent. Europium in alloys or intermetallic compounds may be in a divalent, trivalent or intermediate-valence state [41]. Moreover, a mixed valency state has also been found in many other RE-TM intermetallic compounds [42, 43].

Europium is also an example of rare earth for which magnetic properties are directly connected to its valency state (see Table 3). There is a noticeable difference in the magnetic properties of europium in the two different valency states Eu^{3+} or Eu^{2+}. Eu^{3+} is non-magnetic ($J = 0$) while the Eu^{2+} has a large pure spin moment ($J = 7/2$). The possibility of switching between the non-magnetic and the magnetic states is also a justification for conducting studies of those systems. Especially nowadays, when microelectronic devices, based on controlling of the charge of electrons, are being replaced by devices which specifically exploiting spin properties instead of or in addition to charge degrees of freedom [44]. Consequently Eu-based structures, which would exhibit described above desired properties, may be applied into new classes of spin-based sensor, memory or logic devices.

Formation of stable bulk compounds between europium and few of the *3d* metals such as Zn, Cu and Ni (see Table 2, Appendix E) is well known. Also some limited reports about $EuFe_2$ compound can be found in the literature [45, 46]. The lack of stable bulk compounds between europium and majority of elements in group of transition metals is rather surprising taking into account high chemical activity of Eu and formation of compounds between other rare earths and the transition metals (see Table 1 and Table 2). From the binary diagrams (see Appendix E) for the Eu-(Cr, Fe, Mn) bulk systems, one can conclude that there is no solubility of the europium in chromium, iron or manganese and vice versa at the temperatures below 800K.

All these properties motivated our study of Eu based intermetallic alloys.

The aim of this work was to examine, over a wide range of Eu-(Mn, Fe, and Cr) concentrations, the formation of ordered compounds in the form of thin films, and to determine some of their physical properties.

We decided to use a Molecular Beam Epitaxy system to prepare Eu-(Mn, Fe, and Cr) compounds assuming that structural effects at interfaces in a multilayer system may be helpful in formation of new phases. We carried out electronic and crystallographic characterization of their properties using *in situ* Reflection High Energy Electron Diffraction, *in situ* X-ray photoemission spectroscopy (XPS) and later after the reaction had taken place and after removing the sample from the system the X-ray diffraction (XRD). The *in situ* measurements were performed during the controlled alloying between neighboring layers and after that process. The magnetic and transport properties were investigated with the help of a SQUID magnetometer and a 4-point probe for the measurements of temperature dependence of electrical resistivity over a wide temperature range. In addition, control tests of the surface topology were performed using the Atomic Force Microscopy.

2. Experimental details

A molecular beam epitaxy (MBE) system equipped with X-ray Photoelectron Spectroscopy (XPS) and Reflection High Energy Electron Diffraction (RHEED) systems was used to synthesize Eu-TM compounds by reaction in the solid state phase and to monitor the changes of the crystallographic and electronic structure of prepared films. Further measurements include X-ray diffraction and X-ray reflectivity but also studies of magnetic and transport properties of synthesized films. In this chapter the basis of applied methods and used growth procedures will be presented.

2.1 Film preparation

In the first part of the chapter an introduction to the basic principles of the Molecular Beam Epitaxy technique will be presented. This section will also include description of MBE deposition facilities used for the growth of Eu-TM films. Also developed and implemented procedures, such as preparation of the substrates, fabrication of the films, and description of the reaction parameters will be briefly described in this section.

2.1.1 Molecular Beam Epitaxy

Molecular Beam Epitaxy: Principles and Applications

Molecular Beam Epitaxy, developed by Cho and Arthur in 1970s is one of the most popular deposition processes [47] where the film material is transferred from solid precursors into a vapor phase in Ultra High Vacuum (UHV) and later condensed, after a transport, on a monocrystalline substrate. The evaporated elements in the form of "molecular beams" are in this process deposited onto crystalline substrate to form thin epitaxial layers. Film which has a

crystallographic structure ordered with respect to the crystallographic structure of the underlying substrate can be described as "epitaxial". Epitaxial films could be grown on a substrate of the same material, in which case the film can be described as "homoepitaxial"; or alternatively, if grown on a substrate of a different material, the film as "heteroepitaxial".

The MBE allow depositing different kinds of materials, it was firstly applied to the growth of semiconductors [48 - 50] however now it evolved in to a technique for producing also layers of metals or oxides [51]. Characteristic feature of the MBE is the possibility of growing high-quality and high-purity ultra-thin epitaxial layers with very abrupt interfaces, very good control of the film thickness or compositional profiles. To achieve this, several conditions such as slow grow rate, UHV environment, high-purity of materials must be provided.

In the MBE growth process several steps should be taken into account.

- Fabrication of molecular beam is the first step of the process. This is realized by heating in the UHV chamber the material source up to specific temperatures (depending on the type of material) as a result the material source evaporates. The groups of atoms, ions, free radicals or molecules produced, during that process in the gaseous state, and transported in the UHV chamber form so-called molecular beam. To ensure uniformity of deposited layer the molecular beam should be precisely stabilized, this can be achieved by applying appropriate growth parameters (evaporation rate or mass flux).
- Aforementioned transport of the molecular beams in the UHV chamber to the substrate is next step in the process. In the UHV environment, the beam of atoms or molecules should travels in nearly collision-free paths until arriving at the substrate where they condense. For this condition the mean free path λ of the particles should be larger than the geometrical size of the chamber, it can be maintained when the total pressure of the residual gas in the chamber in the range of $10^{-4} - 10^{-5}$ Torr. Nevertheless, to avoid the influence of residual gas impurities on both growth process and formation of high-purity layers, the UHV conditions are necessary. These conditions ensure the uniformity of the mass transport and formation of uniform layer of high purity.
- The vapor pressure of selected material should be high enough that it can be evaporated from the thermal sources but low enough that it can condensate on all surfaces within the MBE chamber. Condensation of the evaporated material onto the

substrate is the final step of the MBE process. Several elementary processes can be realized when the atoms or molecules arrived on the surface of the substrate. Figure 2.1 presents possible processes that have been taken into account; binding, surface diffusion, nucleation, island growth, coalescence, and continued growth.

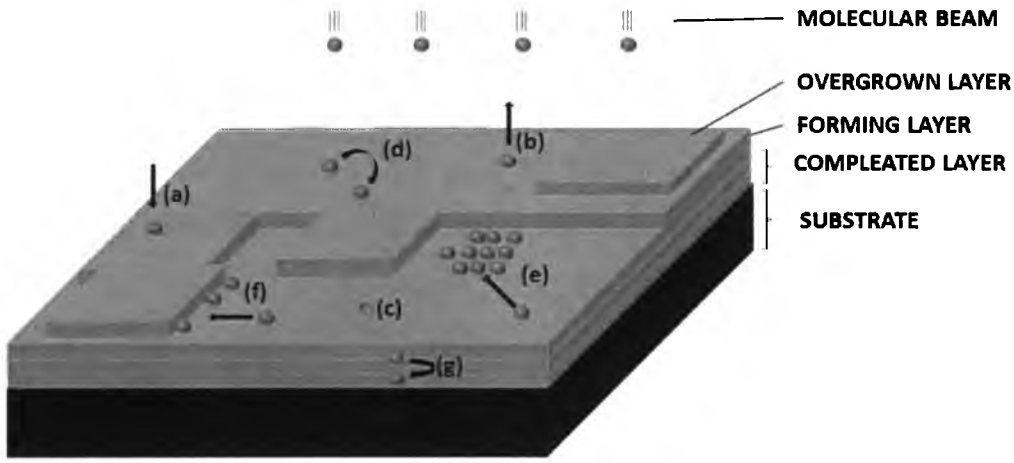

Figure 2.1 Possible processes during the MBE growth.

Adsorption of atoms or molecules on the surface of the substrate is the first possible process (a), the atoms may be or physisorbed in that case atoms are weakly bound to the surface of the substrate by van der Waals forces or can be chemisorbed when the bounding is stronger. Adsorbed atoms can be desorbed back into the vacuum chamber (b). Chemisorbed atoms may be incorporated (c) into the lattice by forming bulk-like bonding configurations. After adsorption atoms can migrate (d) across the surface, migrate into the crystal and diffuse in bulk (g), propagate along the surface until they find a step edge (e, f). Surface diffusion also allows formation of two dimensional clusters of adsorbed atoms (e).

The formation of new materials in described processes; by chemisorption, diffusion and further incorporation may result in different **growth modes**. Those are monolayer overgrowth, nuclear growth, and the growth mode that has both features of the former two. (See Figure 2.2) The growth modes depend upon various factors; the most important are growth temperature, interaction strength between adatoms and the surface, strain and surface energies of different materials. Layer by layer growth mode has been presented by the idealized Frank van der Merwe growth mode shown in Figure 2.2 in comparison with two other growth modes: the 3D island (Volmer-Weber) and island plus layer (Stranski-Krastanov).

Frank van der Merwe (FM) growth mode allows achieving the best structural properties and high quality flat surfaces; this mode requires substrate of very low misfit. In this two dimensional mode, called also a layer by layer growth, each atomic layer is completed (nucleated) before the next begins to grow. In three dimensional Volmer-Weber (WV) mode the adatoms are strongly bounded to each other more than to the substrate, in such case the atoms tend to agglomerate and form an island. Between FM and VW modes another growth mechanism exists, Stranski-Krastanov (SK) growth mode considered as intermediate between them. This process is characterized by both 2D layer and 3D island growth and it is caused by many different factors: surface energies and lattice parameters, lattice misfit from film and substrate.

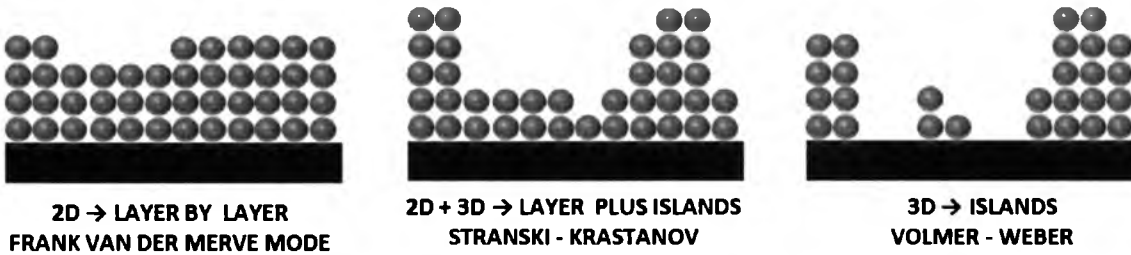

Figure 2.2 Growth modes.

Among other effects affecting the growth of the layers one has to mention factors like deposition rate and substrate temperature, bulk and surface diffusion, contamination (poor background pressure, impure deposition source, dirty or defected substrate), geometry: shadowing. Those factors lead to variations of the idealized, described above modes, such as step flow mode, columnar growth, step bunching, screw-island growth, coherent or incoherent 3D island growth, or layer-by-layer growth with strain relief.

Molecular Beam Epitaxy: Growth apparatus and components

Two similar MBE systems have been used for the films preparation, the first one located at Center for Magnetism and Magnetic Nanostructures at University of Colorado at Colorado Springs (See Figure 2.3) was used for preparation of majority of the Eu_xTM_y films, the second one located at August Chełkowski Institute of Physics at University of Silesia (See Figure 2.4) was used to clarify and confirm some of the Eu_xTM_y properties. Specific details concerning first MBE system can be found in [52].

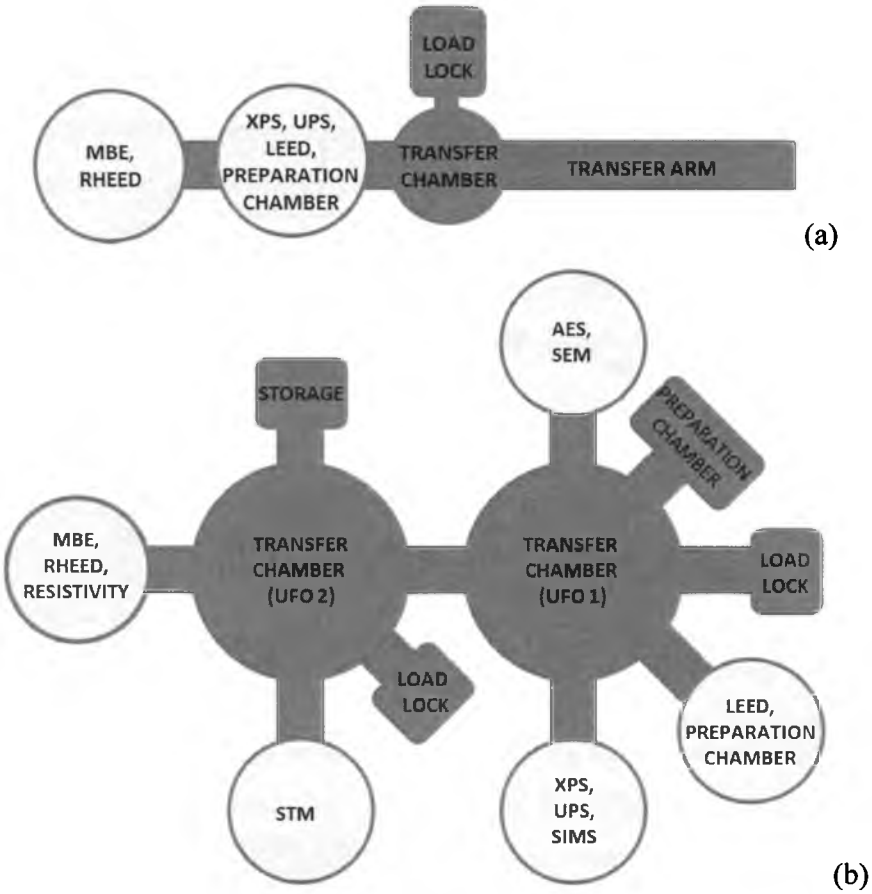

Figure 2.3 Schematic illustration of the MBE system located at (a) University of Colorado, (b) University Silesia

Both systems contain similar components which allow precise growth of desired elements with simultaneous control of the films quality. Both systems contain MBE chamber with typical for MBE method components, as it has been indicated schematically in Figure 2.4. Typically [49, 51] it contains the following essential components for MBE growth: source ovens, beam shutters and actuating mechanism, substrate heater and sample docking mechanism, in situ growth characterization tools, residual gas analyzer and/or separate beam flux monitor, cryopanels to act as cryopumps and to condense unused beam flux.

The MBE technique requires, as it was mentioned before, specific environment, the growth and further measurements have to be performed in UHV conditions. To realize that requirement the system of several pumps is demanded in the MBE chamber. Typical UHV pumping systems include a setup of few different pumps: rotary or diagram pump used as fore-vacuum pump, turbomolecular, ion, and/or cryogenic pump.

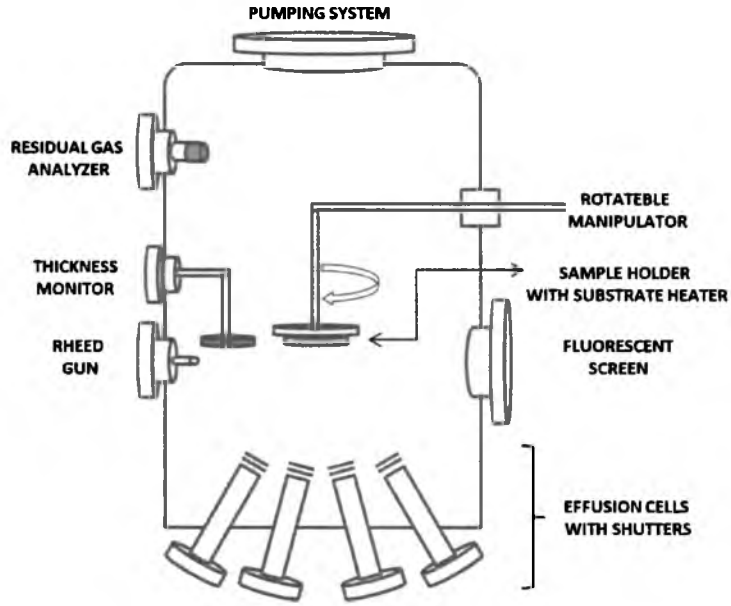

Figure 2.4 General scheme of MBE growth chamber

The quality of the vacuum in both systems was monitored by a Residual Gas Analyzer (SRS RGA) to make sure that no additional impurities or contaminations were introduced into the vacuum chamber during the growth process or later XPS measurements. During the growth process, the pressure in the vacuum chamber varied between 10^{-8} to 10^{-9} Torr, whereas during the RHEED and XPS measurements the pressure was about 10^{-10} Torr. During the growth process, H_2 was the main component of the residual gases.

The sample was mounted on rotatable manipulator which allows optimizing of the growth process (rotation during the growth and relative orientation to the evaporation source); the manipulator was equipped with a heated holder enabling the growth of the film under desired temperature conditions.

Many different kinds of evaporation sources are employed for flux generation in MBE their design roughly speaking depends on the kind of evaporated material. Here only two types of sources have been used. The first one - Knudsen cell is one of evaporation sources where indirect resistive heating has been applied. The increased thermal mass and the evaporant-heater separation (achieved by placing evaporant in the crucible, isolating it from the heater) stabilize the evaporation rate. The maximum temperature for the classic Knudsen cell is around 2000K. The second one- the electron-beam source is characterized by high deposition rates and large evaporant capacity. Here a high electron flux, generated by a hot filament placed below the source, is electrostatically and magnetically focused on the top of the

evaporant. The electron beam energy raises the evaporant surface temperature allowing for evaporation.

The Inficon TM-350/400 Thickness monitor has been used in both systems to provide a direct display of film thickness and deposition rate during deposition process. It uses a quartz crystal microbalance as the sensor, in such way that thickness of deposited film can be directly recalculated (inversely proportionality) from the quartz crystal frequency.

The RHEED gun used in both systems as in situ growth characterization tool will be described in details in 2.2.1 section of this thesis.

2.1.2 Design, preparation and research sequence of grown films

A series of alloys with different stochiometries and different thicknesses of Eu and Mn layers were grown on MgO, Al_2O_3, and Si or GaAs (with a 50 nm buffer layer of Mo) substrates. The final procedure of the film growth and the sequence of research have been illustrated on Figure 2.5.

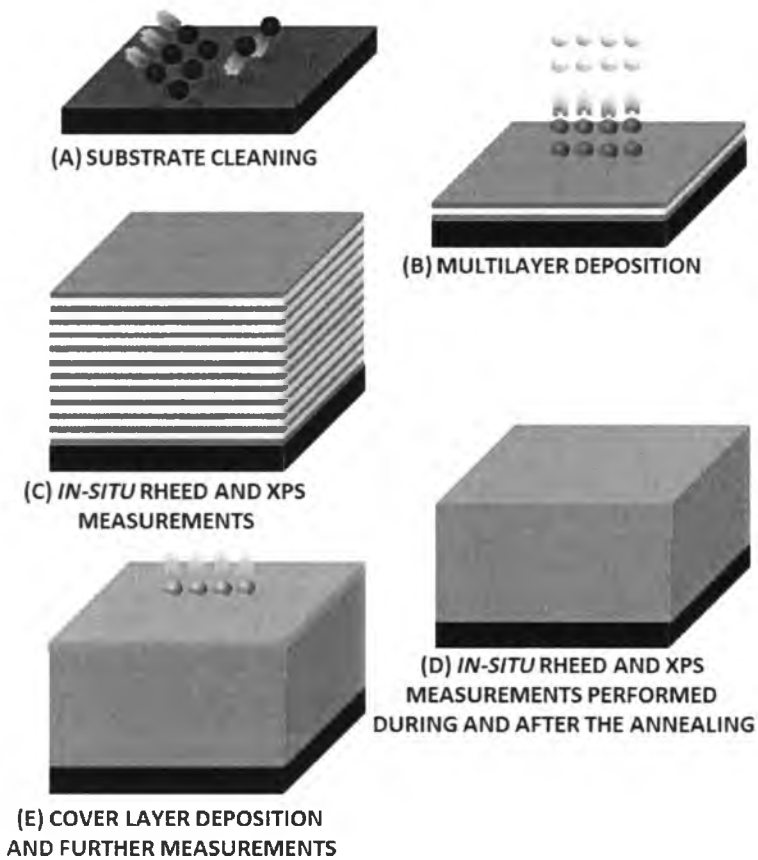

Figure 2.5 Sequence of film preparation and characterization procedures.

The surfaces of the Al_2O_3 and MgO substrates were cleaned by outgassing in an ultrahigh vacuum at about 600°C for 30 min, while the surface of the polycrystalline Mo buffer layer, grown by sputtering on Si or GaAs, was outgassed at 400°C and additionally cleaned by hydrogen gun at 500°C for 1h (see Figure 2.5 A). The growth of the Eu, Mn, Cr, Fe elements was executed after the substrate cooled to room temperature, no increase of the temperature was provided during the growth. The substrates have not been chosen to provide epitaxial growth; the motivation for their use was to have flat surface with the smallest amount of any type of contamination just to provide the best condition for studies of formation of new compounds and reaction between deposited elements.

In our studies we used two types of deposition: The first type was a co-deposition process while the second type was a multilayer process. The multilayer deposition process allows us to produce films with the assumed stoichiometries by depositing the layers of the metals with the proper thicknesses ratios (see Figure 2.5 B). Other parameters, such as the thickness of individual layer or total thickness were also taken into account to allow good efficiency for interfacial reaction between Eu and Mn atoms. Typically, depending on the stoichiometries of the desired compound, the thickness of an individual layer of Eu was varied from 4 to 20 Å while the thickness of individual Mn layer was consistently maintained at around 10 Å. To increase the probability of a solid state reaction in the films, we varied the number of interfaces from 2 to 40. The total thickness of films ranged from 30 to 300 Å. Detailed information about the thicknesses of particular layers can be found in Appendix 6.2.

To ensure the formation of Eu-TM compounds, the films were annealed up to 500K for about 24h. The reaction between Eu and Mn layers was monitored using RHEED and XPS (see Figure 2.5 C, D). RHEED investigations were performed using a 15 keV electron beam. In the XPS experiment, we measured the shape and chemical shifts of the core levels of Eu (3*d* and 4*d*) and Mn (2*p*, 3*p*, 3*s*), as well as the valence band structure with monochromatic Al K_α radiation (1486.7 eV). After the annealing process, the films were covered by Mo/Au layers to protect the surface from the oxidation during the *ex-situ* measurements (see Figure 2.5 E). Also different coatings, such as Ag and Cr, have been used to protect the films.

The *ex situ* structural characterization (θ-2θ and low angle reflectometry measurements) was carried out. A SQUID magnetometer was used to characterize the magnetic properties of the Eu_xTM_y films. Transport properties were measured in the temperature range of 20 to 500 K by a standard four point technique.

2.2 Characterization methods

Available research apparatus allows us to develop the procedures for conducting bi-directional measurements. The first direction, where the measurements were performed *in situ*, was monitoring the changes in the crystallographic and electron structure during the reaction of deposited elements via the RHEED and XPS. The second one was determination of the properties of reacted film by RHEED, XPS, SQUID, XRD, XRR, AFM, resistivity measurements. This chapter will include the basics of listed techniques.

2.2.1 Structural characterization

To characterize the crystallographic structure of examined films two different diffraction techniques (RHEED and XRD) have been applied. Additionally the X-Ray Reflectivity measurements, used for surface characterization of multilayer films, have been performed.

Reflection High Energy Electron Diffraction (RHEED) is the most popular and valuable *in-situ* technique routinely used in the MBE systems. This technique is ideal analytical tool for studying surface crystallography and its kinetics in the meaning of observation of real-time changes in surfaces of the films during deposition or desorption of adsorbates.
In this technique a high energy (up to 100 keV) electron beam is directed on the sample surface at grazing incidence; the diffraction pattern is imaged on a symmetrically placed fluorescent screen (see Figure 2.6). The grazing incidence (typically less than 3°) provides scattering of the electron beam in the first few atomic layers, this is due to the fact that the energy component perpendicular to the surface of the film is of order of 100keV, the penetration depth of incident electron is very limited, less than 10Å, giving a surface-sensitive diffraction pattern. As a result, crystal surface acts as a two dimensional grating which diffracts the incident electron beam. In addition, the system geometry: both the electron beam and the phosphor screen do not interfere with the MBE. Among all information that can be drawn from the RHEED images the most important are qualification of the nature of the film (amorphous in contrast to crystalline films does not give a diffraction pattern), determination

of the geometry of the surface including the flatness/roughness of a surface, formation of island, grains size, orientation of the crystallographic directions of both substrate and grown film, strains in the film. It also provides information on the kinetics of growth; as an example the improvement in the surface ordering that may occur with the subsequent annealing. Furthermore, calibration of the growth rate can provided by analysis of RHEED intensity oscillations.

The origin of RHEED patterns can be seen in Figure 2.6 (a) and (b). For flat and ordered surface the electrons interact only with the first atomic layer, the three-dimensional reciprocal lattice points degenerate into parallel infinite rods. The diffraction occurs at the points where each of the lattice rods intersects with the Ewald sphere. The radius of Ewald sphere, due to high electron energy, is very large when comparing to the reciprocal lattice rods constant, as a consequence the Ewald sphere intersects the lattice rods practically along their lengths. RHEED image for such flat surface consists of long and equally spaced streaks, normal to the shadow edge of the surface of the film [53, 54].

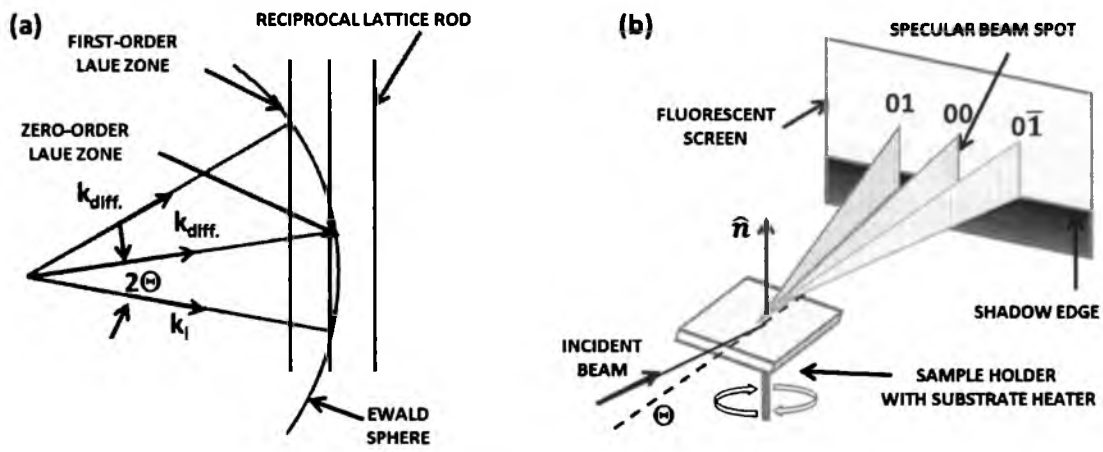

Figure 2.7 (a) Ewald sphere construction, (b) RHEED geometry and formation of a diffraction pattern.

Depending on the nature of the surface of deposited layer several types of RHEED images can be observed (see Figure 2.7):

- the RHEED image for monocrystalline flat surface consists of concentrically aligned Laue circles spots as it has been presented for ideal flat surface (a), formation of concentrically spaced streaks (b) is due to the finite width of the rods,

  - the spacing of the RHEED streaks can give information regarding the periodicity of the surface, the distance between the streaks on the screen is inversely proportional to the lattice interplanar spacing of the crystal
  - weaker fractional order streaks located between the integer order streaks indicate the periodicity of the surface reconstruction
- transmission features exhibiting bulk-like reflections as shown on image (c) are characteristic for monocrystalline films with rough surface [55]. In that case electron must pass through the irregularities (or the presence of small crystallites or 3D islands on the surface) and consequently the transmission patterns in the form of individual points are the results. Small surface roughness is indicated as spots and lines on the fluorescent screen [56].
- polycrystalline surfaces give diffused background with concentric rings (d), similarly textured films would be represented on the fluorescent screen by concentric arcs instead of the rings. These types of images allows to determine: (i) the texture of the film, (ii) the average angle of the texture axis with respect to the surface normal, and (iii) the angular width of the distribution of this angle about its average value [54, 57].
- amorphous surface give only diffused background.

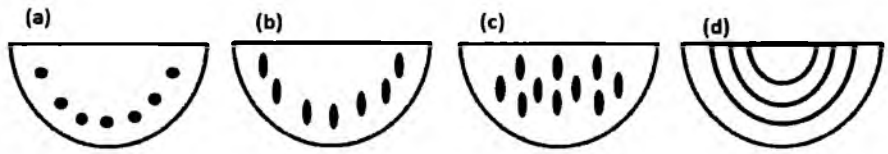

Figure 2.7 Schematic diffraction patterns for (a) ideal smooth surface, (b) real smooth surface, (c) transmission diffraction through 3D clusters, (d) diffraction form polycrystalline or textured surface.

X-ray Diffraction (XRD) has been used as a method for the crystallographic characterization of grown films. When electromagnetic radiation impinges on periodic structures which has the geometrical variations on the length scale comparable to the wavelength of the radiation the diffraction effects are observed. The interatomic distances in crystals and molecules are in the range 1.5–4Å, in the electromagnetic spectrum this corresponds with the wavelength of x-rays having photon energies between 3 and 8 keV. Due to that reason the X-rays are the best radiation for probing the structural arrangement of atoms and molecules in a wide range of

materials. X-rays penetrate deep into the materials and may provide information about the bulk structure of the crystalline materials.

Information that may be obtained from XRD measurements are wide and include, inter alia: crystal structure (by Rietveld refinement of the diffraction pattern), unit cell lattice parameters and Bravais lattice symmetry, phase composition of a sample (determination of relative amounts of phases in a mixture), residual strain, texture, crystallite size (indicated by peak broadening), and other effects.

In order to better understand the fundamental principles of X-ray diffraction, some theoretical considerations will be presented. When certain geometric requirements are met (Bragg law, and Figure 2.8(a)) a diffracted beam is produced as a result of interference of scattered from a crystalline solid X-rays, the resultant intensity distribution is strongly modulated by this interaction. The difference in path length between incident and diffracted beam must be an integral number of wavelengths. If the atoms are arranged in a periodic lattice the diffracted beams will consist of sharp interference maxima with the same symmetry as in the distribution of the atoms in the lattice [58-61].

The $\theta/2\theta$ diffractometer, shown on Figure 2.8(b), is the most often used instrument for measuring the Bragg reflection of a thin film. The diffraction pattern is collected by changing the incidence angle of the incoming X-ray beam by θ and the scattering angle by 2θ.

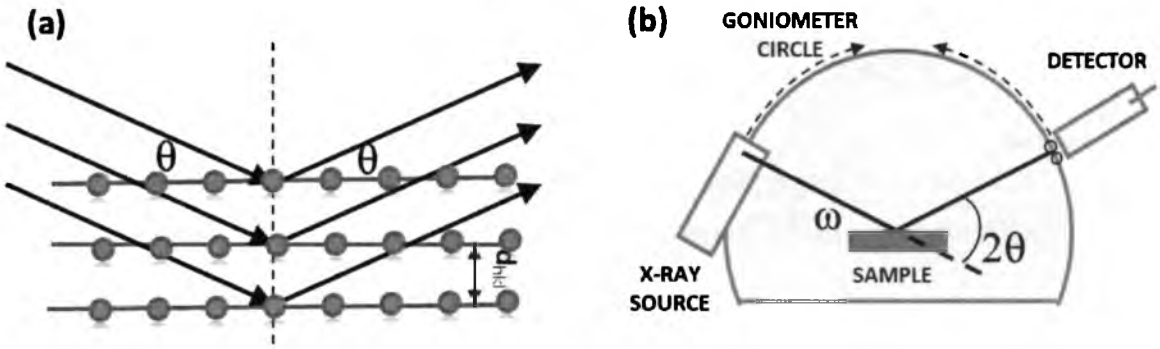

Figure 2.8 (a) Illustration of the geometry used for the simplified derivation of Bragg's law, (b) Schematic representation of θ/2θ diffraction in Bragg–Brentano geometry

The scattered intensity I(2θ) is measured as a function of the latter. According to that two angles have to be changed during a $\theta/2\theta$ scan. For one set of instruments the x-ray source remains fixed while the sample is rotated around θ and the detector moves by 2θ. For other systems the sample is fixed while both the X-ray source and the detector rotate by θ simultaneously, but clockwise and anticlockwise, respectively [62].

Bragg-Brentano geometry commonly produces unsatisfactory low-intensity reflections received from the film phases; moreover those reflections are strongly masked by substrate scatter. An alternative uncoupled geometry - Glancing-incidence asymmetric Bragg diffraction, is more surface-sensitive technique, and easily can be applied for the structural characterization of the thin films. The technique uses a fixed low-incidence angle and parallel-beam optics to increase path length through the sample and decrease X-ray penetration into the substrate. As a result, observed in the diffraction patterns, relative sample peak intensities is higher whereas relative substrate peaks are lower. Some other applications should also be mentioned. For the characterization of defects in the thin films the Rocking Curve measurements are widely applied, in this technique detector is fixed at 2θ and the film is scanned around the θ, the broadening of the peak gives information about the quality of the film. To determine the orientation distribution in a polycrystalline sample other technique, texture measurements, can be applied. Panoramic view of the structural properties of the films is realized via performing a scan, with fixed at 2θ detector, by in-plane rotation around the plane normal at different azimuthal angles [58, 61, 62].

Nevertheless the X-ray diffraction measurements presented in this thesis have been performed, in the conventional Bragg-Brentano parafocusing geometry, with the use of X-pert Diffractometer situated at University du Main in Le Mans, France. The analysis has been accomplished with the use of several different programs for XRD analysis: PowderCell for Windows (version 2.4), FullProff, Maud and High Score Plus (version 3.0.c).

Specular **X-ray Reflectivity (XRR)**, a technique parallel to X-ray Diffraction (XRD), non-destructive and non-contact technique is now becoming a widely used tool for the characterization of thin-film and multilayer structures. It has been devoted mainly to investigating the morphology of the samples The advantage of that technique is that it does not rely on diffraction phenomena, the investigated sample does not have to consist of crystalline matter it may be amorphous, the only limitation is the thickness of the layer up to 200nm.

Among the different applications of that technique the main one should be listed:

- thickness determination between 2-200 nm with a precision of about 1-3 Å,
- determination of electron density, it can be determined from the critical angle,

- determination of the roughness or interdiffusion at the interface between the layer and the substrate, as well as the roughness of the layer by itself, for a rough surface, the reflectivity falls faster than for a flat one,
- monitoring of the uniformity across wafers, as well as pore density and pore size.

In this technique [63 - 65] collimated monochromatic X-ray beam irradiates the film at very low angles ($0 < \theta < 4°$) with respect to the surface of the film. Diffracted X-rays are collected in the detector at angle 2θ with respect to the incident beam after experiencing multiple reflection and refraction at the different interfaces in the film, see Figure 2.9.

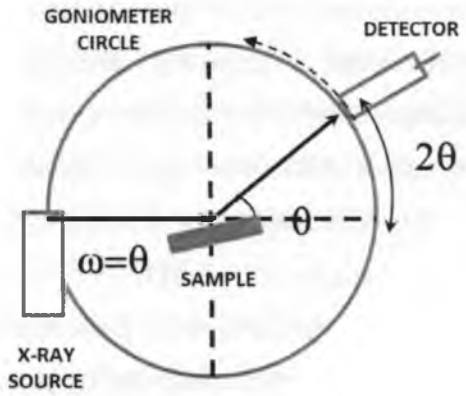

Figure 2.9 X-Ray reflectivity geometry.

A monochromatic x-ray beam of wavelength λ irradiates a sample at a grazing angle ω and the reflected intensity at an angle 2θ is recorded by a detector. The figure 2.9 demonstrates specular reflection where the condition $\omega = 2\theta/2$ is satisfied. The $\theta/2\theta$ operation mode provides that incident angle is always half of the angle of diffraction. The reflection at the surface and interfaces results from the different electron densities in the different layers and this corresponds to different reflective indexes in the classical optics. For incident angles θ below a critical angle θ_c, total external reflection occurs. Above θ_c the reflection from the different interfaces interfere and give rise to interference fringes. The period of the interference fringes and the fall in the intensity are related to the thickness and the roughness of the layer (layers in case of multilayers).

Since in specular reflectivity only the z-component of the wave vector is non-vanishing typically the specular reflectivity is presented as a function of the wave-vector Q_z where the z-component of the transfer wave vector can be expressed as follows $Q_z=(4\pi\sin\theta)/\lambda$.

The interaction of X-rays with matter can be well described by an index of refraction which characterizes the change of direction of the X-ray beam when passing from air to a material. A classical model in which an electron of the material is considered to be accelerated by the X-ray field shows that the index of refraction for X-rays can be written as

$$n = 1 - \delta - i\beta \qquad 2.1$$

where δ and β describe dispersion and absorption terms. The values of δ and β depend on the electron density, ρ, and linear absorption coefficient, μ, of the material. If the reflective index is slightly less than 1 a beam impinges on flat surface and can be totally reflected. That would be possible when incident angle is smaller than the critical angle θ_c defined as

$$cos\theta_c = n = 1 - \delta \qquad 2.2$$

Assuming that n is very close to unity, after some mathematical approximation the critical angle can be related to the electron density, ρ, wavelength λ and the classical radius of the electron r_e as it has been presented in equation 2.3

$$\theta_c^2 = 2\delta = \frac{r_e\lambda^2}{\pi}\rho \qquad 2.3$$

For identified single periodicity a computation of the thickness of the thin film can be carried out in accordance with the formula 2.4

$$t = \frac{\lambda}{2\Delta\theta} \qquad 2.4$$

where $\Delta\theta$ is a difference between two consecutive minima and λ is wavelength.

To summarize the average electron density can be directly connect to the critical angle. The period of characteristic fringes, visible above the critical angle in the XRR profile interference fringes, indicate total thickens of the layer, it can be calculated for both single layers as well as for multilayer structures. The decay of XRR intensity is related to the roughness of the surface of the layer, and of the interface with the substrate.

X-ray reflectivity measurements have been performed with the use of X-pert Diffractometer situated at University du Main in Le Mans, France. Reflectivity calculation and density profiles were obtained with based on Matlab program written by G. Vignaud and A. Gibaud Reflectivitie 2000.

2.2.2 X-Ray Photoelectron Spectroscopy

X-ray photoelectron spectroscopy (XPS) is one of the most powerful analysis techniques in surface physics [66-68]. It allows obtaining in detail valuable information about not only the electronic structure but also about the chemical composition of any solid material and the types of bonding that occurs within many compounds.

The basis of the photoemission experiment in the independent particle description is the absorption of a photon and the transfer of its total energy to an electron, schematically it has been shown in Figure 2.10 the latter is excited from the state | i > into the state | f >:

$$h\upsilon = E_f - E_i \qquad 2.5$$

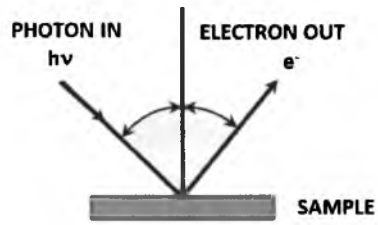

Figure 2.10 Schematic diagram showing the processes of photoemission.

If the E_f is large enough, the electron can overcome the work function barrier Φ and be emitted into vacuum. The kinetics of such process is given by Einstein equation:

$$E_{kin} = h\upsilon - \Phi - E_B \qquad 2.5$$

While the work function Φ is consistent for each sample on a specific XPS analyzer, the binding energy E_B is dependent on the type of atom the electron came from as well as atom environment.

In the XPS experiment mono-energetic soft X-rays (typically Al Kα radiation, $h\nu$ = 1486.7 eV) irradiate the sample with a penetration depth of 1-10 mm. The probing depth is limited by the inelastic mean free path of the photoelectrons; electron escape depth is typically of 5-20 Å which gives the actual sizes of depth sensitivity of that technique. The kinetic energy of ejected, during the photoemission process, electrons is measured by an electron energy analyzer. Figure 2.11 shows a typical setup for the XPS experiment.

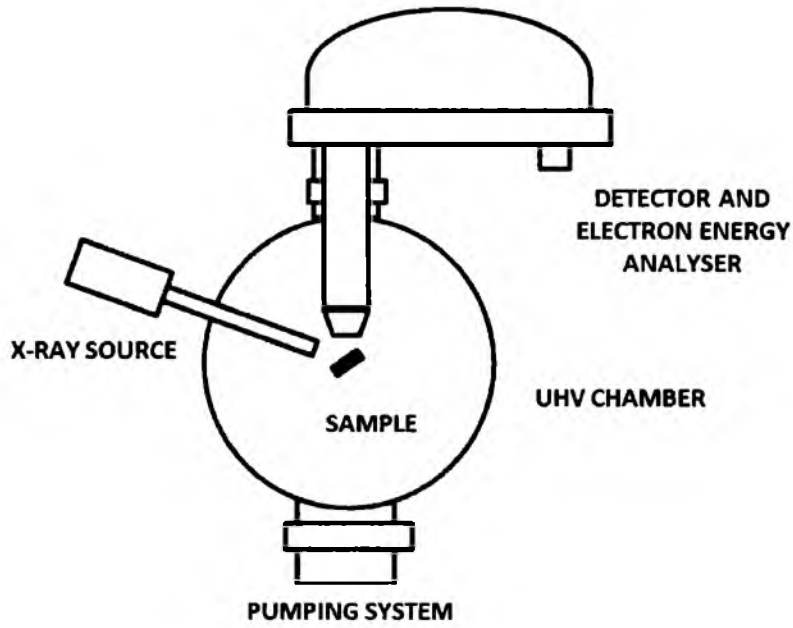

Figure 2.11 Typical setup for the XPS experiment.

Since every element has a characteristic, related with each core atomic orbital, binding energy the specific set of peaks in the photoelectron spectrum will be pronounced. The presence of the peaks at particular energies indicates the presence of a specific element in measured sample. The intensity of the peaks is related to the concentration of the element within the analyzed region. Thus, the technique provides a quantitative analysis of the surface composition. Typical application of the XPS technique:

- identification of elements (with the exception of H and He),
- quantitative analysis of chemical composition,
- identification of chemical state (valence, etc.),
- determination of the distribution of the elements in tested material, including determination of the distribution of atoms and compounds adsorbed on the sample surface,
- examination of surface phenomena such as catalysis,
- depth profiling for thin film composition,
- valance band structure.

An X-ray photoelectron spectroscopy system from Specs GmbH was used for in-situ X-ray photoelectron spectroscopy (XPS) studies performed at University of Colorado at Colorado Springs (UCCS). Photoelectrons were excited with monochromatized Al K_α (1487 eV) radiation. A nine-channel hemispherical energy analyser (Specs GmbH, model PHOIBOS

150) was used for spectra acquisition. Strong charging effects observed in films grown on MgO and Al_2O_3 have been neutralized with the use of a flood gun during XPS measurements. Spectra were collected in normal photoemission. Different spectrometer, Physical Electronics PHI 5700/660 was used for the measurements performed at University of Silesia. Due to the fact that the measurements in Katowice has to confirm some studies performed at UCCS laboratories other parameters like vacuum conditions, excitation source, or parameters used during the measurements (pass energy values, acquisition time) were basically the same. The XPS measurement executed at University of Silesia have been supplemented by the depth profile measurements. Ultra high vacuum (UHV), ensured through the use of several different pumps, allowed for performing the measurements at good conditions in both systems; the pressure during the XPS measurements was about 10^{-10} Torr.

2.2.3 Magnetic measurements

Superconducting quantum interference device (SQUID) magnetometer is one the most sensitive instrument for magnetic moment characterization. Wide range of both temperature and applied magnetic field is a standard for measurements in this technique [69,70].

The essential element of the magnetometer is the superconducting quantum interferometer where quantum interference of charge carriers is being to detect and measure very small changes in magnetic induction. The principle of performing the SQUID measurements is following (see Fig. 2.12) [70]; the sample is placed on mobile holder that has a possibility of

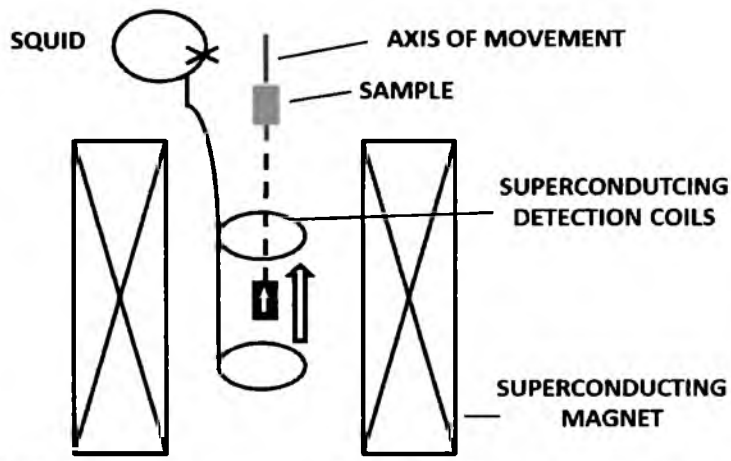

2.12. Schematic representation of SQUID measurement set up.

movement along the symmetry axis of superconducting detection coils and a superconducting magnet. Induction of an electric current in the detection coils is provided by the magnetic moment of the sample which is changing due to its movement along the symmetry axis. The persistent current in the detection circuit is modified because of the variation of magnetic flux in superconducting coils. The modified output voltage in the SQUID, basically proportionate to the magnetic moment of the sample, is being produced by the variation of the current in the detection circuit.

Mentioned above four components, the SQUID device itself, magnetic shields, superconducting magnet, and the superconductive detection coils, are the main constituents of the SQUID apparatus. The SQUID device, the most important module in the magnetometer, consists of two superconductors separated by thin insulating layers to form two parallel Josephson junctions. If a constant biasing current is maintained in the SQUID device, the measured voltage oscillates with the changes in phase at the two junctions, which depends upon the change in the magnetic flux. This device has been used in the magnetometer to convert the induced current to the, proportional to the magnetic moment of the sample, voltage in an extremely sensitive manner. Since the device is characterized by an extreme sensitivity it has to be isolated from the influence of large magnetic field induced by the superconducting magnet, for this purpose a superconducting magnetic shields are being used. To allow the measurements, via SQUID device, of the magnetic moment of the sample placed inside the superconducting magnet the superconducting detection coils had to be inserted as it has been shown in the Figure 2.12. The geometrical configuration of detection coils (single superconducting wire) decrease noise from nearby magnetic objects in the surrounding environment. The last component of the magnetometer is superconducting magnet, it is a solenoid made of a superconducting wire that in typical SQUID apparatus can produce magnetic fields in the range 5-18 Tesla.

The SQUID measurements are typically applied for the measurements of:

- real and imaginary components of the AC magnetic susceptibility as a function of frequency, temperature, AC magnetic field amplitude and DC magnetic field value,
- DC magnetic moment as a function of temperature, DC magnetic field, and time. Using a specially designed sample holder the magnetic moment as a function of angle can be also measured.

In the thesis results have been obtained on the Quantum Designed magnetometer SQUID QD-MPMS-XL-7AC are presented. For that instrument the measurements can be conducted in the temperature range 1.9 K - 400 K. An additional option allows the measurement of the weakest magnetic materials by providing high magnetic field homogeneity. Performed measurements contain: temperature dependence of magnetic moment measured in zero field (ZFC) and field cooled (FC) modes at different external fields (10, 50, 100 and 1000 Oe), as well as field dependence of magnetic moment (hysteresis loops).

2.2.4 Resistivity measurements

The last type of measurements used for the characterization of the properties of the films was based on four-point contact resistivity measurements. This method, described in [71, 72], uses four probes, at a fixed spacing distance, aligned linearly that contact the surface of the test material. In this technique the two outer probes are connected to a current supply, and the inner probes to a voltage meter, as it has been shown on Figure 2.13. As current flows between the outer probes, the voltage drop across the inner probes is measured. The relationship of the current and voltage values is dependent on the resistivity of the material under test, and the geometrical characteristics of the probe as per follows $V = \rho V/I = I/2\pi r$; where ρ is the surface resistivity of a material of semi-infinite size, I is the current in the probe, and r is the distance between the voltage measurement and the current probe. The equation is proper with the assumption that the sample is infinite slab and that the spacing between the probes is equal [71, 73]. Some additional correction factors need to be taken into account because the measurements are made on finite sized areas. This correction factor, based on the sample geometry, strongly depends on the sample thickness, edge effects, thickness effects, and the location of the probe on the sample.

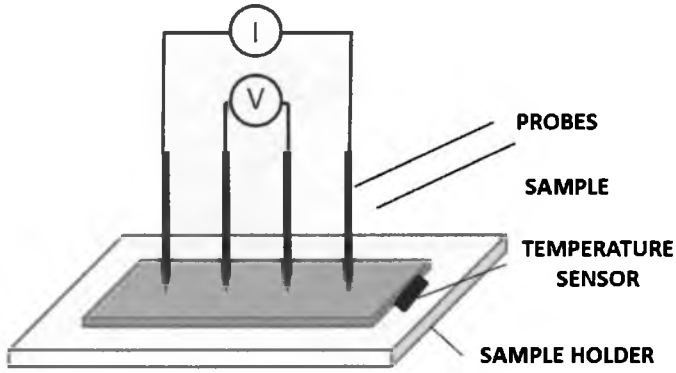

Figure 2.13 Schematic four-point probe set up for resistivity measurements.

For our purpose the system for the resistivity measurements consisted of several elements. The measurements have been performed in vacuum chamber, where the rotary and turbomolecular pumps provided favorable conditions for measurements. The sample has been mounted on the suitable for high and low temperature measurements sample holder. The resistive heater allowed performing measurements up to 500 K. Low temperature measurements were realized by the use of a "cold finger", the application of that device allowed for performing the measurement up to 20 K. Such low temperatures could be achieved because of the approach of cooling the "finger", the sample has been cooled down by compressed helium similarly as in case of cryogenic pumps (with the difference that the cooled surface is at the same time the sample holder). In order to obtain the best electrical contact four equally spaced metal tips, with a finite radius, coated with gold has been used. Each tip was supported by springs on the other end to minimize sample damage during the probing. The temperature has been measured with the use of the platinum resistance thermometer in a 20-500 K wide range.

3. Results and Discussion

This chapter is divided into three parts which include the analysis of results obtained for three different Eu-TM systems. The most extensive is the first part where the analysis for the Eu-Mn system has been presented. Two other sections contain the analysis conducted for the Eu-Fe and Eu-Cr systems.

3.1 Eu – Mn system

The formation of rare earth (RE)/Mn binary compounds with different stoichiometries in the bulk form is known. Although in comparison to the other transition metals such as iron or cobalt in this system the number of stable compounds is limited only for few stoichiometries: $REMn_2$, RE_6Mn_{23}, and REMn12 (for details see Table 1). The $REMn_2$ stoichiometry is among them the most often formed. Even though other stoichiometries in the RE-Mn system seem not to be realized we have attempted to prepare compounds in the thin film form in a wide range of concentrations of europium and manganese.

The deposition was performed by thermal evaporation of elemental sources: Eu (99.99 %), Mn (99.99 %), and Mo (99.95%), Au (99.999 %). Deposition of europium, manganese and gold was done with the use of standard effusion cells, while the molybdenum (used as a protective top layer) with the use of electron beam evaporator. The films were grown in two modes – in the multilayer form or in the co-deposition process, growth procedures has been described in details in Chapter 2.1.2. Growth of Eu-Mn films performed by deposition multilayers of $(Eu/Mn)_x$ layers required a deposition of different thicknesses of individual Eu and Mn layers to achieve assumed concentration. Typical growth rates have been combined in Table 3.1.1.

Table 3.1.1 Growth rates for the Eu-Mn system.

Element	Growth rate [Å/s]
Europium	0.01-0.02
Manganese	0.02-0.03
Gold	0.02-0.04
Molybdenum	0.02

Several representative samples have been chosen to present behavior of the Eu_xMn_y system. In order to standardize the description of the samples in this work the Eu/Mn ratio will be combined with the name of the sample (see Table 3.1.2). The Eu/Mn ratios were calculated from the results of the XPS measurements and will be discussed in Chapter 3.1.2. The thicknesses of analyzed films and their as-grown structure have been summarized in Appendix B. Nevertheless, the total thickness and thickness of individual layers of grown films will be listed along with published results when it will be essential.

Table 3.1.2 Description of Eu_xMn_y films selected for the structural analysis

Sample name	Assumed concentration (Eu/Mn ratio)		Thickness [Å]	Eu/Mn ratio after deposition*	Annealing process	Eu/Mn ratio after annealing*
"A-Mn"	$EuMn_2$	(0.5)	58.1	0.7	100°C (15h)	0.32
"B-Mn"	$EuMn_5$	(0.2)	35	0.74	150°C (15h)	0.63
"C-Mn"	$EuMn_2$	(0.5)	58.4	2.9	150°C (15h)	1.5
"D-Mn"	$EuMn_2$	(0.5)	58.1	0.57	200°C (20h)	0.94
"E-Mn"	$EuMn_3$	(0.3)	181.6	0.6	200°C (20h)	0.52
"F-Mn"	Eu_2Mn_{17}	(0.12)	307.6	1.07	250C (15h) 200°C (4h)	0.78
"G-Mn"	Eu_xMn_y		300	0.46	200°C (15h)	1.44
"H-Mn"	Eu_2Mn_{17}	(0.12)	436.4	-	300°C (60h)	-
"I-Mn"	Eu_xMn_y		200	0.58	200°C (15h)	0.59
"J-Mn"	Eu_2Mn_{17}	(0.12)	307.6	1.35	-	-
"K-Mn"	Eu_2Mn_{17}	(0.12)	266.7	0.73	200°C (20h)	0.59
"L-Mn"	$EuMn_5$	(0.2)	140,1	0.82	up to 250°C (40h)	0.42
"M-Mn"	Eu_2Mn_{17}	(0.12)	266.7	0.8	300°C (10h) 400°C (6h)	0.2
"N-Mn"	Eu_2Mn_{17}	(0.12)	43.1	0.63	up to 500°C	0.3
"O-Mn"	$EuMn_2$	(0.5)	103.9		200°C (20h)	0.51
"P-Mn"	EuMn	(1)	96.8	5.21	200°C (2h) 300°C (6h)	0.9
"R-Mn"	$EuMn_5$	(0.2)	248.6	0.74	200°C (30h)	0.99

3.1.1 Crystallographic structure

In this chapter the results of several different experiments, namely the result of RHEED, XRR and the XRD studies, will be presented. The RHEED images have been obtained *in situ* and were the first criterion for assessing the quality of the layer. The analysis of RHEED studies will be also the first step in determination of the possibility of mixing of grown layer, stating whether in the given conditions, europium and manganese may react with each other and form and create atomically ordered phases. Next step in structural characterization was applying the XRR technique; the results of the XRR measurements and some calculations will be presented right before the presentation of the XRD measurements.

During the deposition of each element, in each and every sample, no trace intensity oscillations of the specularly reflected electron beam have been reported, and the thickness of the layers was controlled only via the thickness monitor.

The mode of growth and changes of the surface structure were investigated in detail using RHEED. At the beginning the RHEED pattern is shown for the multilayer growth of Eu and Mn layers. After deposition at room temperature of single layers of Eu and Mn on MgO [001], changes in the crystalline structure are observed. As an example, in Figure 3.1.1 the RHEED patterns obtained during the deposition of a multilayer structure of $EuMn_2$ on MgO have been presented. The patterns changed with the type of grown element: from weakly developed polycrystalline rings visible for the first layer of Mn, through weak polycrystalline rings with diffused spots of high intensity for the Eu layer, up to a well-developed polycrystalline layer for the last Mn layer.

No significant changes are observed for measurements performed at different angle (see Figure 3.1.1A and 3.1.1.B). After the sample rotation along the z-axis by 45 degrees the RHEED image only firstly deposited iron layer (3.1.1.B b) differs from the one obtained along the [100] MgO azimuth (3.1.1.A b). It seems that along the [100] azimuth of MgO the 5.6Å thick manganese layer is textured, whereas for [110] azimuth of MgO presents more polycrystalline behavior.

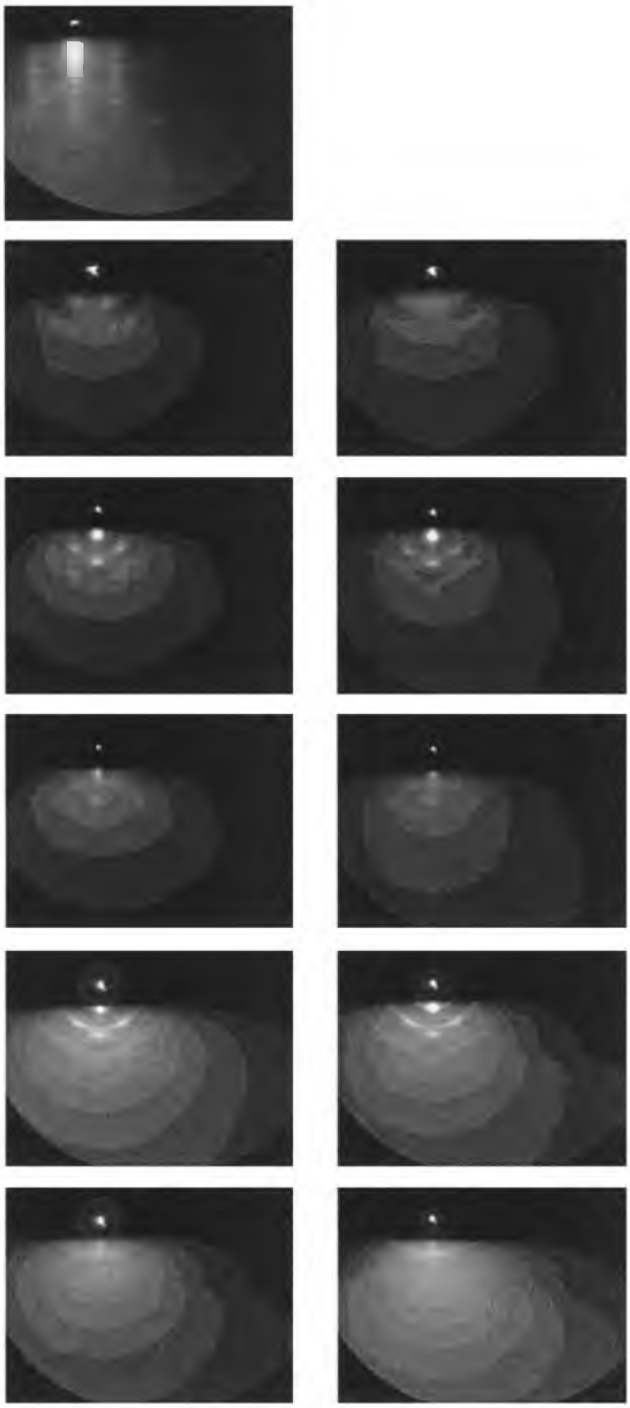

(a) MgO

(b) MgO / Mn (5,6Å)

(c) MgO / Mn (5,6Å) / Eu (18,3Å)

(d) MgO / Mn (5,6Å) / Eu (18,3Å) / Mn (5,6Å)

(e) MgO / Mn (5,6Å) / Eu (18,3Å) / Mn (5,6Å) / Eu (20,6Å)

(f) MgO / Mn (5,6Å) / Eu (18,3Å) / Mn (5,6Å) / Eu (20,6Å) /Mn (8,4Å)

3.1.1.A Sample edge (MgO [100] azimuth)

3.1.1.B Sample diagonal (MgO [110] azimuth)

Fig. 3.1.1 Growth of Eu/Mn multilayer ("A-Mn" film) on MgO presented for measurements performed along the sample edge (3.1.1.A) and its diagonal (3.1.1.B).

Structural changes in the deposited layers were also observed after the annealing process; see Figure 3.1.2. To demonstrate this effect several representative samples have been selected (see Table 3.1.1, for detailed information about the multilayer structure see Appendix B).

For the series grown on Si/Mo or GaAs/Mo, where the thicknesses of the grown films were smaller than 100Å ("thin series"), as in films: "A-Mn", "B-Mn", "C-Mn", "D-Mn", the RHEED pattern shows a set of weak rings with additional diffused spots of a much higher intensity (indicating a polycrystalline sample with some partial texture) right after deposition. The diffraction pattern obtained after the annealing process showed slightly different set of rings and because of that and disappearance of diffused spots the formation of a polycrystalline film is considered.

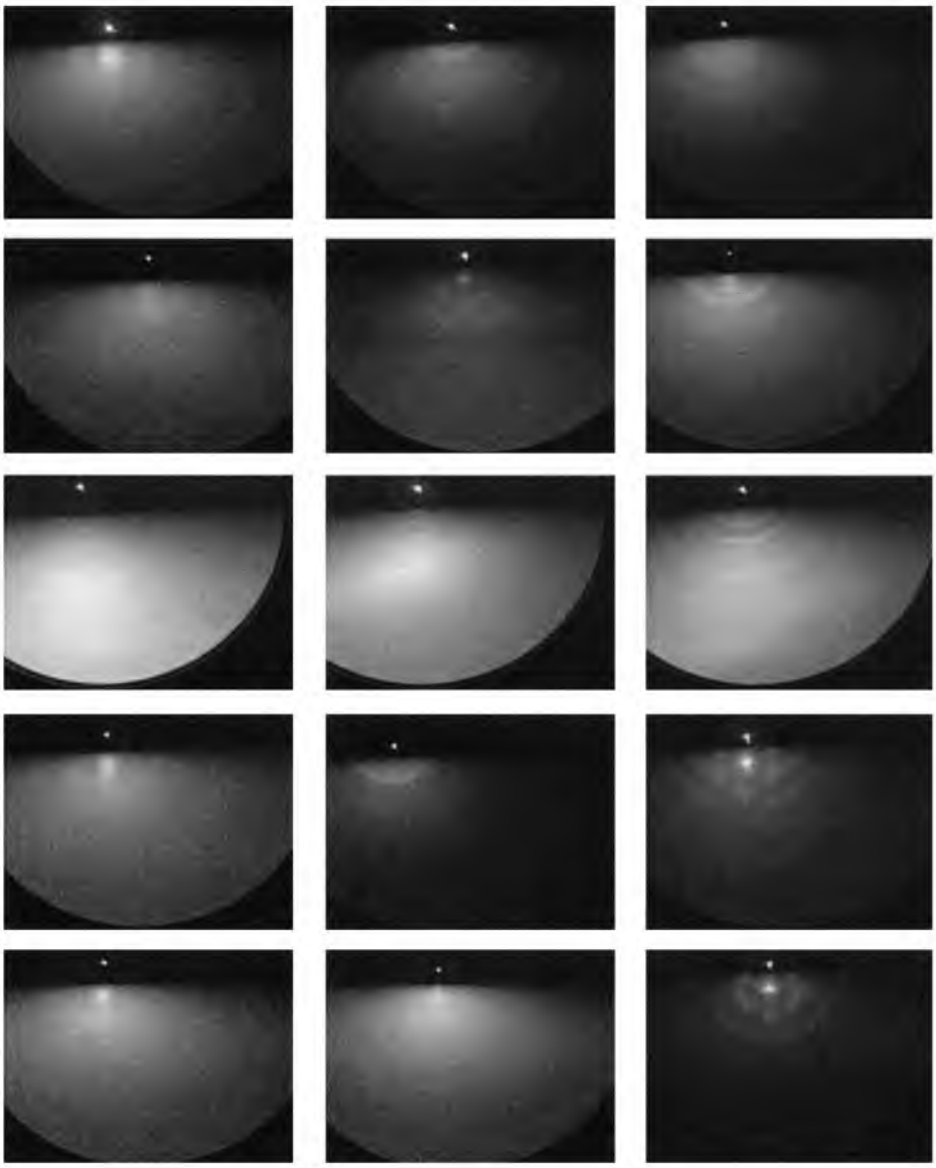

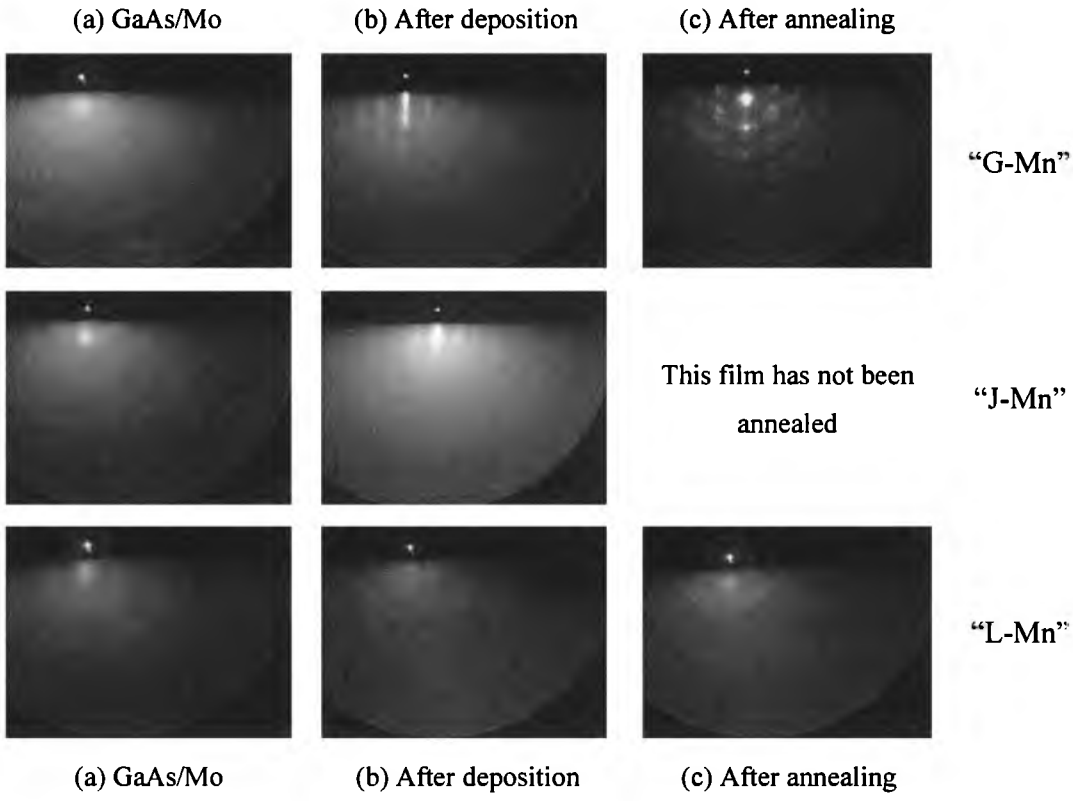

Figure 3.1.2 RHEED patterns obtained for Eu-Mn system where column (a) shows a pattern of the substrate, (b) pattern of grown film, (c) pattern of annealed film.

For the series of films with total thicknesses larger than 100Å ("E-Mn", "F-Mn", "H-Mn", "J-Mn", "L-Mn""), the RHEED patterns consisted only of weak rings after deposition, while the post-annealing patterns showed a different set of rings in addition to diffused spots of much higher intensity. The latter result indicates a polycrystalline structure after annealing with at least partial texture with a possible formation of three-dimensional islands. However, for the samples grown in the co-deposition process (see sample "G-Mn" in Figure 3.1.2), the observed changes differ from the multilayer structures. The RHEED pattern shows well developed streaks after deposition which evolves into a polycrystalline film with a strong texture. The increased temperature lead to reaction within the film and the final structure is more island-like. The lateral position of the main spots is however the same as that of the streaks before annealing indicating to remaining atomic order in the plane of the film [89, 77]. Only one film grown on MgO changed after the annealing process; from a polycrystalline structure (visible on the image as a set of weak rings) into a monocrystalline-like film as visible in the pattern (see Figure 3.1.3).

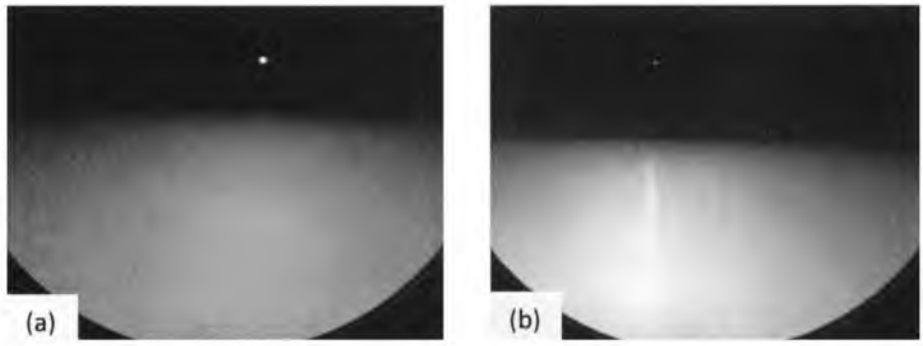

Figure 3.1.3 RHEED pattern obtained for the "H-Mn" film, grown on the MgO (a) after deposition, (b) after annealing.

To determine the crystallographic structure and other properties of the grown films, XRD and x-ray reflectivity studies were performed. All measurements have been performed after annealing process and after covering the film with the protective coating; typically, to protect the film from further reaction, the ~10Å Mo layer was deposited on the top of the film and later ~20Å layer of Au. The thickness and type of applied protective coating has been listed in Appendix B.

Well-defined oscillations in the XRR patterns (see Figure 3.1.4) can be observed for majority of examined concentrations. Characteristic peak above 0.6 $Å^{-1}$ has been seen only for "M-Mn" film, grown on MgO.

To determine the impact of annealing on the mixing of the layers a following test has been performed. Two identical, in terms of thickness and structure, samples "J-Mn", "F-Mn" have been grown in the same conditions. One of the samples, "F-Mn" was annealed at 200 °C and later covered by a protective coating, whereas the second one "J-Mn" has been covered as it was grown. Performed XRR measurements, presented in Figure 3.1.4, did not allow performing meaningful calculations. Nevertheless, in the specular reflectivity spectrum, there are significant differences between those two samples which allow drawing several conclusions. The bumps visible for higher angles (and high Q_z, Q_z above 0.4 $Å^{-1}$), are due to the existence of layers within the film that have not been fully mixed with each other. Since the number of bumps is directly connected with the number of layers in the film, it seems that even without annealing the intermixing of the layers occurs. The structure (see Appendix B) of the "J-Mn" film implies that more bumps should be observed on the specular reflectivity plot. Nevertheless it is possible to roughly conclude this test; for both films some intermixing of the Eu and Mn layers is observed, the intermixing is complete if the film was annealed ("F-

Mn"), without annealing the intermixing is partial. Rough assessments of the roughness of the films, depending on the slope of the curve, indicate that annealed film, "F-Mn" is more flat.

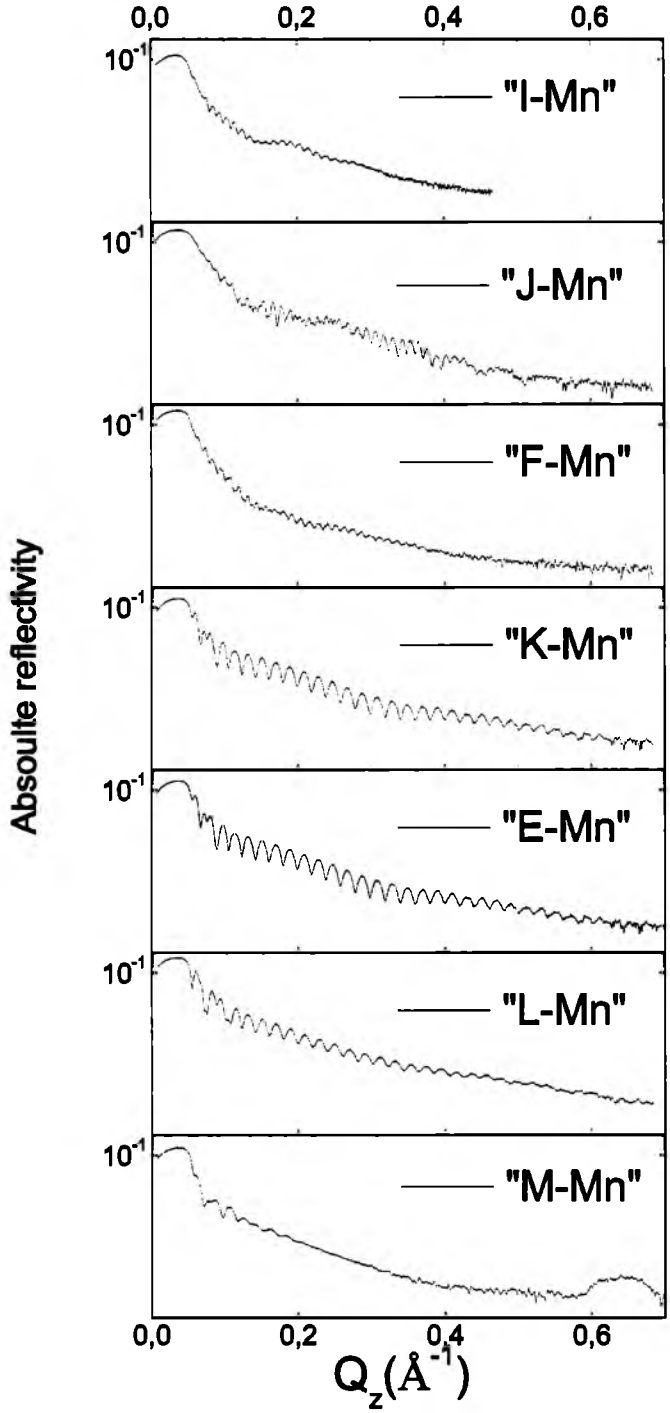

Figure 3.1.4 Specular reflectivity of "I-Mn", "J-Mn", "F-Mn", "K-Mn", "E-Mn", "L-Mn" and "M-Mn" films.

The X-ray reflectivity measurements clearly indicate the formation of a uniform Eu-Mn layer covering the (GaAs,Si)/Mo substrate for almost all examined concentrations. Well-defined oscillations in the XRR patterns (see Figure 3.1.4) for majority of examined concentrations of Eu and Mn allowed for fitting and calculations of the thickness of the films, but also for the calculations of the electron density profiles (see Figure 3.1.5) and roughness of the films. The calculated thicknesses are in good agreement with the assumed value of deposited material (see Table 3.1.2).

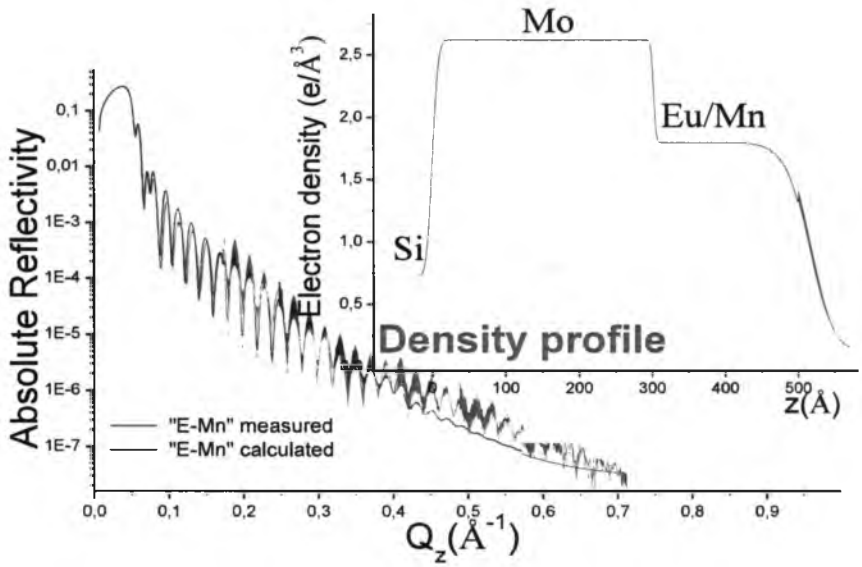

Figure 3.1.5 Electron density profile calculated from the specular reflectivity for "E-Mn" film.

Table 3.1.3 Parameters obtained from the calculations for the "E-Mn", and "L-Mn" films.

Sample name	Assumed stoichiometry	Assumed thickness [Å]	Calculated thickness [Å]	q_c [Å^{-1}]	Calculated roughness [Å]	Calculated absorption (10^{-7})
"E-Mn"	$EuMn_3$	181.6	168.59	0.05027	23.4992	31.2397
"L-Mn"	$EuMn_5$	140.1	159.2	0,0463	0,7	27.24

To determine the crystallographic properties of the films the XRD measurements have been carried out, by employing Phillips Expert XRD system. The measurements have been performed in θ-2θ geometry. Obtained results have been presented in logarithmic scale due to the presence of very strong diffraction peaks from the substrate together with very weak diffraction peaks form other phases which originate from the film.

For several different films prepared in two different growth modes; co-deposition "G-Mn", multilayer deposition "J-Mn", "F-Mn", and "E-Mn" the diffraction patterns indicate the presence of some ordered phases. Some of those phases have been identified. The strongest peaks in the diffraction pattern originate from the substrate (GaAs or Si) but the patterns contain also weak peaks derived from gold and molybdenum which are the components of protective layer. Nevertheless in the diffraction patterns, in addition to those recognized peaks, some unidentified peaks appeared. The results indicate a formation of ordered phases between the components of the films.

In obtained XRD patterns (see Figure 3.1.6 "E-Mn"), besides the peaks coming from the substrate or the cover layer series of peaks associated with this newly formed phases can be seen. *Ex-situ* XRD analysis, using the Fullprof and HighScore Plus programs, indicates that the "E-Mn" film crystallizes into a hexagonal structure in the P6/mmc space group with lattice parameters a = 0.72 nm and c = 1.07 nm [74].

For different, Mn rich compositions, we clearly see the formation of other Eu_xMn_y compounds. For one of the films the hexagonal $EuMn_5$ phase has been found with the lattice parameter estimated as a = 5.20Å, c = 4.01Å. In another "G-Mn" film the XRD pattern indicate formation of densely packed face centered cubic structure where the lattice parameter was estimated as a = 6.98Å. In that case the europium atoms form a frame of the unit cell.

Worth noting is the difference in the diffraction spectra between samples "J-Mn" and "F-Mn". One of the samples, "F-Mn" was annealed at 200°C and later covered by a protective coating, whereas the second one "J-Mn" had been covered as it was grown. Explicitly it is evident that annealing at even at relatively low temperature of 480 K leads to the formation of new phases.

Table 3.1.4 Estimated crystal structure and lattice parameters of new phases.

Assumed stoichiometry	Structure	Lattice parameter
$EuMn_2$	Hexagonal	a = 7.2 Å c = 10.7 Å
$EuMn_5$	Hexagonal	a = 5.20Å c = 4.01Å
Eu_6Mn_{23}	Cubic	a = 6.98Å

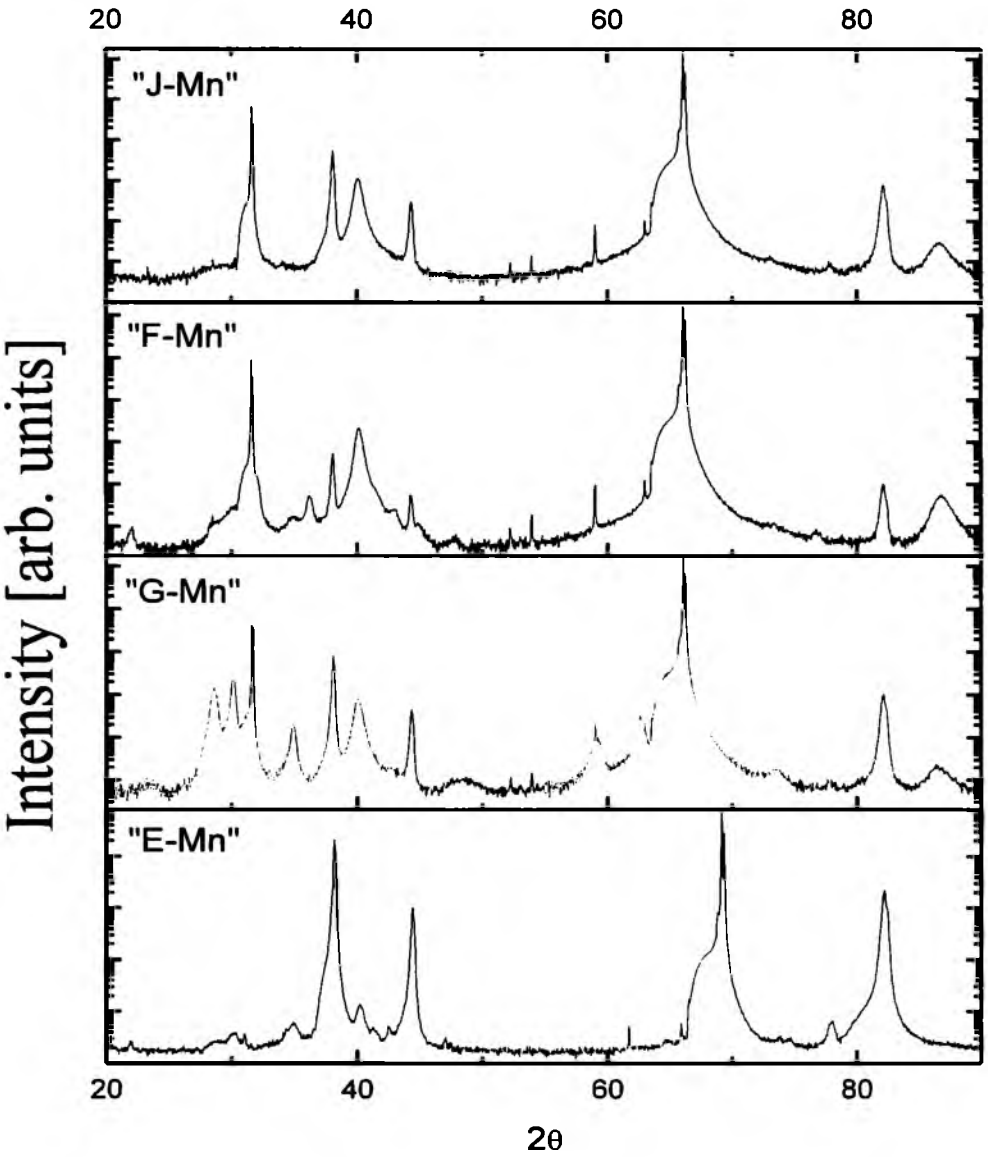

Figure 3.1.6 XRD patterns for "J-Mn", "F-Mn", "G-Mn", and "E-Mn" films.

We anticipate that different Eu_xMn_y compounds can be formed in such cubic structure. We presume that, depending on the number of manganese atoms packed inside such europium frame, similarly as in case of gadolinium based compounds ($GdMn_2$ or Gd_6Mn_{23}), $EuMn_2$ and Eu_6Mn_{23} phases can be realized. That is in good agreement when comparing with other manganese compound formed with other rare earths; among all other structures those two stoichiometries are preferable (see Table 2).

3.1.2 Electronic Structure

Although the motivation for our work was to examine the possibility of formation of Eu_xMn_y compounds few additional effects will be discussed. In this section we will focus on the reaction between Eu and Mn layers. Specifically, the Eu 3*d*, Eu 4*d* and Mn 2*p* core levels, and relative changes in their intensities will be analyzed. Particular attention will be paid to the changes in Eu valency which strongly affect the magnetic properties of Eu_xMn_y films. Also observed for Eu-Mn system reversible valance transitions induced by temperature changes will be in detail described.

Typical for the Eu-Mn system XPS survey spectrum has been shown in the Figure 3.1.7; the analysis indicates that only the deposited elements are the components of the film, no oxygen, carbon or other contamination is visible.

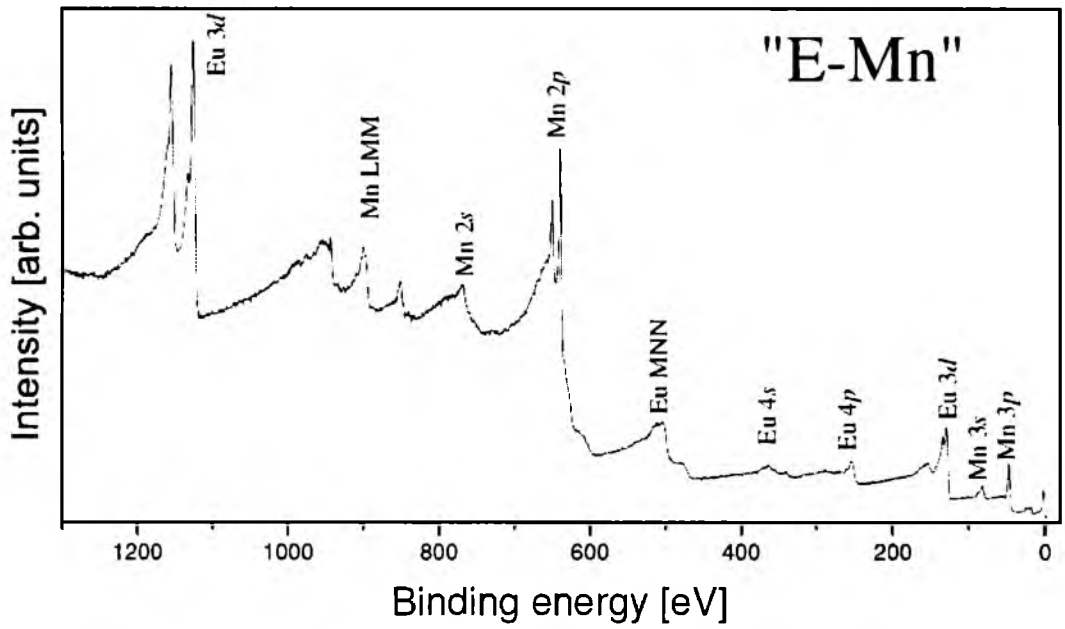

3.1.7 Survey spectrum for the "E-Mn" film after the deposition process.

Both Eu and Mn layers after deposition exhibit typical metallic behavior which has been confirmed by the analysis of the position and shape of both manganese and europium photoemission lines. We have analyzed Mn 2*p* doublet which shows the lines typical for Mn metal and Eu mutiplets. The mutiplets are formed due to the exchange splitting with the spin of the 4*f* shell and spin-orbit coupling which is of the same order. Additionally the final state effects lead to additional splitting, which is particularly important for the Eu 4*f*

photoemission. Well-defined exchange splitting, characteristic for metallic europium [75], observed in the Eu 4*d* line strongly depends on the thickness of the Eu layer; the splitting is stronger when the Eu layer is thicker (Figure 3.1.8 (a)). Particular thickness in samples "E-Mn" and "J-Mn" is respectively equal 12.9 and 4 Å. This have been also completed by the Eu 3*d* core level and valence band spectra analysis, where a single line at 2.2 eV comes from the Eu^{2+} 4*f* level (see Figure 3.1.8 (b)). The 4*f* multiplet coming from trivalent europium is known to form a broad structure in the binding energy range 6-12 eV [76].

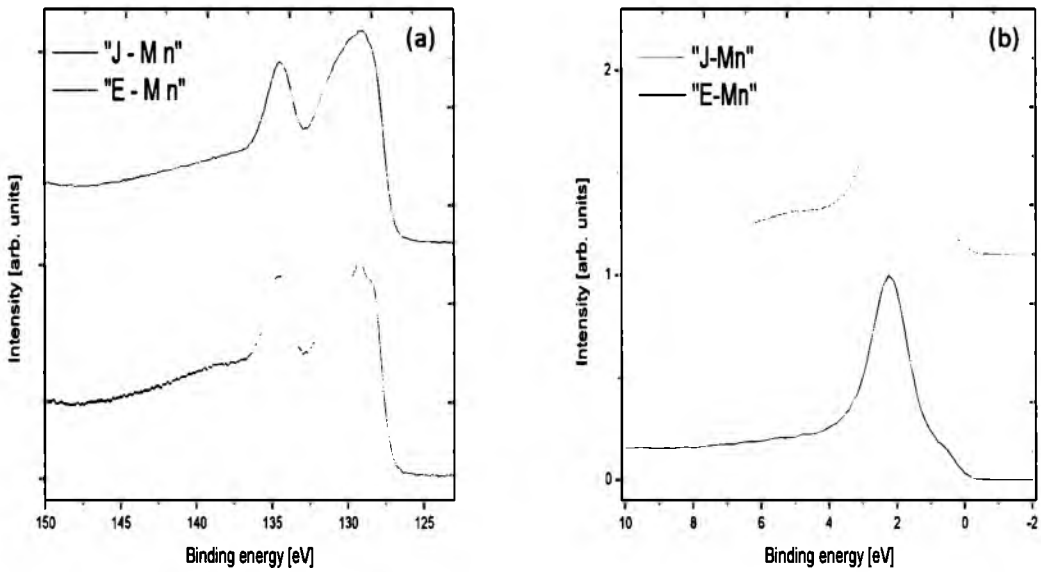

Figure 3.1.8 XPS spectra for (a) Eu *4d*, (b) Valance band for the "E-Mn" film.

During or after annealing process the manganese Mn 2*p* line shows or small shifts up to 0.1 eV, or no sign of shifting and only slight change in its shape; this clearly that during the annealing process manganese does not oxidize even if it is the most outer layer in the multilayer structure. In contrary, during annealing changes of Eu mutiplets are significant. A valence transition from Eu^{2+} to Eu^{3+} was observed for samples rich in Mn. In Figure 3.1.9 the Eu 3*d* and Eu 4*d* (smaller surface sensitivity) lines have been plotted for samples: "C-Mn", "E-Mn", "G-Mn", "M-Mn", "B-Mn", "L-Mn". For the "E-Mn" and "G-Mn" film where calculated Eu/Mn ratio was respectively 0.5 and 1.4 the valence transition to Eu^{3+} state has not been observed. A small shift to higher binding energies and slight change of shape can be detected.

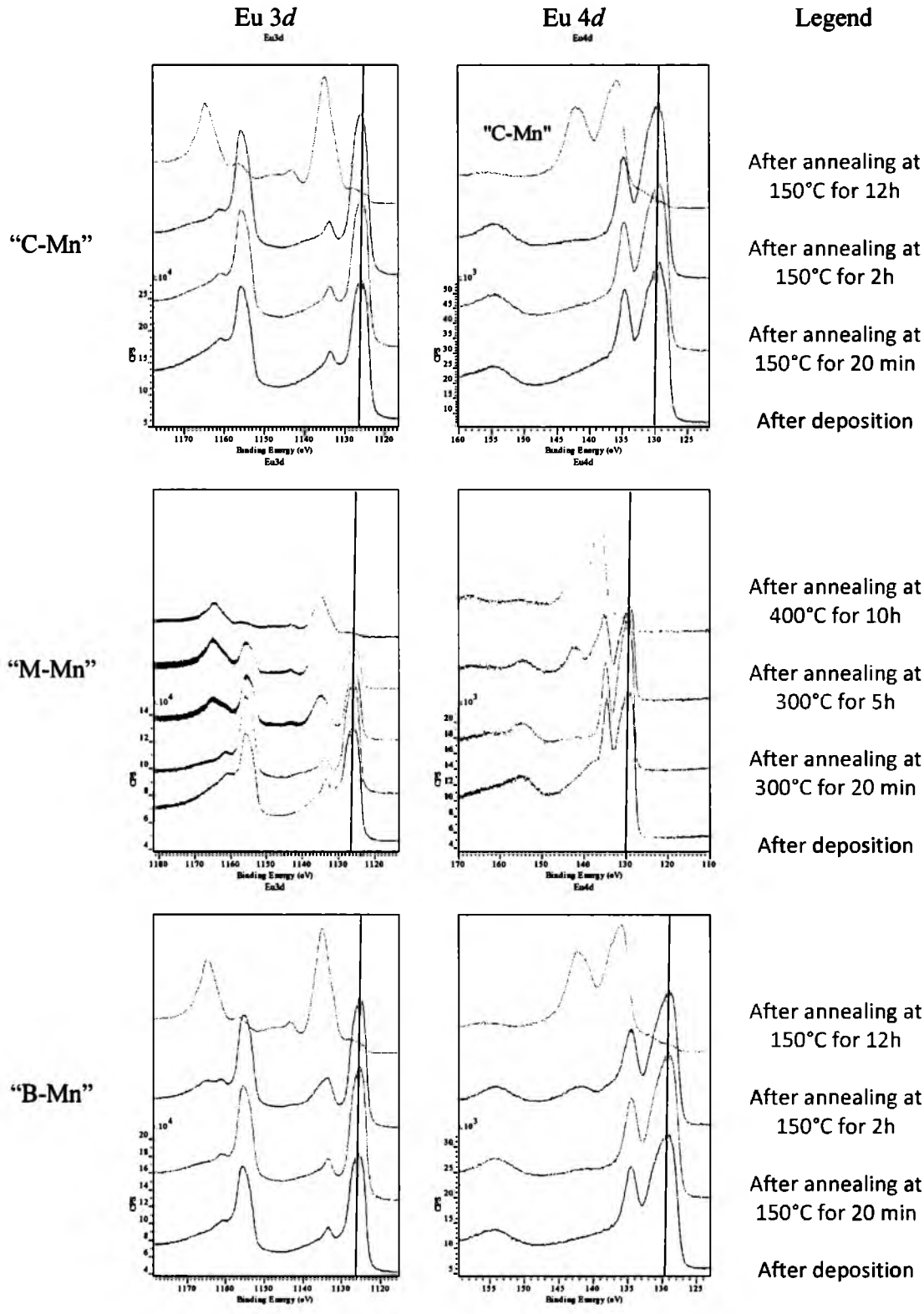
Eu 3d
Eu 4d
Legend
"C-Mn"
"M-Mn"
"B-Mn"
"C-Mn"
After annealing at 150°C for 12h
After annealing at 150°C for 2h
After annealing at 150°C for 20 min
After deposition
After annealing at 400°C for 10h
After annealing at 300°C for 5h
After annealing at 300°C for 20 min
After deposition
After annealing at 150°C for 12h
After annealing at 150°C for 2h
After annealing at 150°C for 20 min
After deposition
Binding Energy (eV)
Eu3d
Eu4d

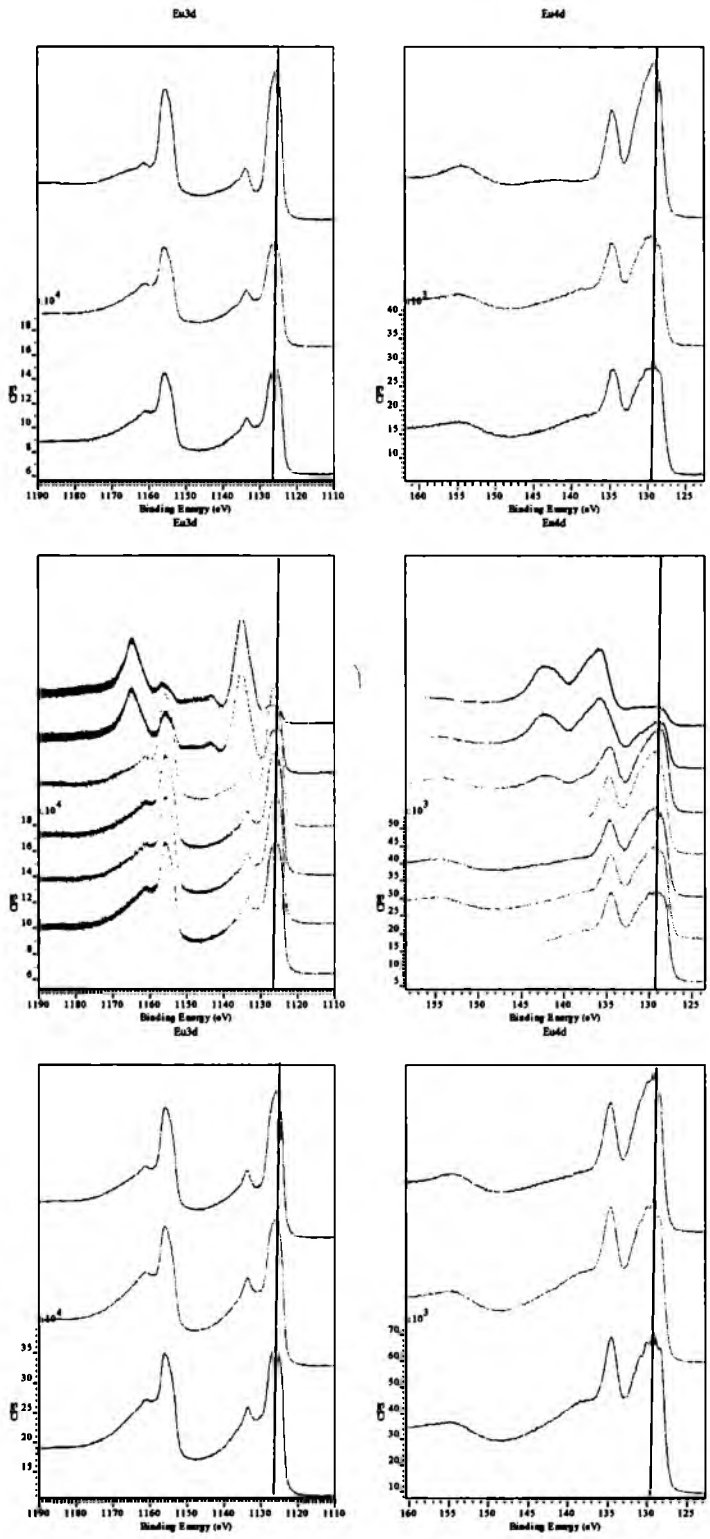

Figure 3.1.9 Eu 3*d* and Eu 4*d* core levels for "C-Mn", "M-Mn", "B-Mn", "E-Mn", "L-Mn" and "G-Mn films.

In case of other composition where Eu/Mn ratio was 0.2 (film "M-Mn"), 0.42 (film "L-Mn") and 0.63 (film "B-Mn") a process of the $Eu^{2+} \leftrightarrow Eu^{3+}$ valence transition was observed during the annealing, however for selected compositions (which have been marked in the Figure 3.1.9) the divalent europium was observed by the low intensity contribution to the 3*d* and 4*d* spectra. This fact may be related to the surface valance transitions observed in some Eu bulk compounds and $EuPd_3$ thin films [77].

The relative changes of the Eu/Mn ratio, derived from the XPS lines, indicate mixing of the Eu and Mn layers (see Figure 3.1.10). Such conversion can be done due to the fact that the inelastic mean free path of the analyzed photoelectrons is of the order of 1-2 nm. Therefore detected photoelectrons are emitted from a few of intermixed Eu and Mn layers.

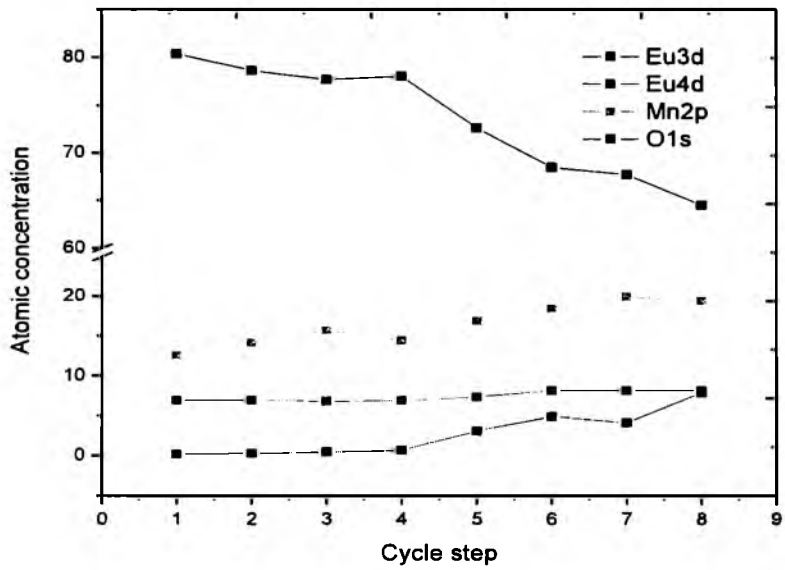

Figure 3.1.10 Relative changes of the Eu 3d, Eu 4*d* Mn 2*p* and O1*s* derived from the XPS lines for the "L-Mn" film. The "cycle step" means respectively measurements preformed 1 after deposition, 2 at room temperature (~2h after deposition), 3 at 2.5A (~150°C) for 20 min, 4 at 2.5A (~150°C) for 1.5h, 5 at 2.5A (150°C) overnight, 6 after cooling down, 7 after additional annealing at 2.5A (250°C) overnight, 8 after annealing at 2.5A (250°C) over next night.

Due to much shorter mean free path of photoelectrons emitted from Eu 3*d* level than those coming from the Eu 4*d* level one observes much stronger variation of the 3*d* multiplet intensity as a result of Eu and Mn layers mixing.

An increase of the relative oxygen content was observed in the survey spectra after a long (12h) annealing. We presume that thin layers of EuO and Eu_2O_3 are formed at the surface of the films. However, in the measured XRD patterns only for several Eu_xMn_y films some traces of EuO and $EuO_{1.5}$ phases and a sign of Eu_2O_3 phase were detected. The presence of EuO phase is also visible in the *ex-situ* temperature dependent magnetization studies which will be discussed later.

XPS depth profile

XPS depth profile studies have been performed for selected films after several weeks or months from the growth. Partial oxidation of the film surface was observed. Even for the Eu_xMn_y alloys where the europium was divalent the Eu^{3+} ions have been detected at the film surface, nevertheless after short argon sputtering trivalent europium has been removed and Eu^{2+} states appeared (Figure 3.1.11).

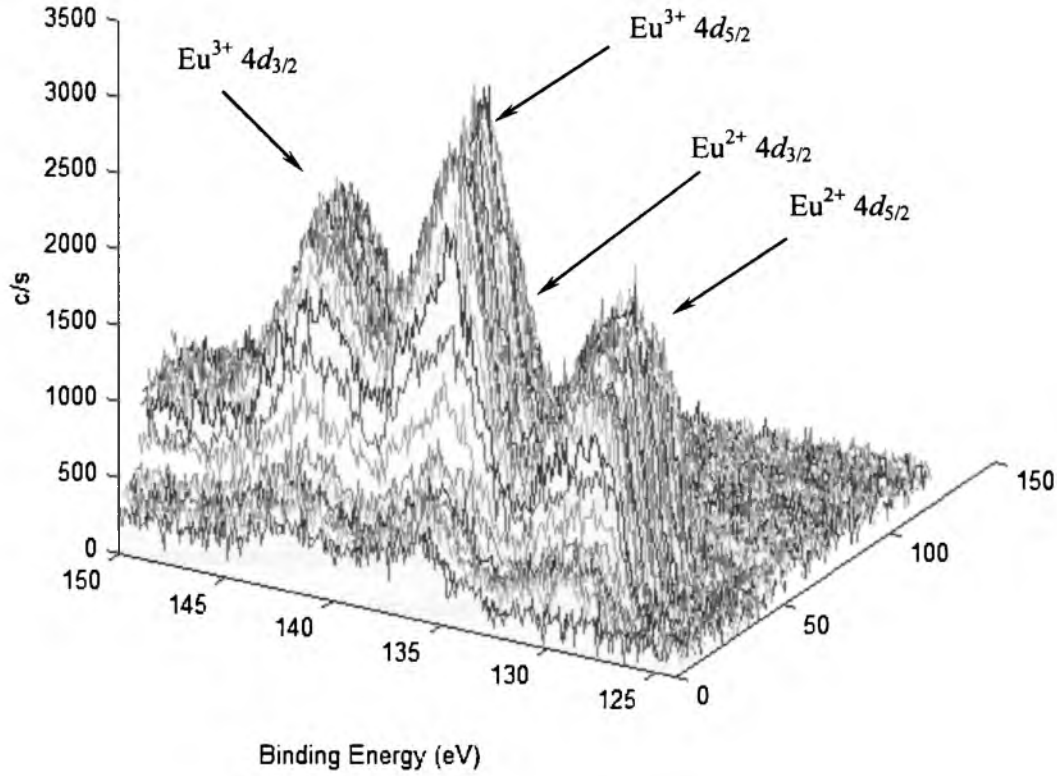

Figure 3.1.11 Changes of the Eu *4d* photoemission line - depth profile for "K-Mn" film.

The removal of the trivalent europium species is not the only reason for that effect as we observed in several compounds where Eu is trivalent its reduction by Ar sputtering. Such

effects was found e.g. in EuF_3. We used for depth profiling ion energy of 2 keV and this energy was found to cause significant reduction of the Eu chemical state, but in trivalent compound, like EuF_3 even long sputtering caused coexistence of both components in the Eu XPS spectra. Similar composition of the Eu 4*d* and 3*d* spectra during depth profiling was found in the Eu_xMn_y films with composition Eu/Mn less than 0.3. It may confirm the bulk character of the trivalent Eu state and a relatively uniform composition within the film. Formation of trivalent Eu ions is thus related to mixing with Mn at its high coordination number with Mn atoms. The effect resembles that found for Eu-Ni [78, 79] and Eu-Pd systems [77, 80] where only compounds with high transition metal content show trivalent europium. The residual content of divalent ions in those systems may be connected to surface valence transition [77] or to formation of the film of EuO. However, it is worth mentioning that even for the cleaved in vacuum single crystals of EuF_3 a divalent europium was found on the surface and this effect disappeared only for the ultrathin films of this compound [90]. For example for the "K-Mn" films the depth profiles (see Figure 3.1.12) confirmed the presence of trivalent europium within the films, although the composition Eu/Mn was generally stable only in the part of film thickness.

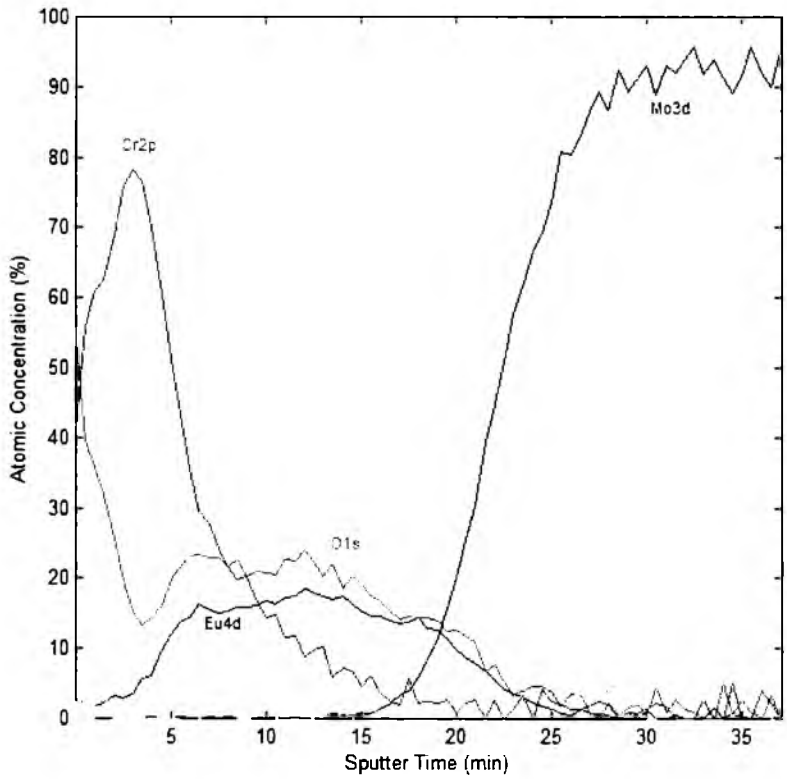

Figure 3.1.12 XPS depth profile performed for the "K-Mn" film.

Island formation

The annealing of multilayer grown Eu_xMn_y films leads to mixing of the layers and in some cases to island formation. Island formation has been confirmed by the XPS as well as AFM measurements for selected studied samples. In Figure 3.1.13 examples of the XPS survey spectra of the thin film series both after deposition and after annealing have been presented.

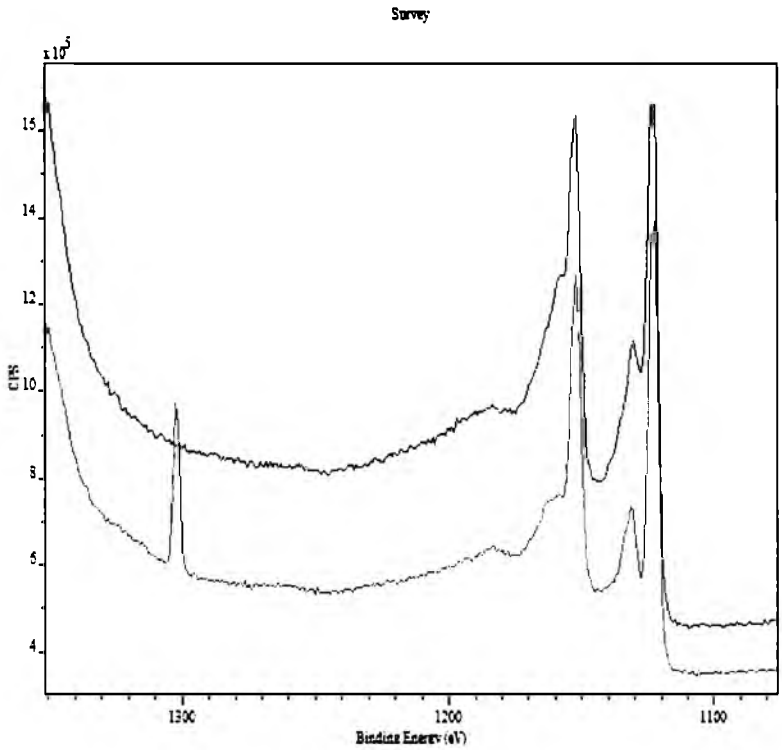

Figure 3.1.13 Part of XPS survey spectra of the "P-Mn" film grown on MgO.

The intensity of the magnesium (MgO substrate) 1*s* line during the annealing process rapidly increases, indicating that the chemical composition of the surface of the film is changing and the Eu_xMn_y islands are forming. For the "thick series" of Eu_xMn_y, the formation of islands could not be determined from the XPS measurements due to the thickness of the deposited material and the value of electron inelastic mean free path which can be estimated as 20-30 Å for the high kinetic energy photoelectrons. However, *ex-situ* AFM measurements of the film covered by Au shows that uniformly distributed regular islands of about 30nm in size are formed, as shown in Figure 3.1.14. The roughness of the film was about 40Å-60Å.

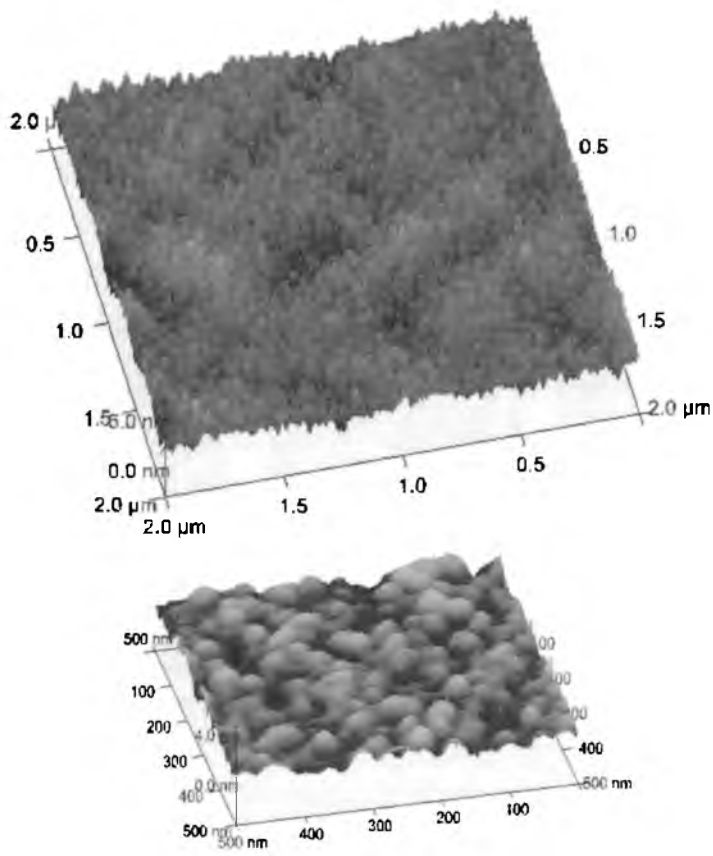

Fig 3.1.14 AFM image of "R-Mn" film covered by Mo/Au protective layer.

Reversible valance transitions due to the heat treatment for the oxidized film.

The reversible temperature induced valence transitions were observed for selected films (see Figure 3.1.15). Here we focused on detailed analysis of 4.3nm thick "N-Mn" film where relatively high amount of oxygen was observed after a deposition process. In that case manganese oxidized after the reaction and long annealing. Similar reversible $Eu^{2+} \leftrightarrow Eu^{3+}$ valence transitions were previously observed for the Eu-Si system [81, 82]. The reversible switching of the Eu ion valency, in the W. A. Henle et.al studies, was achieved by O_2 exposure and mild heat treatment of the 1Å thick Eu layer grown on Si substrate; the authors associate the transitions with changes of the surface stoichiometry. Similar behavior was observed at 400°C for the 41Å thick $EuPd_3$ layers grown on MgO(001) [77].

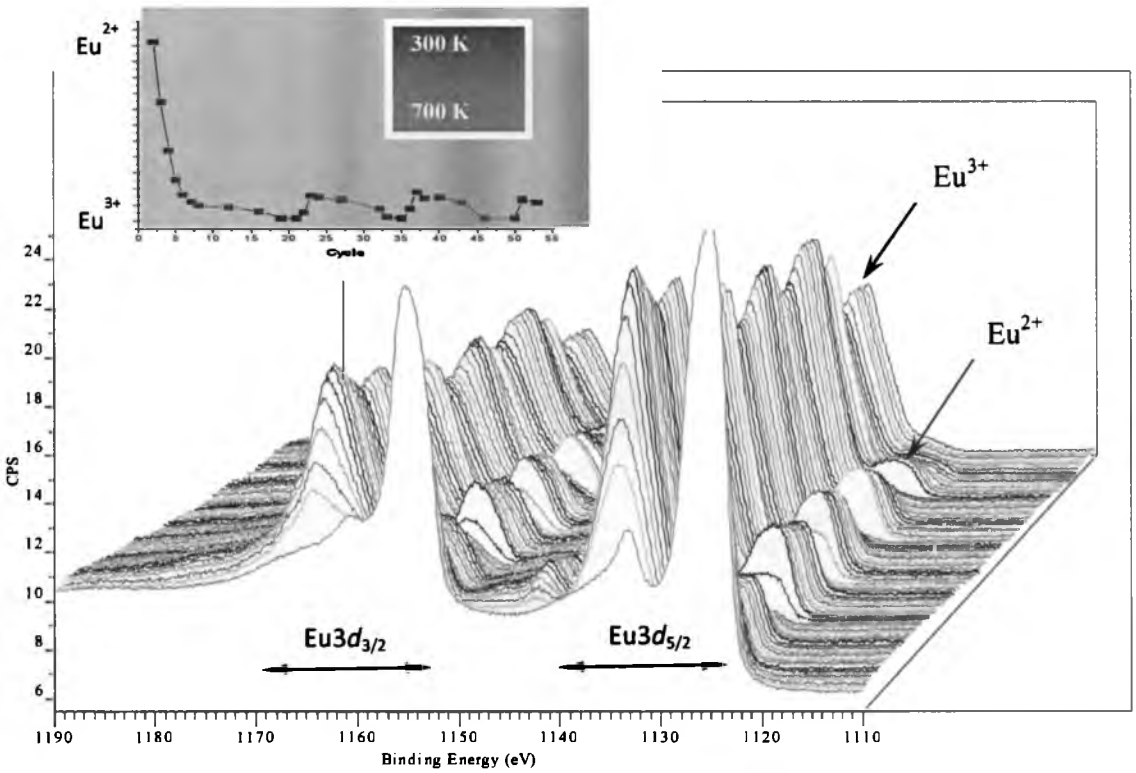

Figure 3.1.15 Reversible Eu valance transitions evaluated from the Eu3*d* photoemission line for "N-Mn" film.

In our studies the oxidized "N-Mn" layer has been studied in terms of the influence of heat treatment on the valency of europium. The relative atomic ratio of the film components, calculated form the Eu 4*d*, Mn 2*p* and O 1*s* core levels indicate mixing of the Eu-Mn layers and the oxidation of the film. The temperature dependent measurements were performed for several days with the temperature changing as it is shown in the Figure 3.1.15 (inset graph). On the inset graph the relative changes of Eu^{2+}/Eu^{3+} have been presented. The majority of the Eu ions after first annealing process remain in the Eu^{3+} valency states, but at elevated temperatures the excitation of Eu^{2+} states was observed. Annealing at elevated temperatures leads to increase of the intensity of the Eu^{2+} states while the reverse "cooling down" process causes opposite $Eu^{2+} \leftrightarrow Eu^{3+}$ transition. The excitation of the Eu^{2+} states tends to decrease with the temperature increase but the reversible changes even after annealing at high temperatures do not disappear. Changes in the Eu 3*d* and spectra have been presented in Figure 3.1.15. Such behavior, taking into account published reports [77, 81, 82], is rather an individual property for the thin layer of europium or rather its oxide in some unique environment. Despite the fact that oxygen seems to play an important role in such switching

we observed the reversible switching of europium valency also for films where the top manganese layer of the film was in pure metallic state. The most likely origin of the behavior, which appears to be interesting also for applications, is the temperature dependence of the surface valence transition related Eu_2O_3 terminating the Eu-Mn films.

Valance transitions due to deposition of additional layer of Mn and other elements

The deposition of additional manganese layer on the top of mixed europium and manganese layer leads to the change of valency state of europium form Eu^{3+} to Eu^{2+} as it is shown in the figure 3.1.16. We present more surface-sensitive europium 3*d* level spectra for the analysis of that effect. In the figure 3.1.16 the Eu3*d* level is presented, after a deposition proces the Eu3*d* is in a 2+ state and exhibit the properties of pure metallic europium (a). After the annealing process the mixing of the layers leads to almost complete change of europium valency state (b), the Eu^{2+} state is still visible in the spectra but the intensity of the peak is relatively low comparing to the Eu^{3+} state. The deposition of additional layer of manganese on the top of reacted Eu-Mn films causes the changes in the chemical composition of the film surface and leads to the changes of electronic structure of europium (c). Explanation of the phenomenon will be discussed based on additional research conducted for the system Eu-Fe.

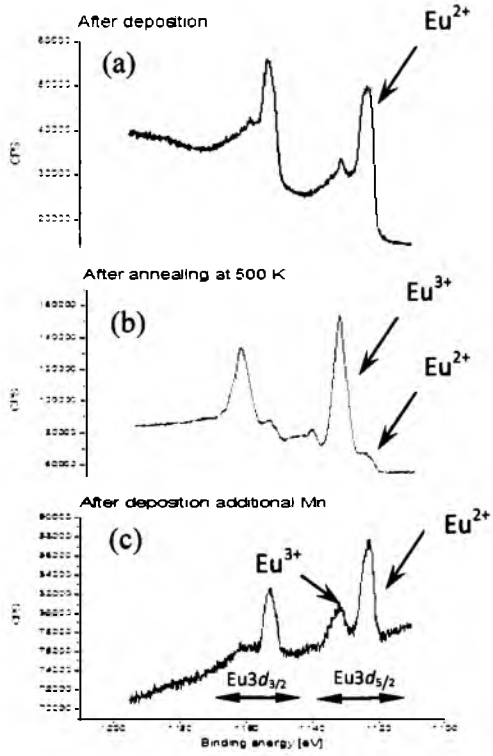

Figure 3.1.16 Valance transition due to deposition of additional Mn layer on the top of annealed layer.

3.1.3 Magnetic and transport properties

Temperature-dependent SQUID measurements were performed in both zero-field cooled and field-cooled modes for different applied fields (10, 50, 100, 1000 [Oe]). The field was typically applied parallel to the surface of the film, but the investigations where the field is applied perpendicular to the film have been also performed for selected samples.

In presented in this chapter results, obtained from the SQUID measurements, the diamagnetic contribution of the films substrate has been subtracted for both temperature (M-T) and field (M-H) dependence of magnetic moment.

For measurements performed in both FC and ZFC modes significant difference seen as irreversibility in the M-T curves have been observed. Figure 3.1.17 present the temperature dependence of magnetic moment of Eu-Mn films measured at 100 and with the filed applied parallel to the surface of the films. For selected films the FC and ZFC modes have been presented.

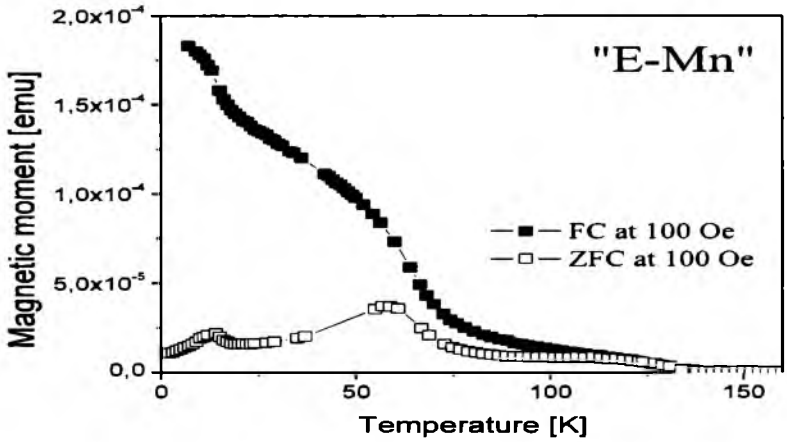

(a)

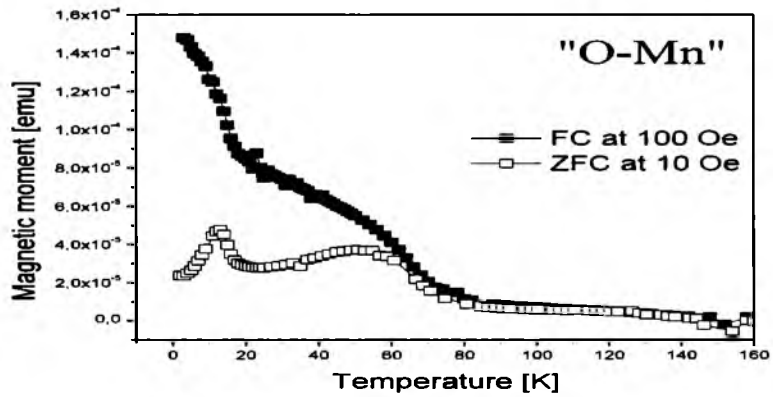

(b)

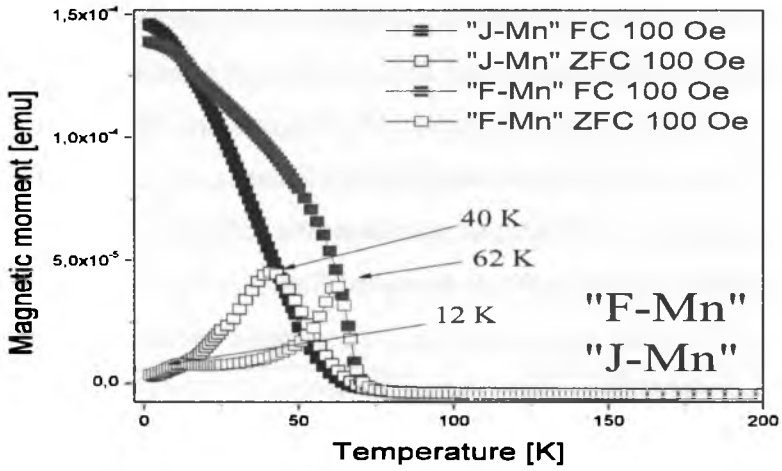

(c)

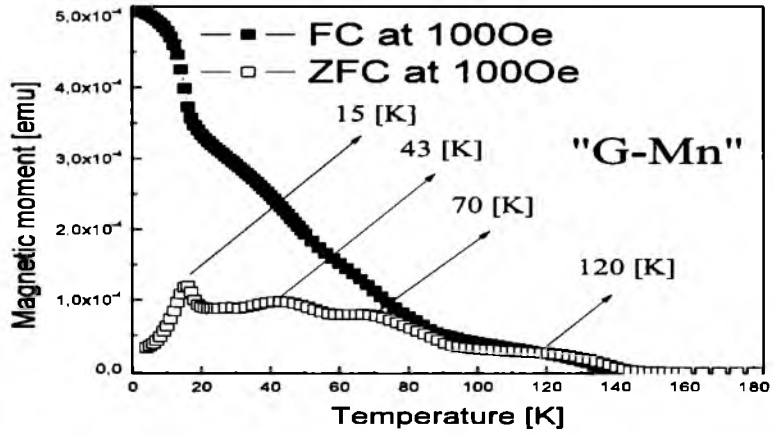

(d)

Figure 3.1.17 Temperature dependence of magnetic moment at 100 Oe for selected films: (a) "E-Mn", (b) "O-Mn", (c) "F-Mn" combined with "J-Mn", (d) "G-Mn".

Transitions to magnetically ordered states, in a ZFC mode seen as sharp maxima in the M-T curve occurred at approximately at 12-15K, 60-70K, and 120 – 140 K (see Figure 3.1.17 (a), (b), (c), (d)). The transition at 12 K observed for the annealed sample can be linked to the $EuMn_2$ phase [74, 83]. The observed behavior is partly caused by the presence of the EuO species in the film. The literature data [87, 88] and new results [91] show similar ferromagnetic-like transition at about 70 K. The transition at 140 K can also be due to the EuO being oxygen-deficient [91]. The abrupt increase around 15 K, with its counterpart in a form of a maximum in the zero-field cooled magnetization run, can be coercive field than those reported in EuO films.

The additional peak at 43 K in ZFC curve for the film grown in co-deposition - "G-Mn" film, process can be relate to presence of another magnetically ordered Eu_xMn_y phase. The separation in M-T curves measured in FC and ZFC modes imply presence of particles in the film [84-86]. Above the ferromagnetic transitions the temperature dependence of magnetic moment measured in ZFC mode retraces corresponding FC curves for all examined films.

The hysteresis loops revealed a decreasing value of coercive field with increasing temperature (see Figure 3.1.18 (a), (b), (c), (d), (e)) for all examined films.

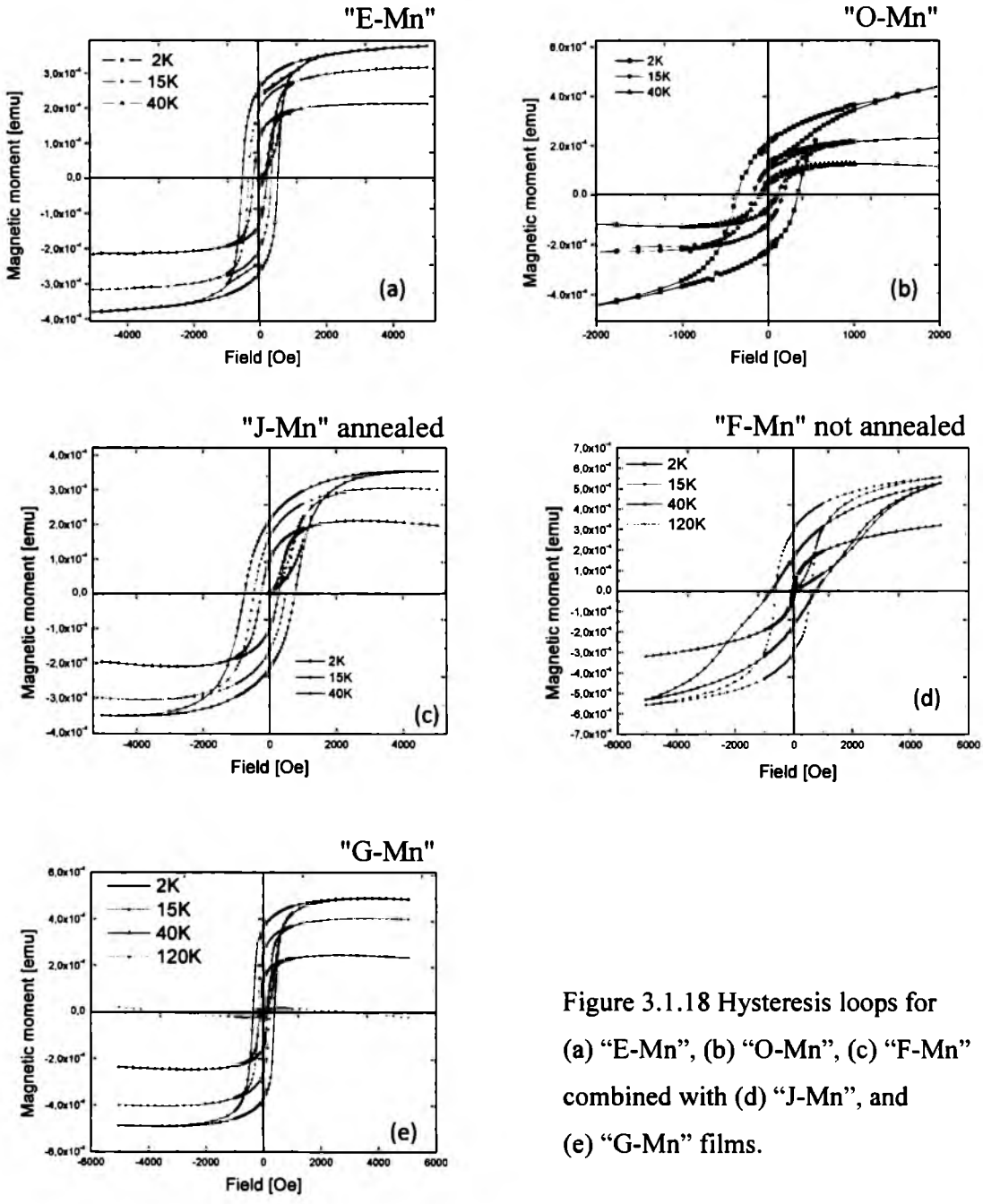

Figure 3.1.18 Hysteresis loops for (a) "E-Mn", (b) "O-Mn", (c) "F-Mn" combined with (d) "J-Mn", and (e) "G-Mn" films.

The hysteresis loops in the "E-Mn" film ($EuMn_2$ compound) show higher coercive field than those reported in EuO films. At 2 K, the value of $4\pi M_s$ was estimated to be on the level of 1.5kG. The presence of a hysteresis loop, and the relatively low value of saturation magnetization, suggest a ferrimagnetically ordered state between the Eu and Mn atoms or frustration among spins. The significant difference between ZFC and FC measurements of the magnetic moment as a function of temperature, and the fact that the $EuMn_2$ film crystallizes into a hexagonal structure P6/mmc space group, strongly suggest frustration among the spins. Such a supposition is further supported by the fact that the sample cannot be saturated out of plane, even in the field of 7 T. It is worth noting that the magnetic studies were undertaken several weeks after sample growth, whereupon partial oxidation of the $EuMn_2$ grains could lead to the formation of an oxygen deficient EuO species.

Temperature dependence of magnetic moment measured in low fields (10, 50, 100 Oe) have been performed for the "O-Mn" film grown in a MBE system placed at University of Silesia under similar as in Colorado Springs conditions (see Figure 3.1.20).

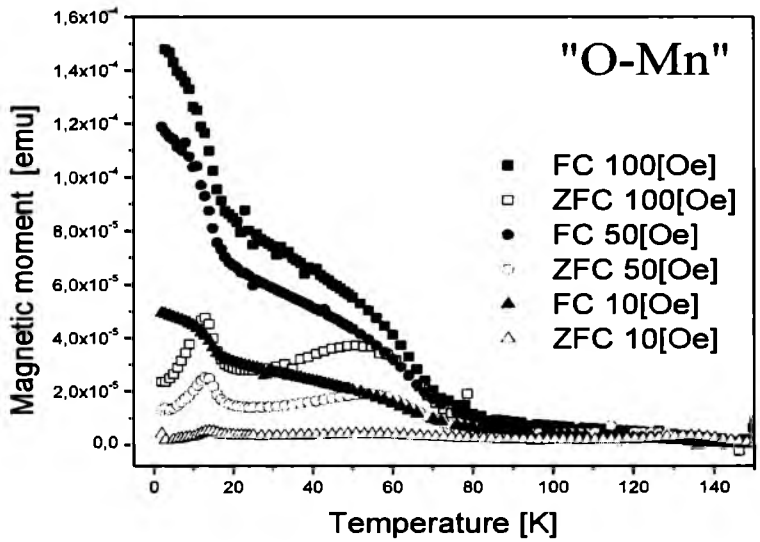

Figure 3.1.19 Temperature dependence of magnetic moment measured in relatively low fields in FC and ZFC modes for the "O-Mn" film.

The irreversibility in FC – ZFC curves appear to be as in other samples (see Figure 3.1.17 (b)), but field dependent measurements allow us for more precise analysis of the behavior of M-T in the ZFC mode (see Fig 3.1.19). Changes in the relative intensity ratio of the peaks as well as small shifts of the peaks have been observed. The significant change is observed for

measurement performed at 10 Oe where the relative intensity of the peak at around 140 K rapidly increased in comparison to measurements at 50 and 100 Oe. Such behavior is thought to be due to presence of superparamagnetic regions (for selected films the AFM images indicate formation of island) in the film. Again for all examined fields above the transitions negligible changes between FC and ZFC curves can be observed.

With the field applied perpendicular to the film surface both M-T curves and hysteresis loops show significant differences when comparing to the measurement performed with the field applied parallel to the film surface as it have been shown in fig 3.1.20.

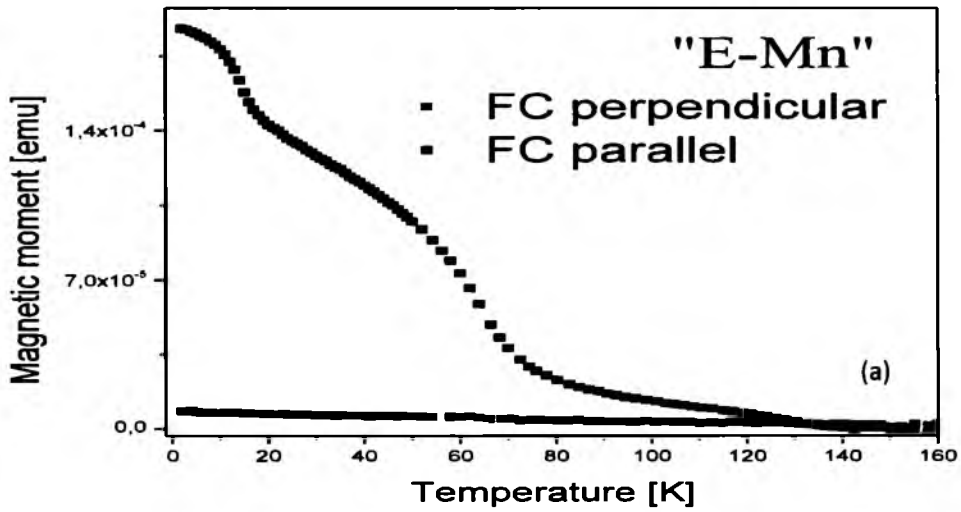

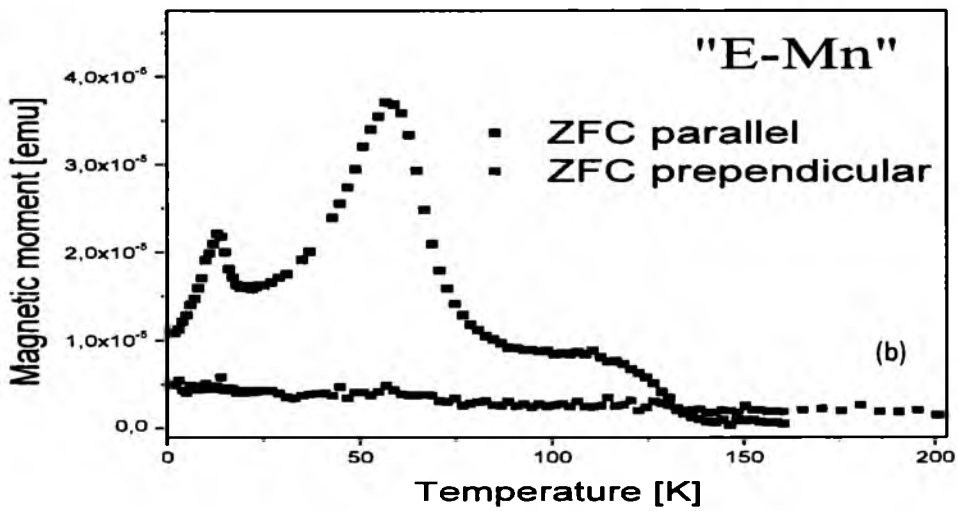

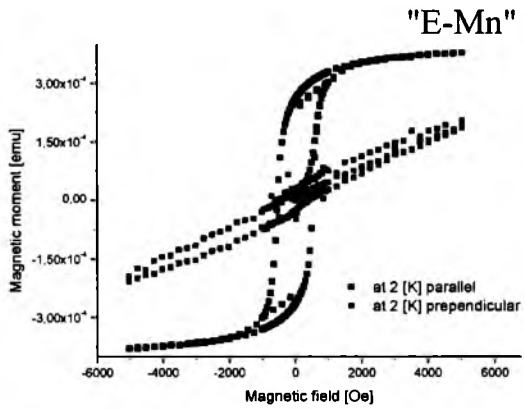

(c)

Figure 3.1.20 Temperature dependence of magnetic moment with the field applied parallel and perpendicular to the "E-Mn" film surface; (a) in FC mode, (b) ZFC mode, (c) field dependence of magnetic moment measured at 2K with the field applied parallel and perpendicular to the "E-Mn" film surface.

Figure 3.1.21 shows the temperature dependence of the electrical resistivity measured represented by the "E-Mn" - $EuMn_2$ film. There are a few interesting features worth noting. The most important is an anomaly in the temperature dependence of the electrical resistivity, namely a maximum of resistivity near room temperature. None of the magnetic transitions were reflected in the resistivity measurements, though the lowest temperature reached in this method was about 20 K. The effect of a well-defined maximum at high temperature was observed for the sample described in this work, and for other Eu-Mn films. The template Mo/Si, and the samples composed of the analogous substrate plus pure Eu and pure Mn layers, annealed at the same temperature, showed only typical metallic resistivity behavior without any such maximum or minimum at higher temperatures (see Figure 2.1.21 b). Thus, this behavior is related to $EuMn_2$ film (which has relatively good conductivity), and the observed maximum can be probably associated with valence fluctuation systems where similar behavior was reported. The confirmation of such a hypothesis requires further studies.

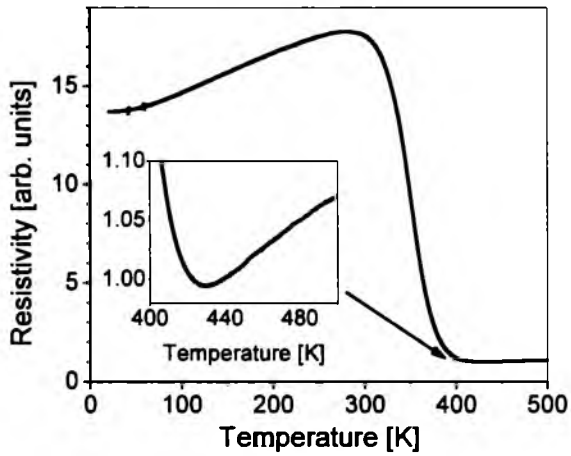

(a)

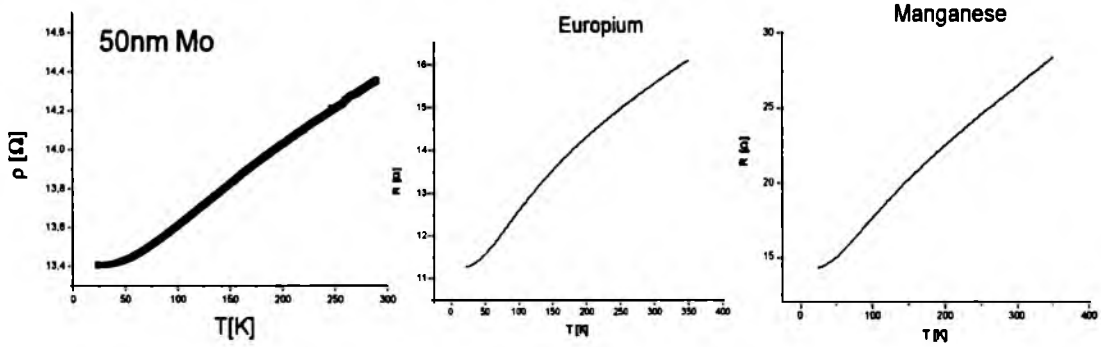

(b)

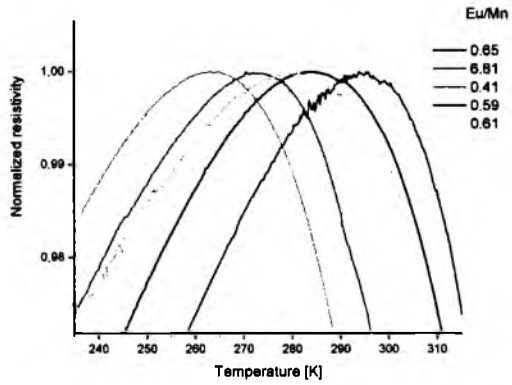

(c)

Figure 3.1.21 Temperature dependence of electrical resistivity of (a) "E-Mn" film - $EuMn_2$/Mo/Si film. Inset: temperature dependence of electrical resistivity narrowed to temperature range of 400 K up to 500 K, (b) Si/Mo substrate, pure europium and manganese layers, (c) narrowed to the peak region other films from the Eu-Mn system.

3.1.4 Conclusions

Changes in a polycrystalline structure of the films, monitored by RHEED, as well as calculations based on the x-ray reflectivity measurements indicate intermixing of the layers and possible formation of Eu-Mn based alloys. Well-defined oscillations in the XRR patterns can be observed for majority of examined concentrations together with the calculations of electron density indicate a formation of uniform Eu-Mn layer. The calculated thicknesses are in good agreement with the assumed value of deposited material. In obtained XRD patterns besides the peaks coming from the substrate or the cover layer series of peaks associated with this newly formed phases can be seen. The formation of Eu-Mn compounds was observed after annealing of Eu/Mn multilayers at relatively low temperatures (up to 400K). We anticipate that different Eu_xMn_y compounds can be formed in hexagonal and cubic structure. The lattice parameters have been estimated for a hexagonal structure of $EuMn_2$ as a = 7.2 Å, c = 10.7 Å for the hexagonal structure. The hexagonal $EuMn_5$ phase has been found with the lattice parameter estimated as a = 5.20Å, c = 4.01Å. Whereas lattice parameters for densely packed face centered cubic structure Eu_6Mn_{23} was estimated as a = 6.98Å. The hexagonal phases are formed more likely when europium is in divalent state whereas the cubic ones where europium is in 3+ state.

Valence transitions from Eu^{2+} to Eu^{3+} were observed for majority of Eu-Mn films with different concentrations of Eu and Mn. Nevertheless in the films where Eu/Mn ratio was equal 0.5 ("E-Mn" film) and one of co-deposited films with the Eu/Mn ratio 1.4 ("G-Mn") after annealing process europium remains in divalent state. The relative changes of the Eu/Mn ratio, derived from the XPS lines, indicate mixing of the Eu and Mn layers. The XPS depth profile confirm the bulk character of the trivalent Eu state and a relatively uniform composition within the film. The formation of islands has been observed via the AFM measurements but it has also been confirmed from the analysis of XPS spectra for relatively thin films. Some unexpected effects occurred during the XPS measurements; the first one was a possibility of excitation of divalent states europium as a result of heating and the second one a possibility of excitation of divalent states europium as a result of deposition of additional layer on the top of the film.

These results indicate that the magnetic behavior is associated with the divalency of Eu and that the behavior of the Eu-Mn films is an effect of frustration in the magnetic interactions.

Transitions to magnetically ordered states, in a ZFC mode seen as sharp maxima in the M-T curve occurred depending on film at approximately at 12 - 15K, 60 - 70K, and 120 -140 K. The transition at 12 K observed for the annealed sample can be linked to the $EuMn_2$ phase. The presence of a hysteresis loop, and the relatively low value of saturation magnetization, suggest a ferromagnetically ordered state between the Eu and Mn. SQUID measurements confirm the existence of magnetically ordered phases which can be attributed to $EuMn_2$ (with Eu^{2+} valency state) and indicate formation of another magnetically ordered phase with the transition to ordered state at 12K.

Presented M-T curves show thermomagnetic effect, the irreversibility in FC and ZFC branches of M-T curves is characteristic for typical of the blocking process for an assembly of superparamagnetic nanoparticles Additionally strong magnetic anisotropy has been observed in the measurements performed in field applied parallel and perpendicular to the surface of the film.

Finally the anomaly in the temperature dependence of the electrical resistivity, namely a maximum of resistivity near room temperature was observed for several Eu-Mn films. Observed maximum can be probably associated with valence fluctuation systems, but this assumption must be confirmed.

3.2 Eu – Fe system

Iron is the second transition metal selected for testing the reaction and therefore the possibility of forming new intermetallic compounds. The number of compounds that iron can form in the bulk form is larger than in case of manganese. Nevertheless it is still limited to several stoichiometries: RE_2Fe_3, $REFe_3$, RE_6Fe_{23}, RE_2Fe_{17} (for details see Table 1). Similarly as in case of manganese; the Eu_xFe_y films have been grown in a wide x and y range.

The deposition was performed by thermal evaporation of elemental sources: Eu (99.99 %), Fe (99.99 %), and Mo (99.95%), Au (99.999 %). Deposition of europium, and gold was done with the use of standard effusion cells, while the iron and molybdenum (used as a protective top layer) with the use of electron beam evaporator. Both iron and molybdenum have been grown from a 1.5mm thick wire. The films, as in case of manganese, were grown in two modes – in the multilayer form or in the co-deposition process, growth procedures has been described in details in Chapter 2.1.2. Growth of Eu_xFe_y films performed by deposition of multilayers of $(Eu/Fe)_x$ required a deposition of different thicknesses of individual Eu and Fe layers to achieve assumed concentration. Typical growth rates, optimally set for slow growth have been combined in Table 3.2.1. The thicknesses of analyzed films and their as-grown structure have been summarized in Appendix B.

Table 3.2.1 Growth rate for deposited materials for the Eu-Fe system.

Element	Growth rate [Å//s]
Europium	0.01-0.02
Iron	0.02-0.03
Gold	0.02-0.04
Molybdenum	0.02

3.2.1 Crystallographic structure

In this chapter the effects of several different experiments, specifically the result of RHEED, XRR, XDR studies, will be presented. The RHEED images have been obtained *in situ* and it has been the first criterion for assessing the quality of the layer. The question of mixing of the europium and iron layer and possibility of formation of ordered phase will be discussed in terms of the diffraction patterns obtained in RHEED measurements. Similarly as in case of Eu-Mn system, further structural characterization included analysis of the XRR measurements; and later the presentation of the XRD measurements.

Structural changes in the deposited layers were observed after the annealing process, see Figure 3.2.1. To demonstrate this effect several representative samples have been selected (see samples "A-Fe" – "E-Fe" in Table 3.2.1, for detailed information about the multilayer structure see Appendix B).

Table 3.2.2 Description of representative samples

Sample name	Assumed concentration (Eu/Fe ratio)	Thickness [Å]	Eu/Fe ratio after deposition*	Annealing process	Eu/Fe ratio after annealing*
"A-Fe"	Eu_2Fe (2)	88.2	2.6	100°C (~20h)	2.4
"B-Fe"	Eu_2Fe_{17} (0.12)	146.5	0.58	150°C (~24h)	0.63
"C-Fe"	$EuFe_5$ (0.2)	161.2	0.49	150°C (~24h)	0.35
"D-Fe"	EuFe (1)	147.5	1.58	100°C (~15h)	1.42
"E-Fe"	Eu_xFe_y	100	1.14	150°C (~15h)	1.16
"F-Fe" **	$EuFe_3$ (0.33)	115.4	0.74	100°C (~15h)	1.6
"G-Fe" **	Eu_2Fe (2)	176.5	3.25	100°C (~15h)	1.15
"H-Fe" **	$EuFe_2$ (0.5)	222.3	0.4	100°C (~15h) 250°C (~3.5h) 100°C (~15h)	0.29

* Eu/Fe ratio has been calculated from the results of the XPS measurements and will be discussed in Chapter 3.2.2.

** "F-Fe" – "H-Fe" films will be analyzed in Chapter 3.2.2 and 3.2.3

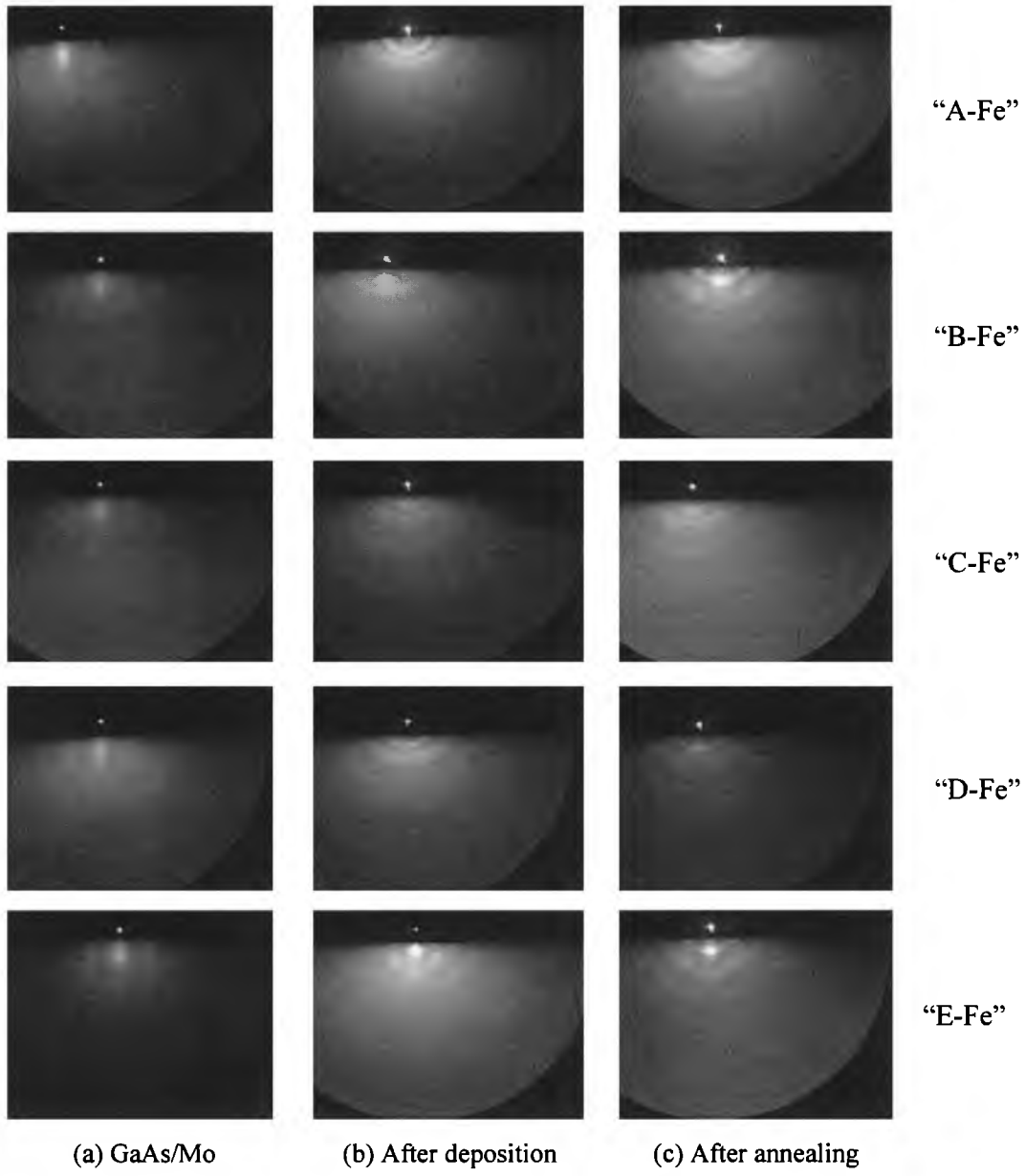

Figure 3.2.1 RHEED patterns obtained for Eu-Fe: (a) substrate, (b) as-grown, (c) after annealing.

In the first column of RHEED images the diffraction pattern of the substrate has been presented. The Mo film was prepared in sputtering system on Si or GaAs and was outgassed and cleaned (hydrogen ion bombardment cleaning) before the deposition of europium and iron layers. The diffraction pattern obtained after the annealing process (typically 100-150°C for about 15-24h as it has been summarized in Table 3.2.2) showed a different set of rings. The latter result indicates the formation of a polycrystalline film. For the series of films with total thicknesses larger than 100Å (films "B-Fe", "C-Fe", "D-Fe"), the RHEED pattern after

the deposition consisted of weak rings, the exception is the sample "E-Fe" grown in the co-deposition process, the after annealing process the RHEED patterns showing a slightly different set of rings. In contrast to the Eu-Mn system, no additional diffused spots of much higher intensity can be observed. The Eu-Fe films after the annealing process still have polycrystalline structure; although for films "A-Fe", "B-Fe", "D-Fe" different set of rings represent the surface atomic arrangement. Visible blur of the rings indicate amorphization of the surface or some other dynamical processes, for example not finite crystallization or more likely some oxidation of the film surface. For the film grown in the co-deposition process, the observed changes, similarly to the Eu-Mn co-deposited film, differ from the multilayer structures. The RHEED pattern shows a set of weak rings in addition to diffused spots of much higher intensity. After the annealing process, the film maintains in the polycrystalline structure with some texture. However, during the annealing process, the distances between diffused spots slightly changed which could indicate that present in the film texture is different comparing to the as-grown film, or that some additional strains occurred. Protective coating shows a polycrystalline arrangement of surface (weak system of rings) for all prepared films.

Determination of the crystallographic properties of the films, in the meaning of characterization of entire film not only the surface as it was in case of RHEED measurements, has been also carried out. The *ex situ* measurements performed after annealing process and after covering the film with the protective layer (depending on a film; Mo, Au, see Appendix B) were aimed at determination of the crystallographic structure as well as other properties (roughness, electron density) of the Eu_xFe_y films, for that the XRD and x-ray reflectivity techniques have been respectively applied.

The X-ray reflectivity measurements (see Figure 3.2.2) showed for almost all examined concentrations that more or less one uniform layer, consisting of a mixture of europium and iron, is formed on the top of (GaAs,Si)/Mo substrate. Well-defined oscillations in the XRR patterns allowed for calculations of the thickness and the roughness of the films after fitting the data (see Figure 3.2.3). The calculations are in good agreement with the assumed thickness; typically calculated thicknesses were several angstrom smaller comparing to assumed ones. For example for the "B-Fe" film calculated thickness is smaller from the assumed one about 1.8Å, for "C-Fe" film the difference is equal to 4.1Å whereas in case of "A-Fe" about 9.9Å. This would suggest that the Eu and Fe atoms are mixing and form more

packed structures in such mixture, as is the case with other compounds of the RE-TM system. Calculated roughness has not been dependent on the as-grown structure; it is between 11.87Å for the "C-Fe" film and 30.47Å for the "D-Fe" film.

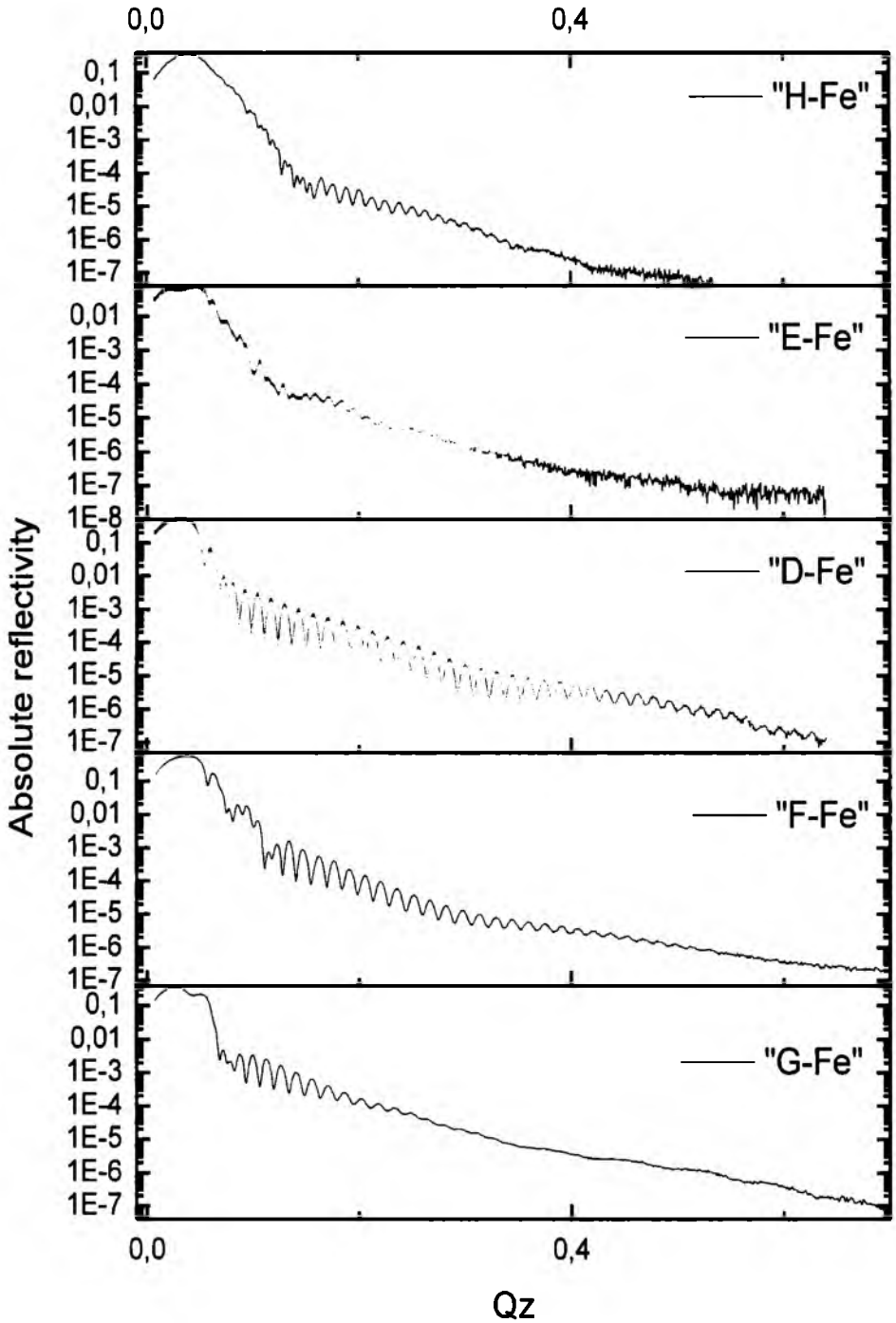

Figure 3.2.2 Specular reflectivity obtained for selected Eu-Fe films.

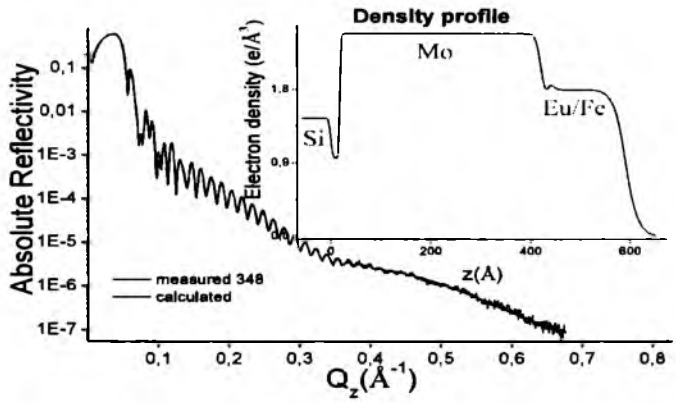

Figure 3.2.3 Electron density profile calculated from the specular reflectivity for the "C-Fe" film.

Taking into account that formation of compounds between rare earth and iron is more likely to occur (see Table 1) suspected formation of new phases has been verified through the XRD research. Polycrystalline arrangement of the crystallites on the surface of the films, specified via the RHEED measurements, was another point in favor of a good research direction which was to search for new Eu_xFe_y phases. Unfortunately, even if the europium and iron layers are mixed and form uniform 10 – 20 nm thick layer of well-established electron density, no atomically ordered intermetallic phase could be resolved basing on the diffraction results. The only apparent diffraction peaks come from the substrate or the protective coating, as can be seen in Figure 3.2.4

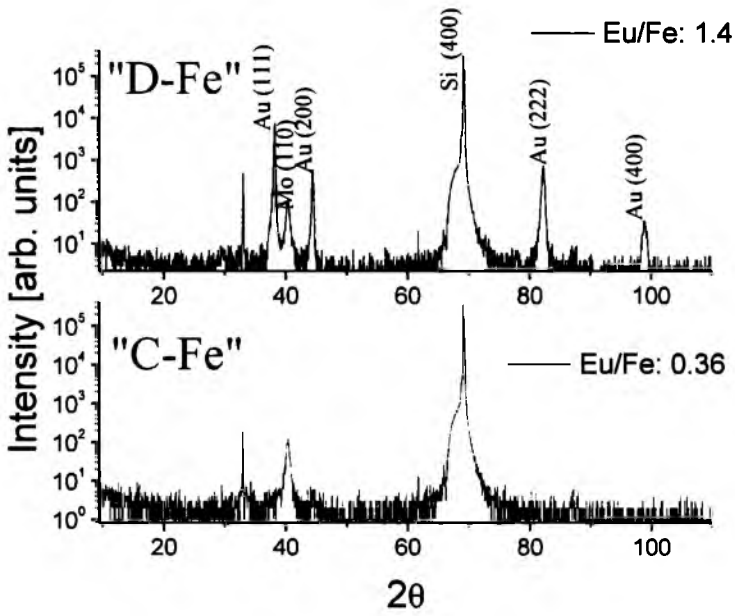

Figure 3.2.4 XDR patterns for selected "D-Fe" and "C-Fe" films.

3.2.2 Electronic Structure

In this section the reaction between Eu and Fe layers will be evaluated. Specifically, as in case of Eu-Mn system the Eu 3*d*, Eu 4*d* and Fe 2*p* core levels, and relative changes in their shapes and intensities will be analyzed. This chapter will provide some additional information about pure thin layer of iron and its oxide, which have been notified to explain the influence of the cover layer on the properties of examined films. Again particular attention, in case of performed XPS measurements, was paid to the changes of the valency of europium.

Typical for the Eu-Fe system XPS survey spectrum has been shown in the Figure 3.2.5; the analysis indicates that only the deposited elements are the components of the film, as in case of previously studied system no oxygen, carbon or other contamination is visible in the XPS survey spectra. Lack of lines originating from molybdenum buffer layer, in the XPS spectra, indicates that the Eu and Fe layers were grown in the layer-by-layer (Frank-van der Merwe) or layer-plus-island (Stranski-Krastanov) growth mode.

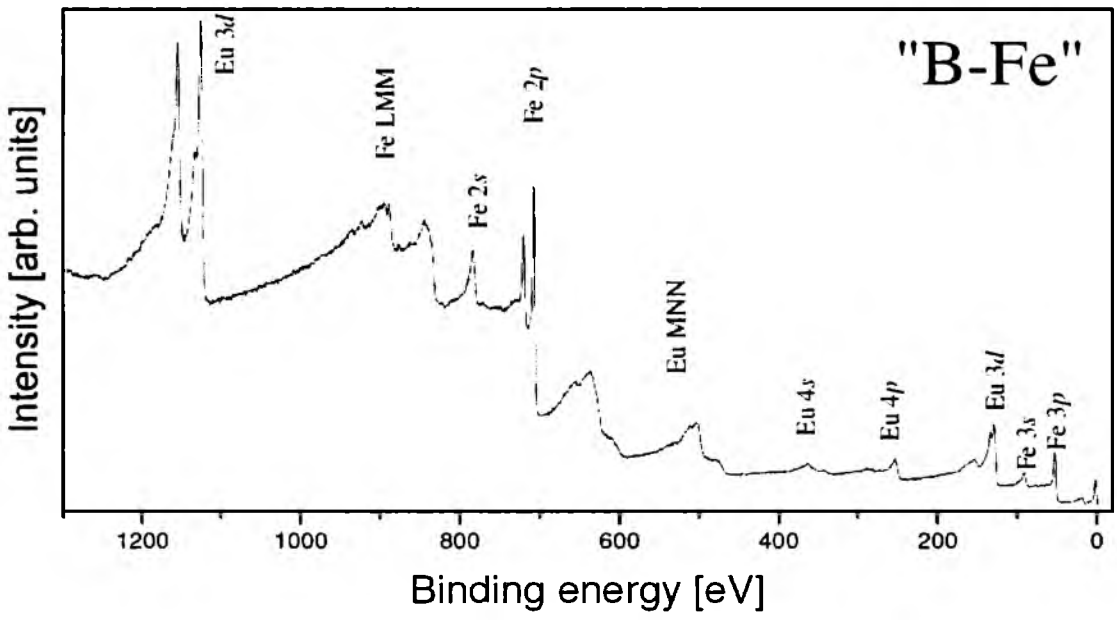

3.2.5 Survey spectrum for the "B-Fe" film after the deposition process.

The photoemission spectra of core levels were systematically taken after the deposition of Eu-Fe multilayers and later during the annealing process. For all examined films in the Eu-Fe system Eu and Fe layers after deposition exhibit typical metallic behavior which has been

confirmed by the analysis of the position and shape of both iron and europium photoemission lines. During or after annealing process the Fe 2*p* line shows small shifts up to 0.2 eV and slight change in its shape; this clearly indicate that iron, the top layer in the structure (see Appendix B), remains in metallic state but the co-ordination has changed. However, similarly as in case of Eu-Mn system, during annealing process changes of Eu multiplet are significant. For almost all examined films of the Eu-Fe system the valence transition from Eu^{2+} to Eu^{3+} was observed. In Figure 3.2.6 the Eu 3*d* and Eu 4*d* and Fe *2p* line have been plotted for representative of the Eu-Fe system samples: "B-Fe", "C-Fe".

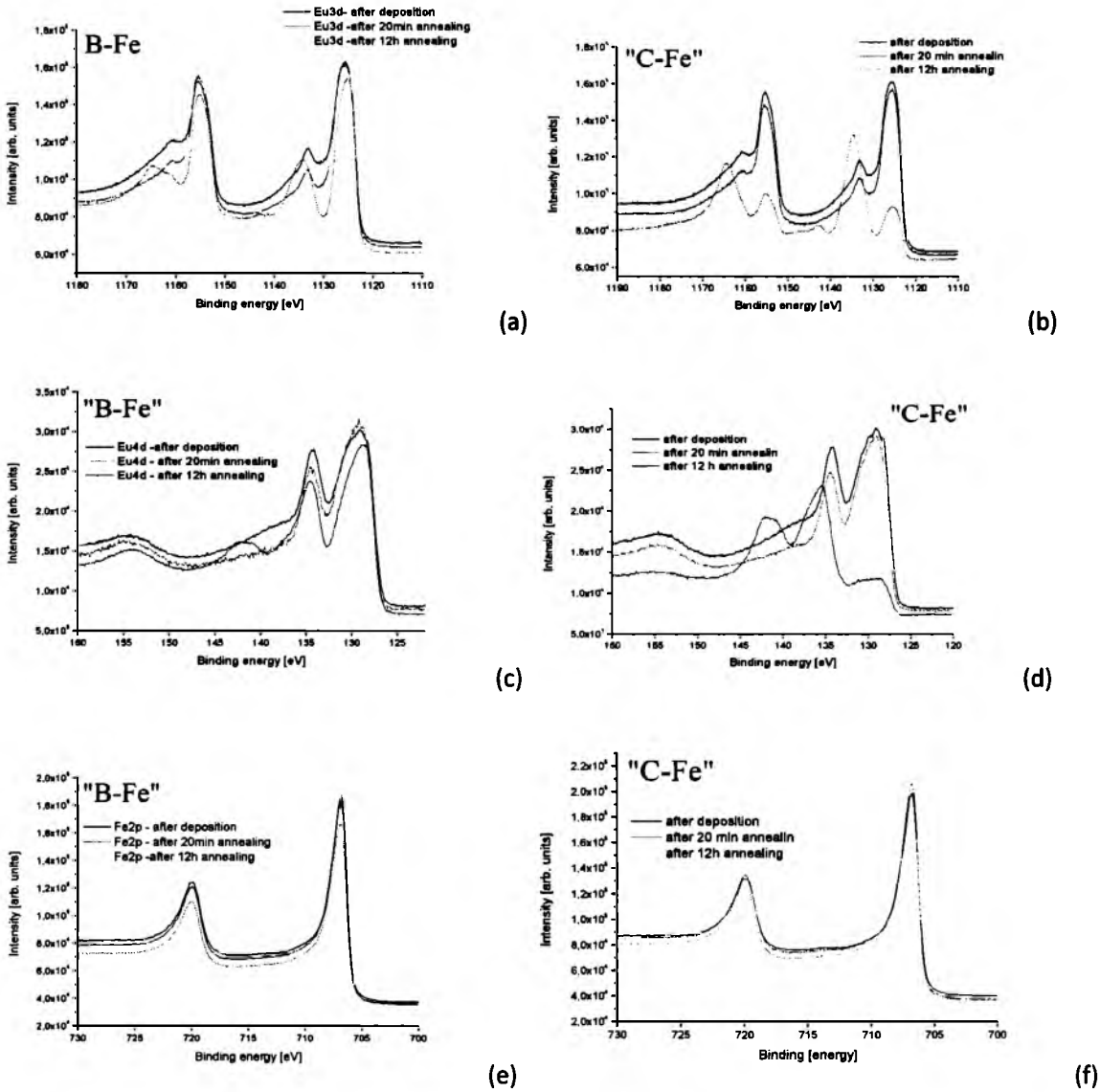

Figure 3.2.6 Eu *3d* (a, b), Eu *4d* (c, d) and Fe *2p* (e, f) core levels for "B-Fe" and "C-Fe" films. The temperatures of annealing have been summarized in Table 3.2.2.

The chemical shifts of core levels (Eu *3d* up to 8.9eV, Eu *4d* and Fe *2p* up to 0.1eV) and relative changes in Eu *4d*/Fe *2p* area ratio also monitored by the XPS indicate mixing between europium and iron. The process of the $Eu^{2+} \leftrightarrow Eu^{3+}$ valence transition was observed during the annealing for most examined concentrations, however for selected compositions the divalent europium was observed by the low intensity contribution to the *3d* and *4d* spectra as it has been shown in Figure 3.2.6.

Valance transitions due to ad-deposition

Valance transitions of europium due to the deposition of additional layer of either Fe layer or layer of protective coating have been observed in the Eu-Fe system similarly to the Eu-Mn system. After annealing process of the "C-Fe" film the film has been covered by a protective layer of 20Å thick layer of gold. Noticeable difference in the Eu^{3+} and Eu^{2+} states has been observed in the XPS Eu *3d* spectra as it has been presented in Figure 3.2.7.

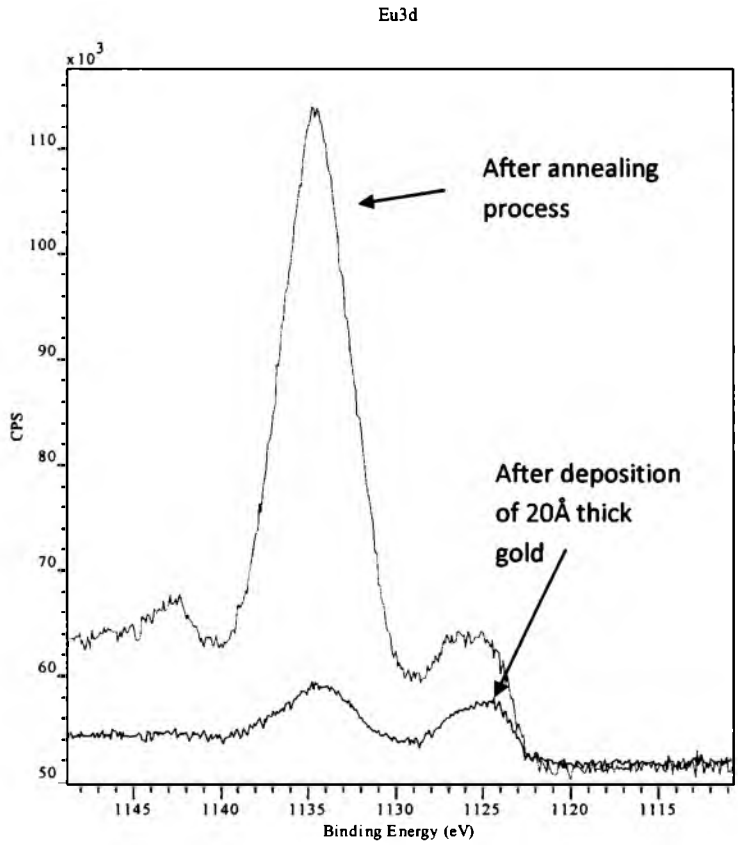

Figure 3.2.7 Changes in the Eu *3d* line after deposition of additional layer of gold on "C-Fe" film.

The relative intensity ratio of Eu^{2+} and Eu^{3+} has significantly changed as a consequence of the deposition of gold layer on the top of the film where europium was primarily in 3+ valency state. To verify that phenomenon additional test has been performed. The 1nm thick iron layer, film "J-Fe" grown in the same conditions as other films, has been oxidized in controlled way; the pure iron layer was annealed up to 230°C and for 10min oxidized in the 10^{-7} Torr O_2 atmosphere.

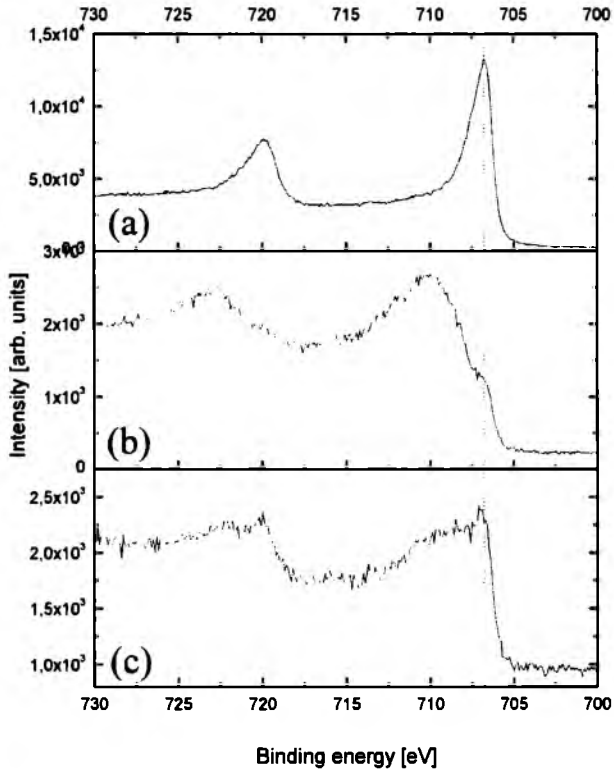

Figure 3.2.8 The Fe 2*p* photoemission lines obtained in the XPS measurements (a) after deposition, (b) after oxidation, (c) after deposition of 20 Å thick layer of Mo.

The Fe2*p* line obtained in the XPS measurements indicate that after the deposition process the iron was in pure metallic state (see Figure 3.2.8 (a)). After oxidation (see Figure 3.2.8 (b)) the metallic iron was still visible but the contribution from the oxide was the largest. In the next step (c) the film was covered by 20 Å thick molybdenum layer, after that process the XPS measurements has been collected and it showed up that the metallic state of iron appeared. Similarly as in case of effect presented in Figure 2.3.7 the relative ratio of two different chemical states is changed due to ad-deposition, this would suggest that the changes are due to changes in the interface of the layers. The influence of ad-layer on the properties of thin

films has been observed in various different researches [93-96]. However, in works to which I refer; the object of interest was the impact of ad-deposition on magnetic properties of the films. According to these research certain changes in the anisotropy of the film due to the ad-deposition of Mo or V layer have been detected in Au/Co/Mo [93] it has been also reported for other thin film systems: Fe/Au layers [94], Co/(Au, Cu) [95], Fe_3O_4/Au [96].

3.2.3 Magnetic and transport properties

For presented in this chapter results obtained in the SQUID measurements the diamagnetic contribution of the films substrate has been, as in case of Eu-Mn system, subtracted for both temperature (M-T) and field (M-H) dependence of magnetic moment.

Temperature-dependent SQUID measurements were performed in both zero-field cooled and field-cooled modes for different applied fields (10, 50, 100Oe), as in case of Eu-Mn system. Temperature measurements were accompanied by the field dependent measurements of magnetic moment performed at 2, 15, 40 and 120 K.

Typical for the Eu-Fe system M-T dependence is different in nature than the one observed for the Eu-Mn system. Here the magnetic behavior is associated with the iron atoms. The value of the magnetic moment and its temperature dependence point to ferromagnetic order present for all films even at room temperature. Experimental results, M-T, are shown in Figure 3.2.9. Some characteristic features visible on the M-T curves (see Figure 3.2.9 (a, b, c, d)) help to understand the nature of Eu-Fe films.

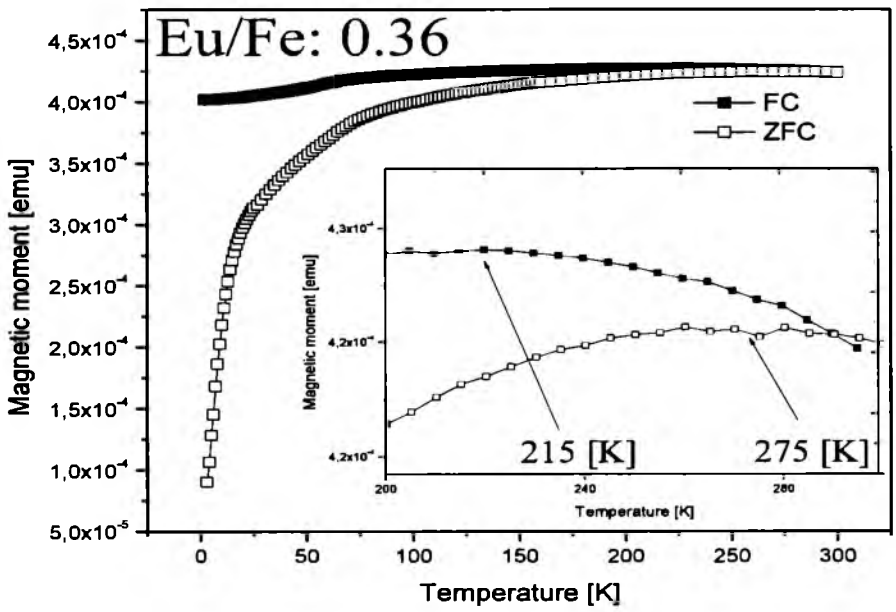

(a)

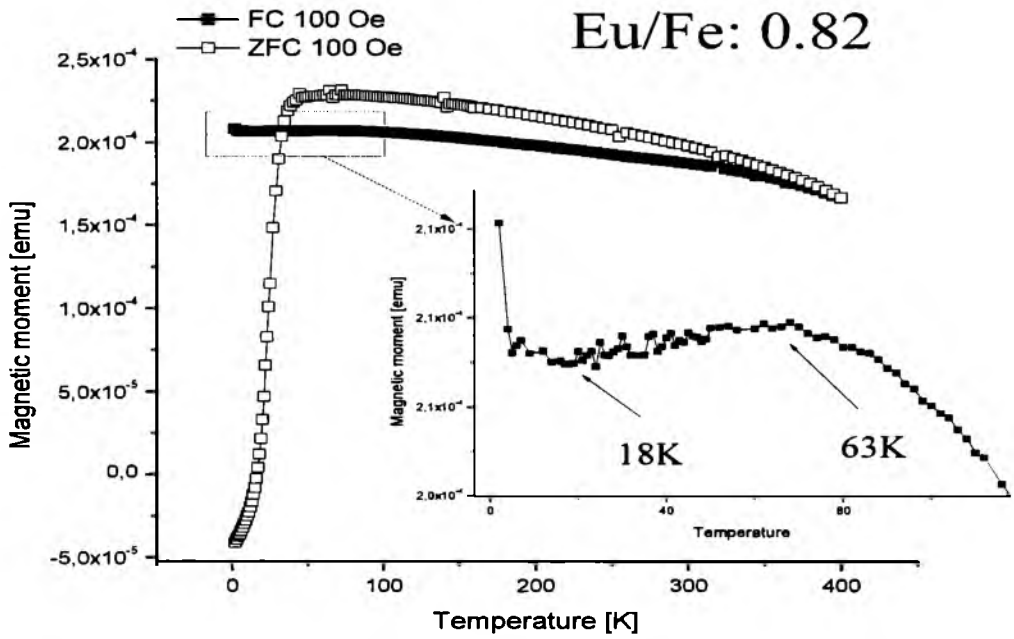
FC 100 Oe
ZFC 100 Oe
Eu/Fe: 0.82
Magnetic moment [emu]
Temperature [K]
18K
63K
Temperature

(b)

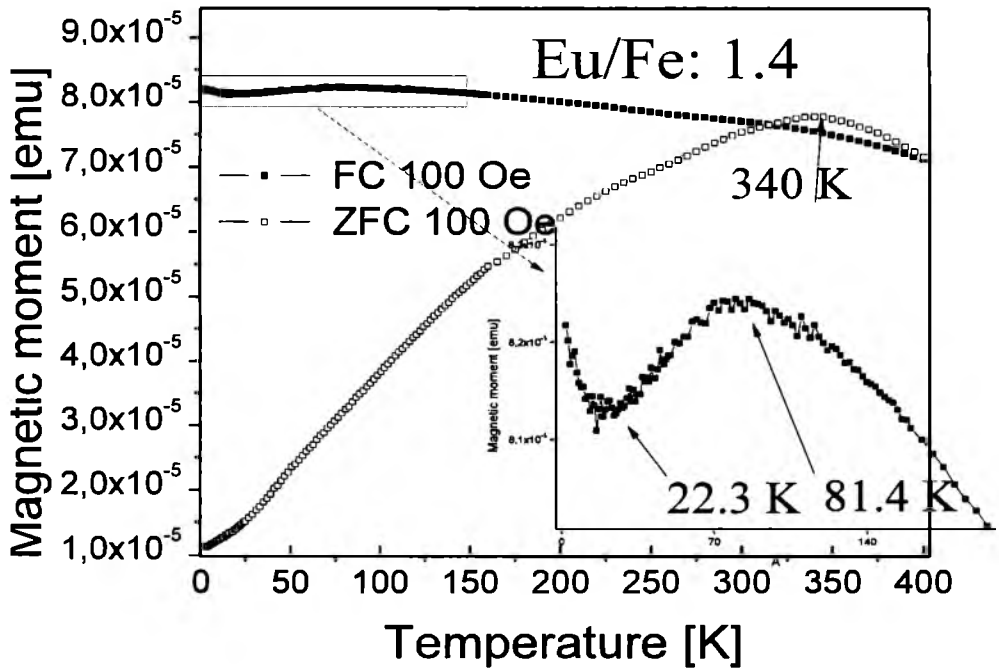
Eu/Fe: 1.4
FC 100 Oe
ZFC 100 Oe
340 K
22.3 K
81.4 K
Magnetic moment [emu]
Temperature [K]

(c)

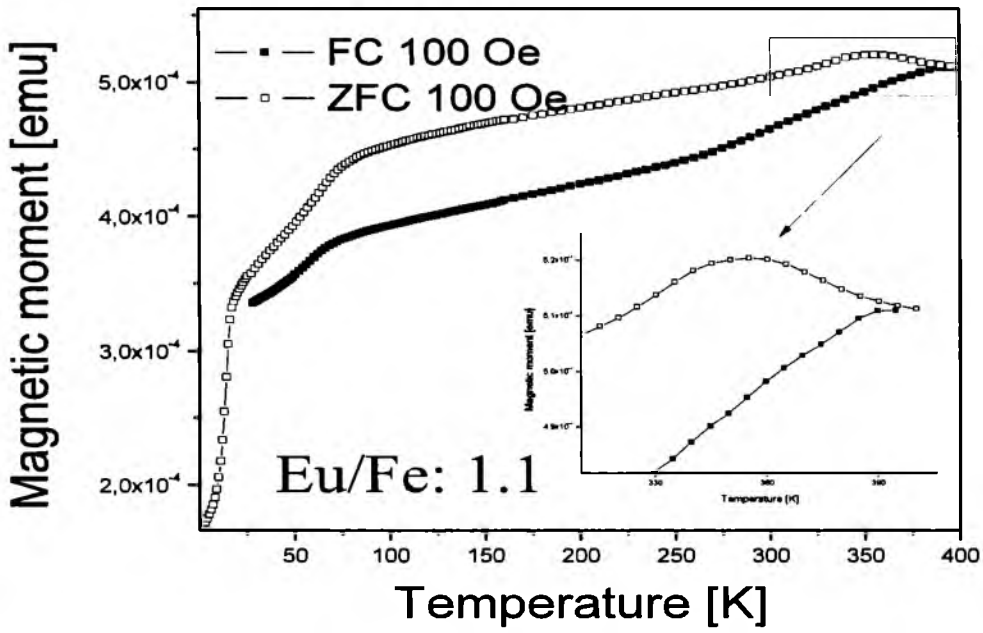

(d)

Figure 3.2.9 Temperature dependence of magnetic moment in FC and ZFC modes at 100 Oe presented for (a)"F-Fe", (b) "C-Fe", (c)"D-Fe", (d)"E-Fe" films.

The most important feature of the M-T curves is a strong thermomagnetic effect seen as irreversibility in the measurements of temperature dependence of magnetic moment in FC and ZFC branches. That feature was detected even if the temperature for which the measurements were stared (400 K) was below the Curie temperature of the ferromagnetic component. In order to detect that temperature selected samples were measured up to about 1000 K with the use of a PPMS magnetometer and it was found that T_c is at least 600 K. For higher temperatures the irreversible degradation of the films was observed.

Presented M-T curves show thermomagnetic effects in the entire temperature range (2K-400K) for which the measurements have been performed. Observed for all examined films irreversibility is demonstrated as the splitting of M-T curves measured in FC and ZFC modes. The irreversibility can be understood due to the fact of slowing of the spin relaxation times which is caused by the anisotropy (of the coercivity) in ferromagnetic particles. For the M-T curves obtained in measurements performed in zero-field-cooled mode, the magnetic moment increases more rapidly than for those performed in field-cooled mode. Such splitting resembles behavior of a magnetic particle system [97]. It is characteristic for typical of the

blocking process for an assembly of superparamagnetic nanoparticles but it can be also linked to the spin glass materials [97 - 99]. Frustration in the magnetic ordering can also lead for similar thermomagnetic effects.

Besides the irreversibility there are number of additional important features manifested in the M-T curves in both modes. Characteristic feature, which can be seen in M-T curves obtained in zero-field-cooled mode, is a presence of a broad maximum. The maximum has been observed for all measured films, for the applied field of 100Oe it occurs near room temperature with the exception of the film where Eu/Fe ratio is 0.82 where the maximum appeared below 90K. For the film where Eu/Fe ratio is equal 1.4 at 340K, 356K for the co-deposited film with the 1.1 Eu/Fe ratio and finally 275K for the films with Eu/Fe ratio equal 0.36. The maximum in M-T curves measured in the ZFC mode can be related to superparamagnetic unblocking process of the single/domain particles. Most likely the particles become superparamagnetic at temperatures above that observed maximum. Thus the maximum is related to the average blocking temperature of the particles. Nevertheless, looking more closely at accompanying M-T curve measured in FC mode some extra features allow to qualify two of the films as spin glass or super spin glass like materials. Those two films: with the Eu/Fe ratio 0.82 and 1.4 have the characteristic feature, minimum in the M-T curves in FC mode at 18K and 22.3 respectively, which can be only observed in the spin glass and super spin glass systems [97, 98].

Another important feature is an unusual and rarely observed effect of the value of the magnetic moment measured in ZFC mode exceeding that found in the FC mode. Such effect has been observed for three samples (see Figure 3.2.9 a, c, d) however it occurred for those films in a different temperature range. For the film with Eu/Fe ratio 1.4 the temperature range was about 75K wide, for the one with Eu/Fe ratio 0.82 about 370K and for the co-deposited film where the Eu/Fe ratio was equal 1.1 the widest temperature range of about 400K was observed. Analysis of the literature data shows the unusual effect where M-T in FC mode stays below M-T in ZFC mode only in very limited number of materials - in amorphous flash-evaporated Pd-doped NiMn thin films [100] and amorphous carbon [101]. The explanation of this effect was proposed by the Y. Öner *et. all* in reference [100]. Proposed by this group explanation was based on the model of Imry and Ma [102]. According to this model if the coexistence of a classical ferromagnet together with some additional antiferromagnetic regions/areas is assumed the following behavior can be expected. Appearance of a random component of the field due to presence of antiferromagnetic regions

causes coupling to the host ferromagnetic alignment as a result the system can be forced to break into domains antiferromagnetically coupled to each other. Decrease in the average moment per atom may occur due to the long-range ferromagnetic ordering together with the antiparallel alignment of some spins at antiferromagnetic regions/areas. In such circumstance, for the measurements performed in the FC mode, the extent of the antiferromagnetic alignment along the applied field should be larger than for the measurements performed in ZFC mode. Consequently the magnetic moment measured in the FC mode may possess in some temperature range lower values than in case of ZFC mode.

With regard to presented in Figure 3.2.9 results described the above model could be introduced with the assumption that the role of classical ferromagnetic phase plays an amorphous layer of pure iron or mixture of iron and europium with some specified Eu/Fe ratio whereas the antiferromagnetic regions would consisted of mixture of iron and europium or pure europium respectively. As the XRR results show no separated Fe film the ferromagnetic phase should be rather attributed to small, probably amorphous, Fe nanoparticles.

The last option would be the presence of two Eu-Fe phases; the host ferromagnetic phase consisted of Eu-Fe mixture together with an additional Eu-Fe phase ordered antiferromagnetically. On the basis of presented in this thesis results it is difficult to choose which of these options is correct. Nevertheless considering the as-grown structure of the multilayered films ("D-Fe", "C-Fe") the effect occurs in the wider temperature range for the "F-Fe" film where thickness of individual Eu layer was about 6.5 Å whereas for the "D-Fe" film the Eu layer was about 19.5 Å thick with the iron thickness fixed at about 5 Å for both films. For the co-deposited film where both Eu and Fe were grown at the same time the effect is the greatest. It is an additional indication that the antiferromagnetic phase should be rather uniformly distributed in the film.

The field dependent study of temperature dependence of magnetic moment was also performed. The figure 3.2.10 presents the M-T curves in FC and ZFC modes for co-deposited sample "E-Fe" (b) and for the sample grown by a deposition of multilayers of Eu and Fe "F-Fe" (a).

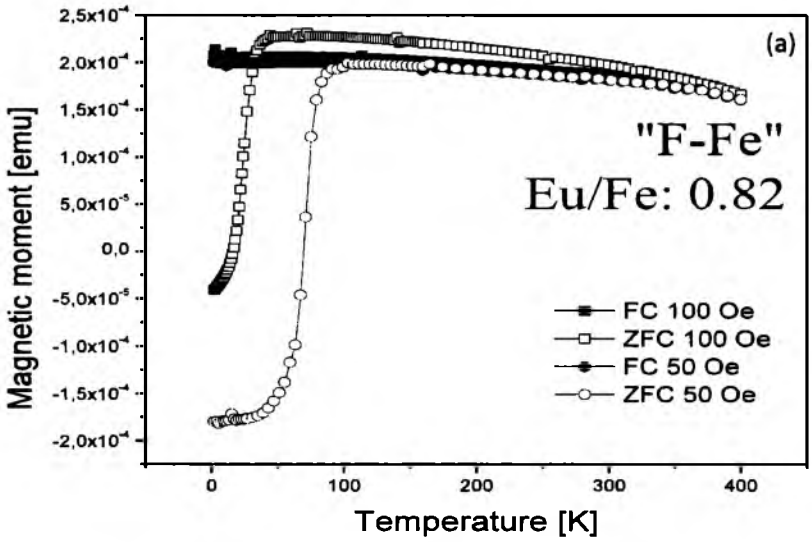

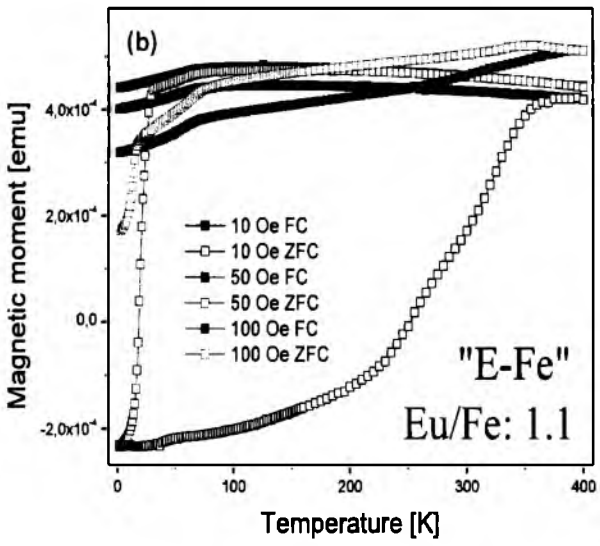

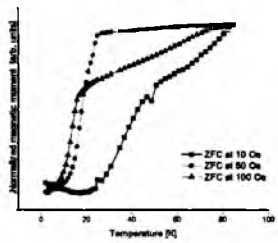

Figure 3.2.10 Field dependent measurements of temperature dependence of magnetic moment for (a) "F-Fe" and (b) "E-Fe" films.

The field dependent measurements of magnetic moment measured as a function of temperature was performed in both FC and ZFC modes for the "F-Fe" film with the applied field of 50 and 100 Oe, whereas for the co-deposited film for the 10, 50 and 100 Oe. The pronounced bifurcation of the FC and ZFC branches in the M-T curves is still visible with some different for the "E-Fe" and "F-Fe" films changes.

It can be seen in the M-T curves measured in ZFC mode for the "F-Fe" film that the blocking temperature decreases by about 47K as the field increase from 50 to 100 Oe. This essentially means that for higher applied field the effective barriers necessary to reorientation of the spins are lowered. Additionally the measurements performed in the applied field of 50 Oe in contrast to the one performed at 100 Oe does not allow to obtain the M-T curves measured in ZFC mode above the one measured in FC mode. This would suggest that 50 Oe external field is too low to see the impact of antiferromagnetically ordered regions. In such case when the temperature is higher than the peak temperature, ZFC and FC curves merge.

Changes observed in the M-T curves obtained for different applied fields have slightly different character for the "C-Fe" film prepared in co-deposition process. For this film similarly as for "F-Fe" film the M-T curves measured in ZFC mode are above the one measured in FC mode only at measurements performed at 100 Oe. But the shape of both FC and ZFC curves changes significantly when applying different fields. Merging FC and ZFC branches of the M-T curves above 150 K is well visible for the measurements performed in 50 Oe applied field. Characteristic drops below 100 K in FC branch of M-T curve was observed for all applied fields but unlike the measurements performed at 100 Oe for the applied field of 10 and 50 Oe it is preceded by the presence of a broad maximum at around 120 K. Observed in low temperature region transition in ZFC branch of M-T curve is field dependent; the temperature of the transition increases with decreasing field (see Figure 3.2.10 (b inset)). The observed field dependence of the peak in M-T curves in a ZFC mode as well as rather weak changes in temperature dependence of FC magnetization indicate a cluster spin glass like behavior, with some strong interactions between the particles [103, 104].

Different field dependence results probably from the structural difference such as the particle size.

In order to determine whether the magnetic moment of the films depends on other parameters the field dependence of magnetic moment (M-H hysteresis loops) as well as the M-T measurements have been performed in two different orientation of the sample and applied field; when the surface of the sample was parallel to the applied field (in plane) and when it was perpendicular (out of plane). For both types of measurements (see Figure 3.2.11 for M-T curves and 3.2.12 for M-H curves) a strong influence of the relative "film – applied field" setting have been observed.

Figure 3.2.11 (a) presents the FC branch of M-T curve, the inset represents M-T curves in both geometries at one scale, however to allow easy observation of the nature of the curves they are summarized on the graph with double y scale. For the M-T curve measured in the FC mode, the magnetic moment increases rapidly and attains a greater value for the field applied parallel to the film surface. In case of the measurements performed for the field applied perpendicular to the film surface the temperature dependence of magnetic moment exhibit completely different behavior; here both minimum at 9 K and broad maximum at around 120 K can be observed.

The differences can be observed also for the M-T measurements performed in the ZFC mode (see Figure 3.2.11). Particularly noteworthy are the results obtained for the out of plane measurements, where the region close to the room temperature region exhibits the strongest changes.

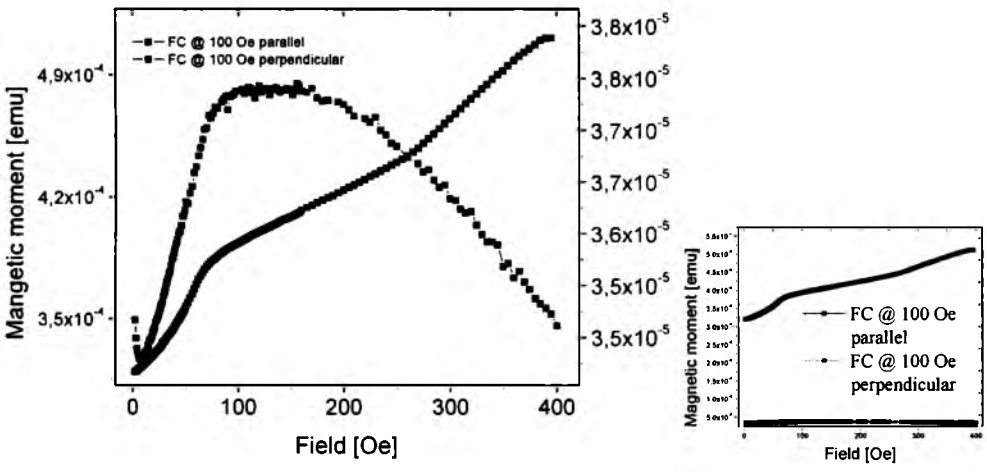

(a)

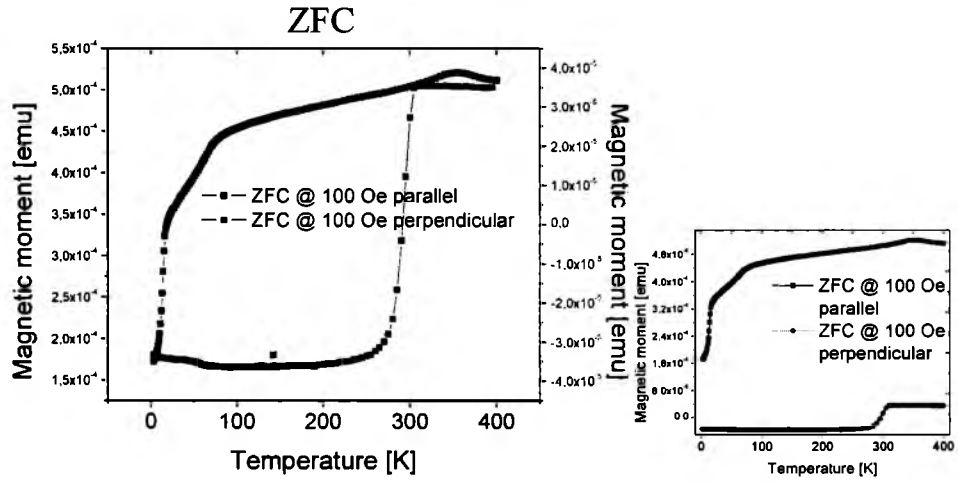

(b)

Figure 3.2.11 Temperature dependence of magnetic moment measured with the field applied parallel and perpendicular to the surface of the "E-Fe" film (a) in FC mode, (b) in ZFC mode.

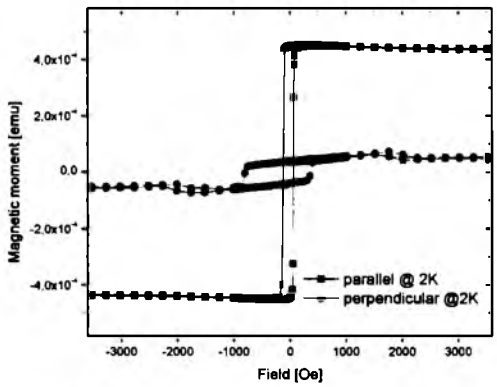

Figure 3.2.12 Hysteresis loops obtained at 2K with the field applied parallel and perpendicular to the film surface for the "E-Fe" film.

The alignment of the film parallel or perpendicular to the applied field is strongly imprinted in the M-H curves as presented in Figure 3.2.12. The M-H measurements have been performed at 2K in a wide field range. It can be seen that applying field perpendicular to the film surface causes significant increase of the coercive field as well as relatively large exchange bias effect (shift of the hysteresis loop) - the last one will be discussed below. The results imply that the easy magnetization axis in the plane of the film as it has been observed for the many materials in the thin film form.

To conclude the strong magnetic out of plane anisotropy has been established on the basis of FC and ZFC branches of M-T curves and M-H hysteresis loops. The cause of the observed changes in results obtained for in plane and out of plane measurements is the dominant contribution of the shape anisotropy, which favors the arrangement of the vector magnetization in the plane of the film. Nevertheless, the contribution of other kinds of anisotropies that may exist in thin films, such as exchange bias anisotropy or the magnetocrystalline anisotropy cannot be omitted.

The last stage of the magnetic research was to investigate mentioned above field dependence of the magnetic moment. Several additional details about the magnetic properties of the Eu_xFe_y films can be obtained from the analysis of the M-H hysteresis loops (see Figure 3.2.13).

The shape of the hysteresis loops is rather rectangular, the coercive fields (see Table 3.2.3) are relatively low for the "C-Fe", "F-Fe", "E-Fe" (see Figure 3.2.13 (a), (b), (c) respectively), while relatively high for the "D-Fe" film (Figure3.2.13 (d)). For all examined films the hysteresis loops revealed a decreasing value of coercive field with increasing temperature as in case of Eu-Mn system although, oppositely to the Eu-Mn system, the changes of the saturation in the Eu-Fe films at the examined temperatures are rather minor.

Magnetization loops have highlighted the presence of exchange anisotropy in Eu-Fe films. The Exchange bias phenomenon has been observed in the M-H hysteresis loops for all examined stoichiometries and for both types of applied deposition modes: multilayer deposition and co-deposition process. The table 3.2.2 contains assigned offset value. This unexpected in uniform layer effect indicates formation, below 40 K, of antiferromagnetically ordered phase; this would also explain the irreversibility of M-T curves in FC and ZFC modes.

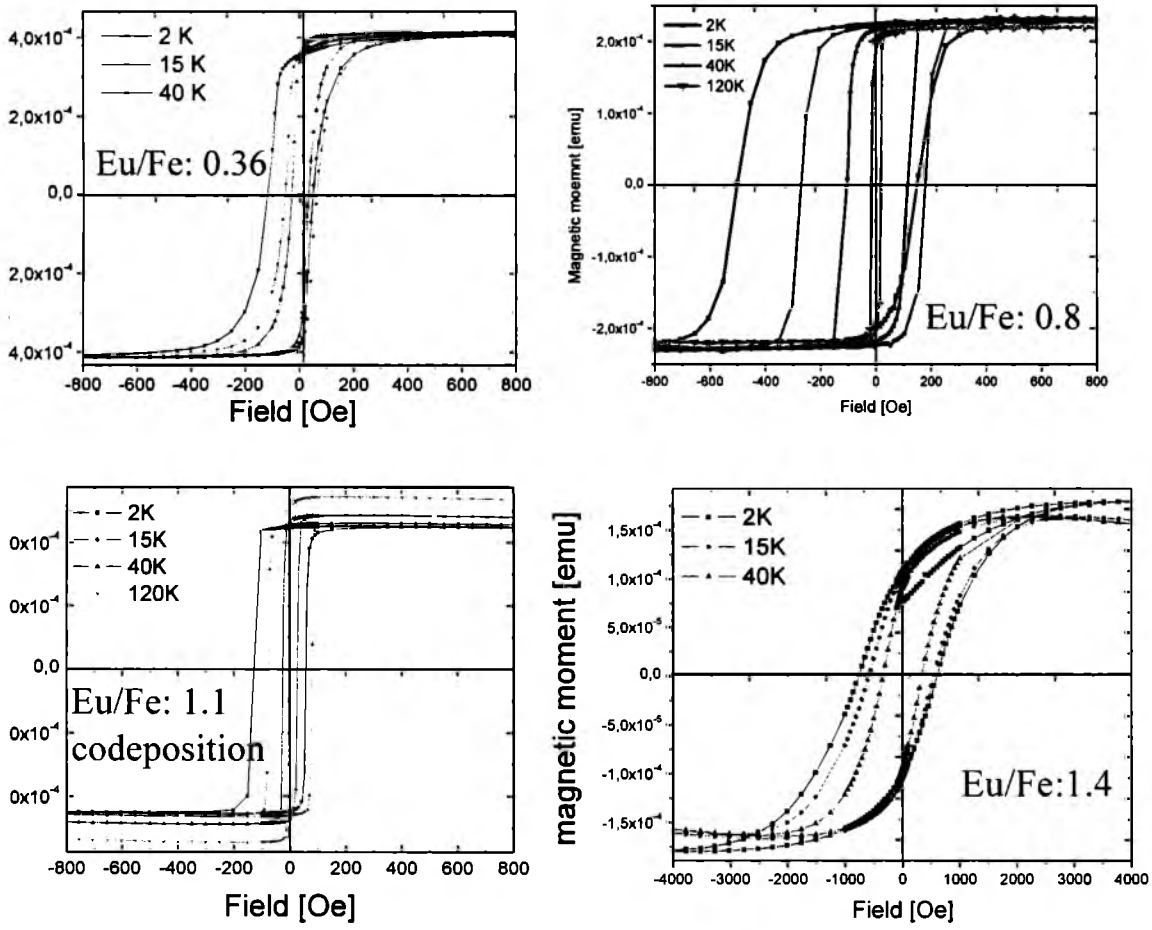

Figure 3.2.13 Hysteresis loops for the (a)"C-Fe", (b) "F-Fe", (c)"E-Fe", (d)"D-Fe" films.

The exchange bias phenomenon is typically observed in systems where both ferromagnetic and antiferromagnetic layers are present. Nevertheless similarly as in case of examined films there are some materials where such phenomenon has been observed with absence of two well defined layers. The effect has been observed in many different systems. For the bulk systems [105] the observed exchange bias behavior in $Ni_{50}Mn_{50-x}Sn_x$ has been assigned to the AFM-FM interfaces in the system which arises from coexistence of antiferromagnetic and ferromagnetic exchange interactions. In some heterostructures like the nanoparticle systems, Co/CoO [106] where partial oxidation of Co particles together with irregularity of interfaces between Co particles and CoO were found to be responsible for the observed exchange bias behaviour. The exchange bias has been even observed in oxygen-implanted Co thin films [106] where the implantation results in the formation of Co_xO_y embedded in a Co matrix. As a consequence exchange bias phenomenon was observed but the character of the AFM-FM interface is different than the one that would be observed in typical Co/CoO bilayer.

Table 3.2.3 Coercivity and the shifts of the hysteresis loops for "C-Fe", "E-Fe", "F-Fe" and "D-Fe" films.

Sample - thickness	at 2K			at 15K			at 40K		
	H_c^+ |Oe|	H_c^- |Oe|	Shift |Oe|	H_c^+ |Oe|	H_c^- |Oe|	Shift |Oe|	H_c^+ |Oe|	H_c^- |Oe|	Shift |Oe|
"C-Fe" - 16.12nm	48	-121.8	**-36.9**	62.8	-55.1	**3.9**	32.4	-30.7	**0.9**
"E-Fe" - 10nm	58	-127	**-34.8**	80.2	-77.4	**2.5**	26	-24.8	**1.1**
"F-Fe" - 11.45nm	150.9	-503.9	**-180.8**	178.7	-271.4	**-46.4**	110.7	-103.6	**3.6**
"D-Fe" - 14.75nm	2585.5	-3321.2	**-367.9**	2324.3	-2508	**-91.9**	1458	-1458	**0**

Table 3.2.3 summarizes the values of the coercivity retrieved from the hysteresis for all analyzed films. The H_c^+ is the value of coercivity on the right side of the loop, H_c^- on the left side, whereas the "shift" is the value of exchange bias field $H_E = (H_c^- + H_c^+)/2$. The common feature for all examined films is decreasing of value of the absolute shift ($|H_E|$). Moreover crossover from negative to positive exchange bias has been observed in the hysteresis loops for the "C-Fe" and "E-Fe" films for measurements performed at 15 and 40 K and for the film "F-Fe" at 40 K. The positive exchange bias was previously observed in typical exchange bias system Fe/FeF_2 [107], Fe/MnF_2 [108] where both ferromagnetic and antiferromagnetic layers are present. For those systems it was proposed that the interface of the antiferromagnetically

ordered layer aligns ferromagnetically with the external applied field and consequently ferromagnetically with the ferromagnetic layer. Such orientation of the spins on the interface of both ferromagnetic and antiferromagnetic layers is not preferable and in a consequence leads to shifts of the hysteresis loops along the field axis in the same direction as the applied magnetic field.

Anomalous behavior of temperature dependence of electrical resistivity was also observed in the Eu-Fe system. For two films with a different Eu/Fe ratio the maximum in the resistivity have been observed as it has been shown in Figure 3.2.14.

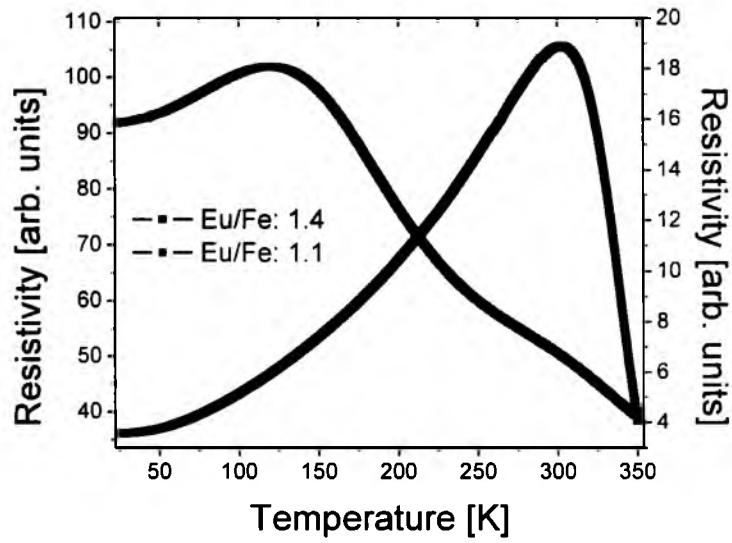

Figure 3.2.14 Temperature dependence of electrical resistivity measured for the "D-Fe" black line and "E-Fe" blue line.

Shape of the resistivity curve measured for the "D-Fe" film is similar to the R-T curves in the Eu-Mn system. The maximum in temperature dependence of resistivity of "D-Fe" film is observed at temperatures close to the room temperature, the maximum is followed by a sharp fall as it was found in the Eu-Mn system. A different R-T dependence was observed for the co-deposited film "E-Fe". The maximum is shifted here towards lower temperatures down to around 120K, but the decline in the value of resistance after the observed maximum is not as sharp as in case of "D-Fe" film. Similarly as in case of Eu-Mn system for the Eu-Fe system no clear association with the magnetic properties has been found.

3.2.4 Conclusions

The calculations based on the x-ray reflectivity measurements indicate intermixing of the layers and possible formation of Eu-Fe based alloys. The results obtained in the XRD measurements indicate a lack of formation of Eu-Fe compounds.

Relative changes of photoemission line intensity ratio Eu4d/Fe2p (Eu3d/Fe2p) as well as chemical shifts of core levels monitored by the XPS indicate mixing between europium and iron. The valance transition of europium from Eu^{2+} to Eu^{3+} was observed for most samples.
Temperature dependent SQUID measurements were performed in both zero-field and field-cooled modes with the filed applied parallel and perpendicular (presented only for one of the films) to the surface of the film.
A significant difference seen as irreversibility in the temperature dependence of magnetic moment in FC and ZFC modes measured for different applied fields (10, 50 and 100Oe) was observed. Additionally an increasing value of blocking temperature (maximum in ZFC curves) was observed with decreasing value of applied external field. The hysteresis loops show a decreasing value of coercive field with increasing temperature. Furthermore we presume that below 40K antiferromagnetically ordered phase is formed and consequently that the coupling between mixed Eu-Fe layers and the antiferromagnetically ordered phase causes below 40K typical for exchange bias phenomenon shifts of hysteresis loops. The coexistence of ferromagnetically and antiferromagnetically ordered phases and their interactions could be an explanation of the splitting of M-T curves measured in FC and ZFC modes. The coercive field has been found to be greater when applied field is perpendicular to the film surface (about one order of magnitude when comparing to the field applied parallel to sample surface).
Composition of the films seems to have a limited influence on the magnetic properties. All samples show a general tendency – ferromagnetic component related probably to Fe nanoparticles embedded in the antiferromagnetic matrix. The matrix may be composed from Eu-Fe compound/alloy where europium is mainly in non-magnetic trivalent state. Non-uniform distribution of ferromagnetic particles – probably also with respect to their size may lead to frustration of magnetic interaction at the interfaces and to exchange bias phenomena.

3.3 Eu – Cr system

Chromium is the last selected transition metal among the Eu-TM systems. It does not form stable bulk compounds with rare earths therefore; the study of Eu-Cr system seemed to be a good reference for the previous systems. Equally as in case of manganese and iron; the Eu_xCr_y have been grown in a wide x and y range.

The deposition was performed by thermal evaporation of elemental sources: Eu (99.99 %), Cr (99.99 %), and Mo (99.95%), Au (99.999 %). Deposition of europium, and gold was done with the use of standard effusion cells, while the chromium and molybdenum (used as a protective top layer) with the use of electron beam evaporator. Molybdenum has been grown from a 1.5mm thick wire, while the chromium from about 0.5mm size pellets. The films were grown only in the multilayer form, the co-deposition process due to design of both electron beam evaporator and the growth chamber couldn't be realized. Growth procedures, common for all systems, have been described in details in Chapter 2.1.2. As in previous systems, growth of Eu_xCr_y films performed by deposition multilayers of $(Eu/Cr)_x$ layers required a deposition of different thicknesses of individual Eu and Cr layers to achieve assumed concentration. Typical growth rates, optimally set for slow growth have been combined in Table 3.2.

Table 3.3 Growth rate for deposited materials.

Element	Growth rate [Å//s]
Europium	0.01-0.02
Chromium	0.03-0.05
Gold	0.02-0.04
Molybdenum	0.02

The thicknesses of analyzed films and their as-grown structure have been summarized in Appendix 6.2. Again, the total thickness and thickness of individual layers of grown films will be listed along with published results.

3.3.1 Crystallographic structure

Analogically to previously described systems structural characterization of the Eu_xCr_y system have been executed through three techniques: RHEED, XRR, XRD.

To determine the quality of grown films and their usefulness for further research the RHEED investigation have been performed *in situ*. In accordance with developed procedures the structural characterization of the surface of deposited films, via the RHEED measurements, was carried out firstly.

Structural changes in the deposited layers were observed after annealing, see Figure 3.3.1. To demonstrate this effect several representative samples have been selected (see Table 3.3.1 and for detailed information about the multilayer structure Appendix B).

Table 3.1.3 Description of representative samples

Sample name	Assumed concentration	Thickness [Å]
"A-Cr"	$EuCr_5$	36.3
"B-Cr"	Eu_2Cr_{17}	29.7
"C-Cr"	Eu_2Cr	90.9
"D-Cr"	EuCr	49.7
"E-Cr"	$EuCr_2$	45.4
"F-Cr"	EuCr	151.5
"G-Cr"	$EuCr_2$	121.2
"H-Cr"	Eu_2Cr	181

The RHEED images indicate that chromium and europium layers grown on poorly structured GaAs/Mo substrate exhibit two types of arrangement. In the first one, represented by films "A-Cr" and "B-Cr" the surface seems to be poorly structured, as the substrate– none of the typical for polycrystalline or monocrystalline features occurs; strongly diffused diffraction spots/or arcs suggest granular partly textured surface, similar behavior is presented when the roughness of the top layer is larger than the substrate. It is also possible that the RHEED image presents the beginning of alloying or crystallization of deposited elements. After annealing, the RHEED patterns changes; for the film "A-Cr" the surface of the film evolves to monocrystalline-like ordering whereas the surface of the film "B-Cr" changes into direction

of forming polycrystalline structure. The second type of arrangement visible as occurrence of set of rings indicates a polycrystalline structure of the surface of the films. The behavior of the surface during the annealing process is quite similar to the one observed in the Eu-Fe system. The ring structure is changed after the annealing process, which indicate changes in polycrystalline structure of the film (see film "C-Cr", "G-Cr") or the ring structure tends to blur which could suggest some kind of amorphization (see figure "D-Cr", "E-Cr", "F-Cr").

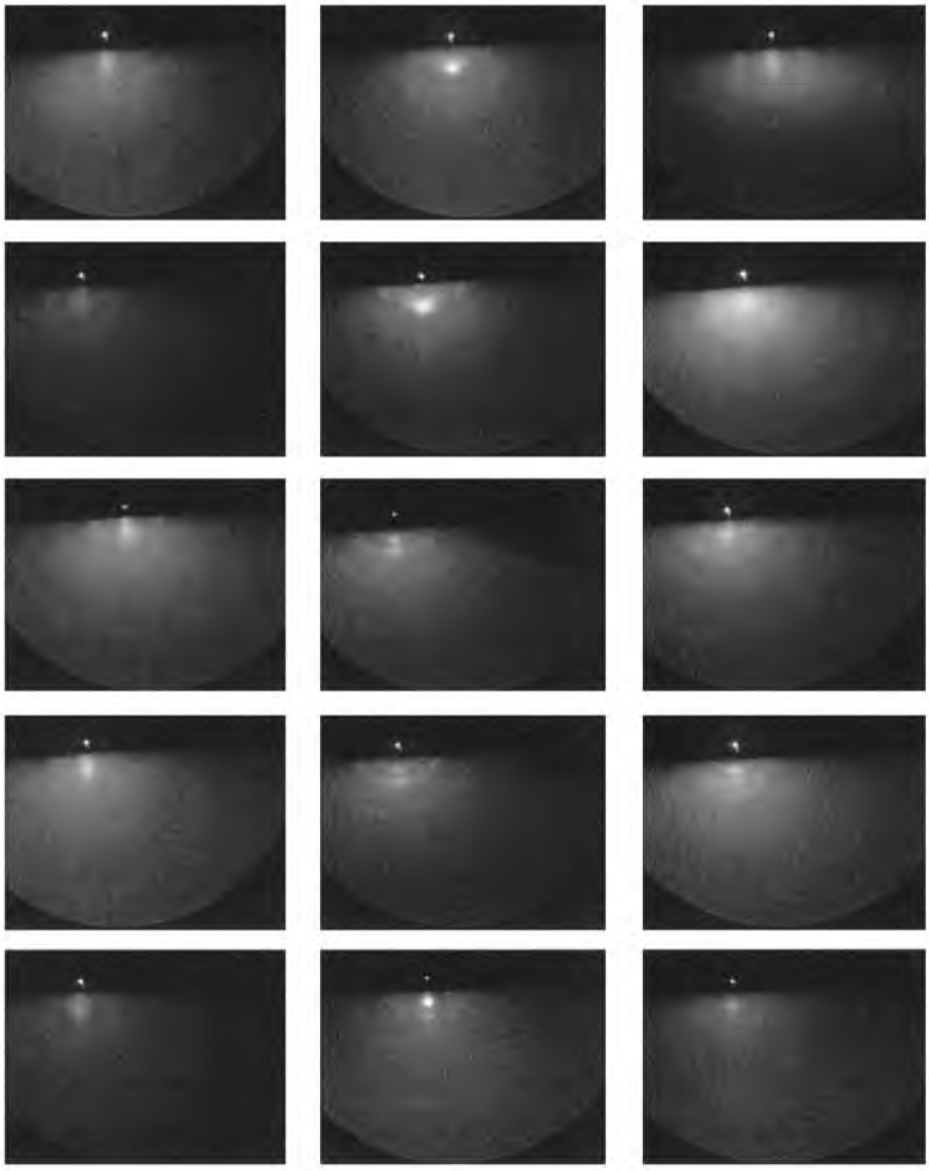

"A-Cr"

"B-Cr"

"C-Cr"

"D-Cr"

"E-Cr"

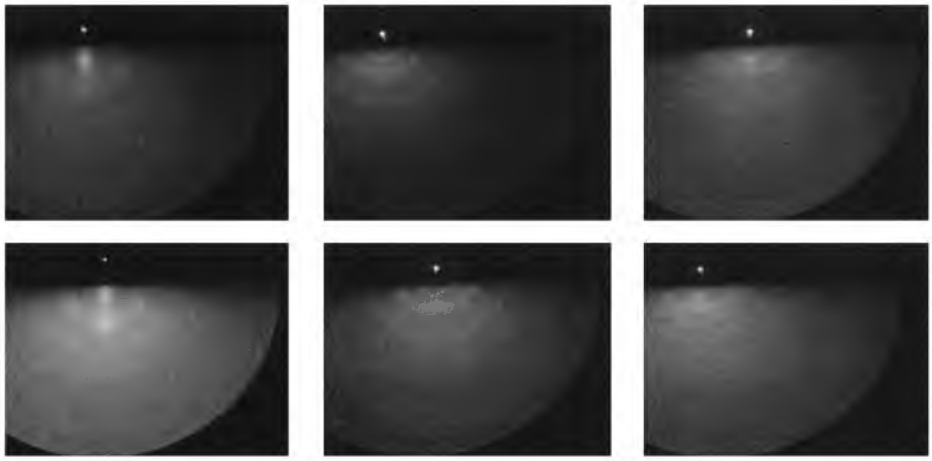

(a) GaAs/Mo (b) After deposition (c) After annealing

Figure 3.3.1(continued) RHEED patterns obtained for Eu-Cr (a) substrate, (b) as-grown, (c) after annealing.

Similarly as in case of Eu-TM system, where manganese or iron were the transition metal, further structural characterization included analysis of the XRR measurements; and later the presentation of the XRD patterns of the Eu_xCr_y system.

Basing on the results of XRR measurements, the electron density profiles have been initially calculated. In contrast to described earlier Eu-Mn and Eu-Fe systems the formation of homogeneous, in terms of electron density, layer in the Eu-Cr system is not observed for all tested films. As it can be seen in Figure 3.3.2, weakly developed specular reflectivity oscillation allowed to calculate the electron density of the film, but as the result (of quite good fitting) two different density profiles have been obtained. In the first one (a), one can find a 15nm thick homogenous layer of deposited elements, but in the second one the region where the film supposed to form a uniform layer the electron density is not constant. The second effect is probably caused by destruction of the protective cover and further reaction of deposited material with the environment.

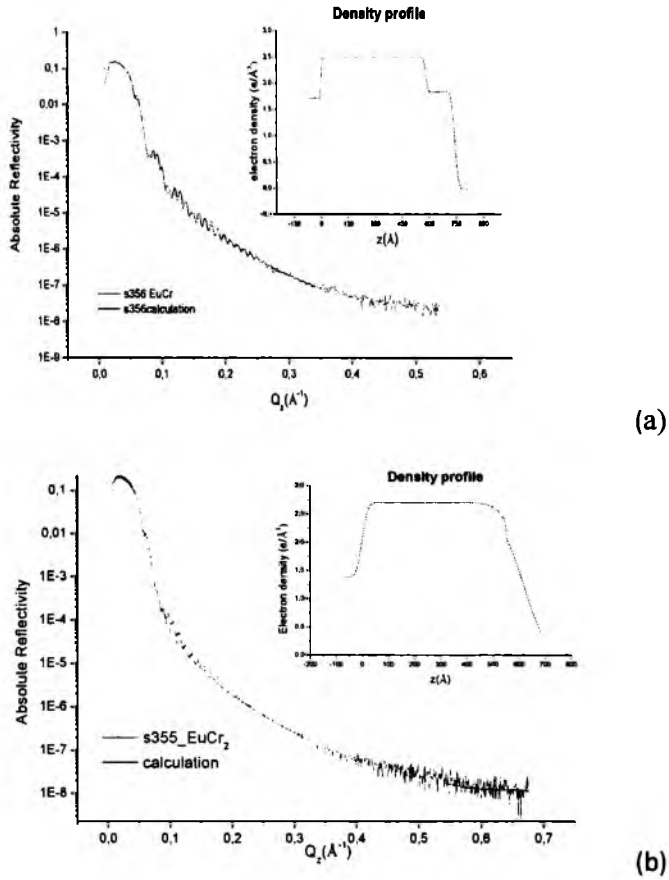

Figure 3.3.2 Specular reflectivity combined with electron density profile calculated from the specular reflectivity for selected film.

The XRD measurements have been the last step in the structural characterization of the Eu-Cr system. Similarly as in the Eu-Fe system no trace of any ordered phases is visible in the XRD patterns. Only the substrate and protective coating gives a rise to the diffraction pattern. Even for the film which has uniform distribution of europium and chromium (15nm thick) the atoms did not form any ordered phases. Nevertheless, although the stable bulk compounds between rare earths and chromium does not exist some reasons which justify the XRD research, like formation of metastable alloys in the thin film form in a wide range Gd_xCr_{1-x} can be found [92]. Unfortunately procedures applied by us to prepare the layers differ from the one presented in reference [92] but in the genre somehow it validate undertaken by us attempts for finding new phases.

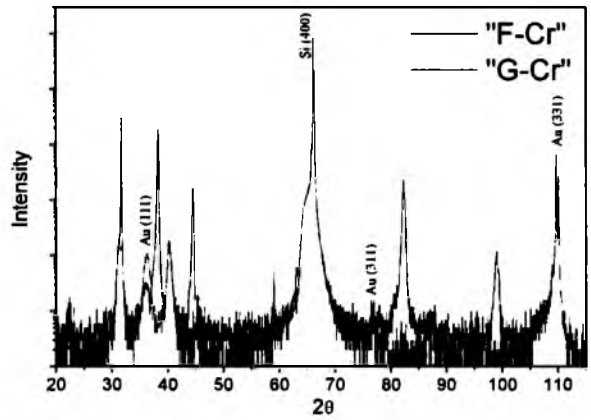

Figure 3.3.3 XDR patterns for "F-Cr" and "G-Cr" films.

3.3.2 Electronic structure, magnetic and transport properties

Typical for the Eu-Cr system XPS survey spectrum has been shown in the Figure 3.3.4; the analysis indicates that only the deposited elements are the components of the film, as in case of previously studied system no oxygen, carbon or other contamination is visible in the XPS survey spectra.

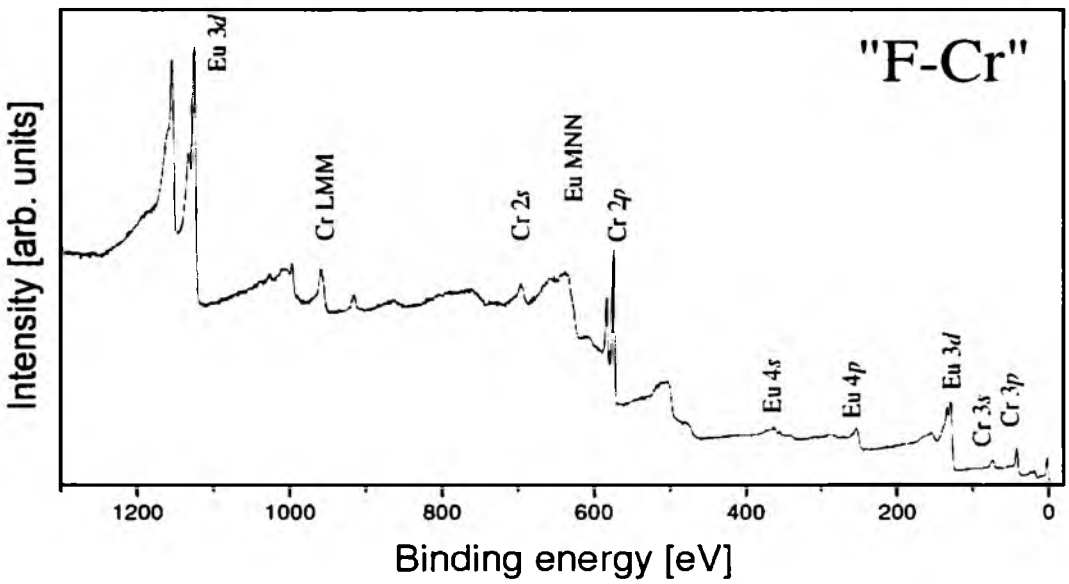

Figure 3.3.4 Survey spectrum for the "B-Cr" film after the deposition process.

The AFM measurements represented in Figure 3.3.5 indicate a formation of quite regular islands of about 100nm diameter.

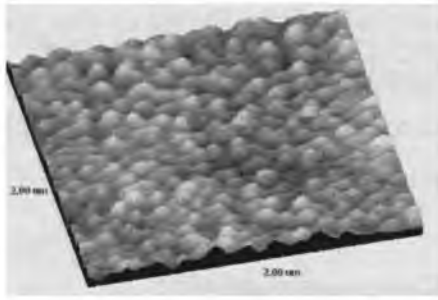

Figure 3.3.5 AFM image of "G-Cr" film covered by Mo/Au protective layer.

For almost all examined films of the Eu-Cr system the valence transition from Eu^{2+} to Eu^{3+} was observed. In Figure 3.3.6 the Eu 3*d* and Eu 4*d* line have been plotted for representative for the Eu-Cr system samples: "G-Cr" and "F-Cr".

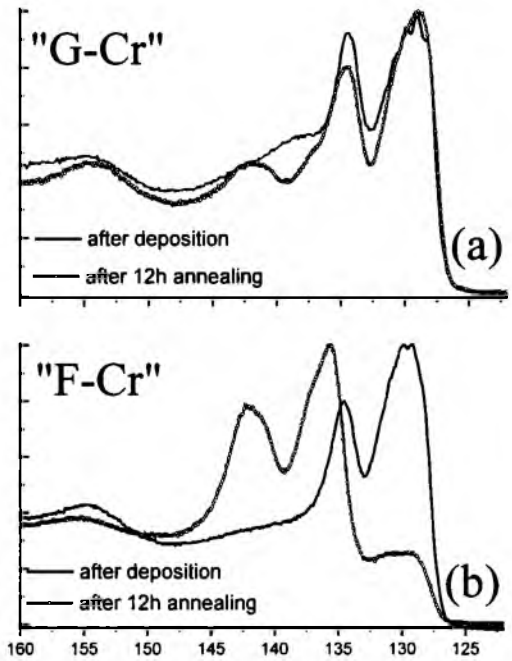

Figure 3.3.6 XPS spectra of the Eu 4*d* level obtained just after deposition of the (Eu–Cr)/Mo/Si film and after annealing at 480 K for 12 h. (a) Eu/Cr: 0.5. (b) Eu/Cr: 0.27.

For all examined films in the Eu-Cr system Eu and Cr layers after deposition exhibit typical metallic behavior which has been confirmed by the analysis of the position and shape of both chromium and europium photoemission lines. During or after annealing process the Cr 2*p* line shows small shifts up to 0.3 eV and slight change in its shape. Similarly as for Eu-Mn and Eu-Fe systems the chemical shifts of core levels and relative changes in Eu *4d*/Cr *2p* area ratio indicate mixing between europium and chromium.

Temperature-dependent SQUID measurements were performed in both zero-field cooled and field-cooled modes for applied field 100 Oe for two representative films. In one of them "G-Cr" europium was, according to the XPS measurements, divalent whereas in the second one "F-Cr" europium was in 3+ state.

Figure 3.3.7 shows the magnetic moment measurements of a film "G-Cr" with a Eu/Cr ratio of 0.5 (a) combined with the "F-Cr" film with the Eu/Cr ratio of 0.26 (b). The ZFC measurements indicate the existence of a transition at 50 K. There is some additional transition at 4K, seen as a clear change of behavior of magnetic moment in the ZFC mode. There is no sign of a europium oxide contribution to the measured moment. For this composition, europium is in the Eu^{2+} valency state (see Figure 3.3.6). Magnetic moment measurements of the "F-Cr" film with a Eu/Cr ratio of 0.29 show no sign of magnetically ordered phases. In this film, the europium was in the Eu^{3+} valency state (see Figure 3.3.6). Above the ferromagnetic transitions the temperature dependence of magnetic moment measured in ZFC mode retraces corresponding FC curves.

These results indicate that the magnetic behavior is associated with the divalency of Eu and that the behavior of $EuCr_2$ is an effect of frustration in the magnetic ordering. A similar effect was observed and discussed in Chapter 3.1.3 in the "G-Mn" ($EuMn_2$) sample.

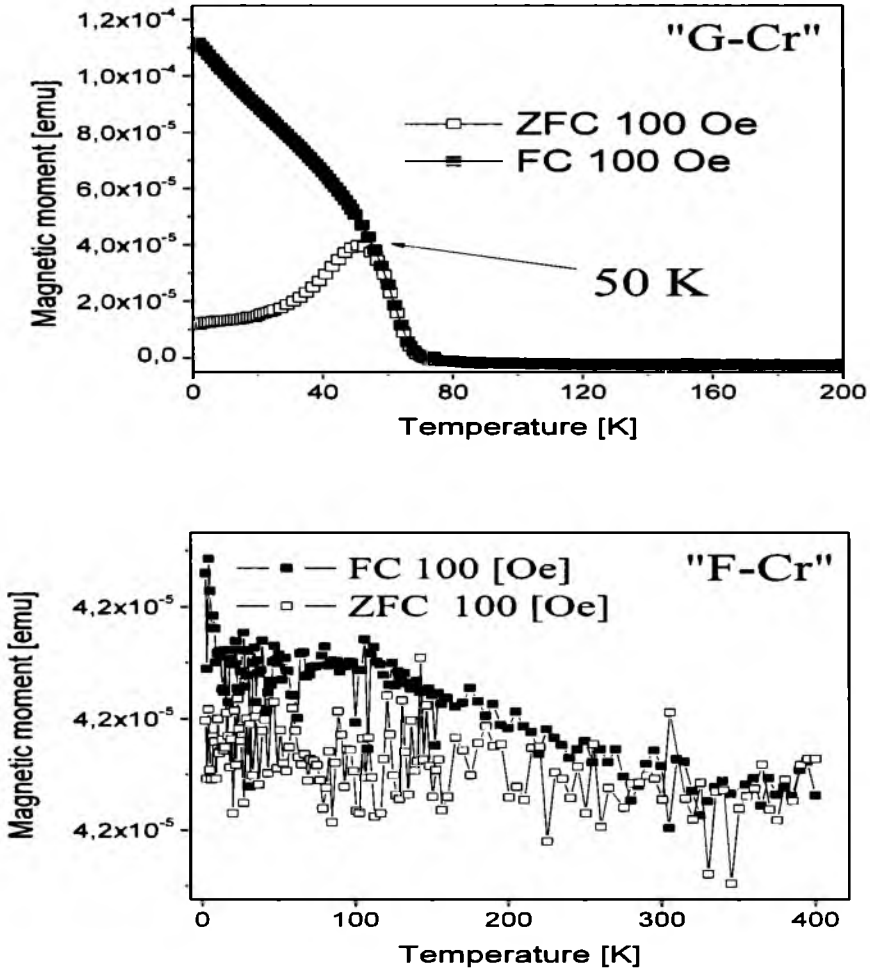

Figure 3.3.7 Temperature dependence of magnetic moment measured in FC and ZFC modes for (a) "G-Cr" and (b) "F-Cr" film.

Field dependence of magnetic moment measurements for the "G-Cr" film has been performed at 2 at 15 K; the results are presented in the Figure 3.3.5. The hysteresis loops revealed a decreasing value of coercive field with increasing temperature as it was in case of previously studied Eu-Fe and Eu-Mn systems.

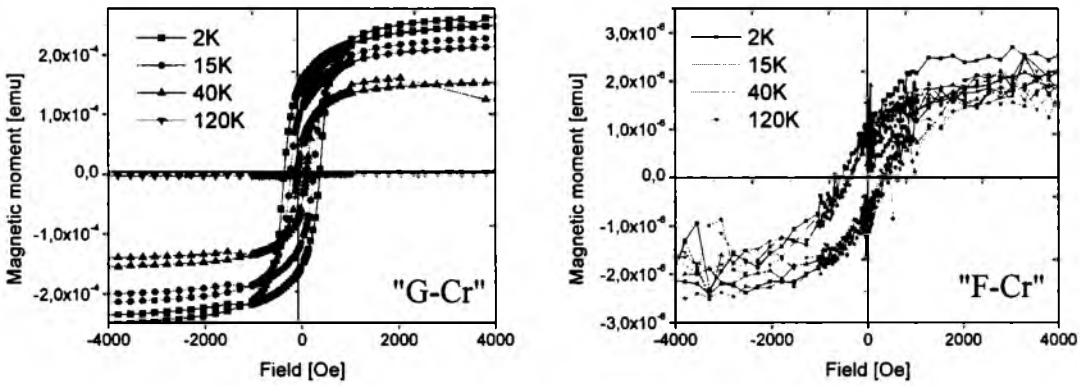

Figure 3.3.8 Hysteresis loops for the „G-Cr" and "F-Cr" films.

The anomaly in temperature dependence of electrical resistivity had been also observed for one of the films ("H-Cr") from the Eu-Cr system.

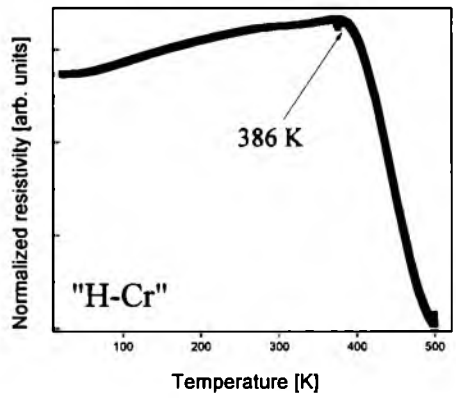

Figure 3.3.9 Temperature dependence of electrical resistivity of „H-Cr" film.

The shape of the R-T curve measured for the "H-Cr" film is slightly different than the R-T curves in the Eu-Mn system. The maximum in temperature dependence of resistivity of "H-Cr" film is observed at 386 K, it is followed by a fall but the fall is not as sharp as it was observed in the Eu-Mn system.

3.3.4 Conclusions

The calculations based on the x-ray reflectivity measurements indicate that intermixing of the layers and possible formation of Eu-Cr based alloys is realized only for selected films. The results obtained in the XRD measurements indicate a lack of formation of Eu-Cr compounds. Nevertheless relative changes of photoemission line intensity ratio Eu 4*d*/Cr 2*p* as well as chemical shifts of core levels monitored by the XPS indicate mixing between europium and chromium. The valance transition of europium from Eu^{2+} to Eu^{3+} was observed for most of the films with the exception of the film where Eu/Cr ratio was equal 0.5. Magnetic behavior of film selected films is associated with the divalency of europium, and similarly as in case of Eu-Mn system, the behavior for the film where europium is in divalent state ($EuCr_2$) is an effect of frustration in the magnetic ordering.

4. General remarks

4.1 Summary

The thesis contains pioneering research of the rare earth and transition metal intermetallic binary compounds, based on the studies of Eu-(Mn, Fe, Cr) films. An attempt was made to produce compounds which do not exist in the bulk form. For this purpose, modern techniques, for both the fabrication and the characterization of the materials, have been applied. To realize the idea of formation of materials with specified properties the Molecular Beam Epitaxy system was used for the material fabrication. Applied research techniques were designed to:

- track changes occurring during the process of forming the layers and later to monitor the changes of the properties of the films under specified conditions (the later included mainly temperature dependence of different factors),
- characterize the properties of fabricated films.

Because of the attempt to produce new compounds particular attention was paid to develop appropriate procedures for the preparation of the films. Described in Chapter 2 procedure was the final effect of many examinations. As a final point it showed up that two different modes of sample fabrication (multilayer deposition and co-deposition) were the best approach to get mixing of elements and finally new structures.

The structural characterization of the films have been performed with the use of diffraction techniques (RHEED, XRD) combined with the XRR technique often used in parallel to those two. Mixing of the layers, as a result of appropriate (heat) treatment, or layers stacking has been proven for all examined films. Formation of homogenous, in terms of electron density, uniform layer of mixture of Eu/Mn, Eu/Fe, Eu/Cr was observed for most of the used compositions. It has been demonstrated that formation of new atomically ordered phases can

be achieved in the Eu-Mn system. Three different phases were recognized for that system. All the phases contain close packed hexagonal planes. Observed lack of intermetallic phases for the Eu/Fe and Eu/Cr systems indicate to a rather amorphous character of those films.

Application of photoelectron spectroscopy, a surface sensitive technique, allowed carrying out studies in several different directions. The first one was aimed at monitoring the reaction of the film constituent elements. It turned out (analysis of chemical shifts and relative changes in the intensity ratio of the elements) that within the examined system the elements are intermixing at elevated temperatures, which were close to 200 C. The second one was directed to changes in the valence of europium. The changes associated to the reaction with surrounding transition metal lead to valence transition of europium $Eu^{2+} \leftrightarrow Eu^{3+}$. Europium may remain in a divalent state ($EuMn_2$, $EuCr_2$), may change the valency to trivalent (EuFe) or show intermediate valence state (Eu_2Mn_{17}). The third one was the observation of reversible valence transitions of europium which was found to be forced by heat treatment or change of the interface resulting from covering the surface of the film.

XPS data together with Atomic Force Microscopy measurements allowed recognizing surface topography exhibiting island formation for a part of samples.

Magnetic measurements performed in both zero-field cooled and field-cooled modes showed significant differences between the systems with various transition metals and modes of studies.

For one of the films - "E-Mn" ($EuMn_2$) ferromagnetic ordering was found which is related with a new phase and the presence of EuO. The ordering temperature of the new phase was determined as 15 K. Similarity of M(T) curves in Eu-Mn and Eu-Cr systems indicate that the magnetic behavior is associated there with the divalent Eu atoms. Separation in M-T curves measured in FC and ZFC modes, for those two systems, is an effect of frustration in the magnetic interaction. Changes observed in field dependent (measurements performed at 10, 50 and 100 Oe) FC and ZFC measurements of M(T) curves of the Eu-Mn system indicate presence of superparamagnetic regions which could be related to nm size islands found in AFM measurements. The hysteresis loops, revealed a decreasing value of coercive field with increasing temperature.

The magnetic properties of the Eu-Fe system differ from the previous two; here magnetic behavior is associated with the iron atoms or more likely with the aggregates of iron atoms. Ferromagnetic ordering is observed for all films even at room temperature. Temperature dependence of magnetic moment in FC and ZFC modes indicate that Eu-Fe films show a

blocking phenomenon and include superparamagnetic components. The M-T curves measured in FC mode indicate that several Eu_xFe_y films show behavior typical for the spin glass or super spin glass. We observed an unusual and rarely observed effect of magnetization exceeding in the ZFC mode that of the FC mode. Explanation of that effect is based on a model assuming the presence of antiferromagnetic areas accompanying the amorphous ferromagnetic film [100]. In the ZFC mode it may lead to higher magnetization with respect to the situation when cooling takes place in the substantial magnetic field. Moreover, exchange bias phenomenon has been observed in the hysteresis loops for the same group of samples. This effect is usually related to the interface between the ferromagnetically and antiferromagnetically coupled layers. As our samples exhibit a relatively uniform electron density, as derived from XRR data, one can expect that again the effect is related to the coexistence of ferromagnetic nanoparticles and antiferromagnetically coupled regions where divalent europium atoms are responsible for antiferromagnetic interactions. The films show a strong magnetic in-plane out-of-plane anisotropy as it was shown on the basis of measurements performed for the field applied perpendicular to the surface of the film.
The temperature dependence of electrical resistivity has shown for various samples a surprising result - the maximum at temperatures close to the room one. The hypothesis relating this effect to valence fluctuations of europium has to be confirmed by additional measurements.

4.2 Future work and applications

Research results presented in this thesis shows a number of interesting properties of the $Eu_x(Mn, Fe, Cr)_y$ films. Nevertheless there are still some open questions and therefore, additional studies could be continued. Further optimization of the growth parameters or other procedures is essential for complete explanation of the processes occurring in layers. In order to do so some supplement studies could be executed. Settlement of the existence of new compounds, with the use of other techniques, is here crucial. Other important steps in the research would be explanation of anomalous resistivity behavior, for this purpose, *in situ* resistivity measurements, performed during the growth and formation of new phases, are planned. It would be interesting to investigate magnetic properties of multilayer structures via Magnetooptical Kerr Effect (MOKE), or define magnetic structures of the films by

Conversion Electron Mössbauer Spectrometer (CEMS) or X-ray Magnetic Circular Dichroism (XMCD). In addition to experimental studies it would be worth to verify obtained results via some theoretical calculations. Starting for example, from the calculations, of occurrence of intermixing in multilayer structures based on Miedema model [109-111].

The application of Eu-TM layers into some devices could be realized from few points of view. The first one is due to properties of europium in which, as it was mentioned before, the valency is directly associated with its magnetic properties (pure spin magnetism or non-magnetic ground state). The possibility of switching between the non-magnetic trivalent and the magnetic divalent states would be remarkable for future spintronic devices. In presented in this thesis results such on/off switching was not observed, but for films where europium was trivalent excitation of the 2+ states was possible and caused only by increase of the temperature. Because of that, if for example some device would need inducing weak magnetic field increase of the temperature of the film by about 100°C should meet this requirement.

Already applied in some devices compounds and alloys from the RE-TM system shows where to find application for the films from the Eu-TM system. Therefore, additionally planned studies will determine and distinguish whether the samples can be applied for specified devices as: permanent magnets, as in case of $SmCo_5$ and $Sm(Co,Fe,Zr,Cu)_7$, magnetorestictive materials, which can transduce or convert magnetic energy to mechanical energy and vice versa, like in $REFe_2$, [112] hydrogen storage, huge absorption of hydrogen by $LaNi_5$, [113], materials for thermo-magnetic recording (TMR), like in TbFe, TbCo, GdTbFe, GdTbCo, [114], materials for thermo-magneto-optical recording (TMO), TbFeCo and GdTbFe [115] and many others.

The last one, in addition to all possible applications, which has to be highlighted, would be applying into certain devices the Eu-TM films exhibiting anomalous behavior (namely maximum in and the subsequent decrease of one order magnitude of the resistivity) in temperature dependence of electrical resistivity.

5. Bibliography

[1] P. Grünberg, R. Schreiber, Y. Pang, M. B. Brodsky and H. Sowers; Physical Review Letters 57, 2442–2445 (1986)

[2] J. S. Moodera, Lisa R. Kinder, Terrilyn M. Wong, and R. Meservey ; Physical Review Letters 74, 3273–3276 (1995)

[3] W. H. Meiklejohn and C. P. Bean; Physical Review 105, 904–913 (1957)

[4] Journal of Magnetism and Magnetic Materials Volume 192, Issue 2, 15 February 1999, 203-232

[5] A.E. Berkowitz, K. Takano; Journal of Magnetism and Magnetic Materials 200 (1999) 552-570

[6] Shufeng Zhang ; Physical Review B 45, 7487–7490 (1992)

[7] D Tripathy and A O Adeyeye, New Journal of Physics 13 (2011) 023035 (11pp)

[8] H. Nakamura, M. Moriwaki, M. Shiga, K. Inoue, T. Nakamura, A.V. Tsvyashchenko, L. Fomicheva; Journal of Magnetism and Magnetic Materials 150 (1995) LI37-LI42

[9] Motoyoshi Murakami, Journal of Applied Physics 101, 09C522 (2007)

[10] H Yamadat and M Shimizuz; J. Phys. F: Met. Phys. I7 (1987) 2249-2260.

[11] C. Djéga-Mariadassou · L. Bessais, Hyperfine Interact (2008) 182:113–123

[12] H. Nakamura , M. Moriwaki, M. Shiga, K. Inoue , y. Nakamura, A.V. Tsvyashchenko , L. Fomicheva; Journal of Magnetism and Magnetic Materials 150 (1995) LI37-LI42

[13] R. Sato Turtellia,_, J.P. Sinneckerb, R. Gro¨ ssingera, A. Penton-Madrigalc, E. Estevez-Ramsc, Journal of Magnetism and Magnetic Materials 316 (2007) e492–e495

[14] Hong Fu, Masud Mansuripur, Pierre Meystre; Physical Review Letters 66 no 8 (1991)

[15] Physics of the Solid State, Vol. 45, No. 5, 2003, pp. 927–931. Translated from Fizika Tverdogo Tela, Vol. 45, No. 5, 2003, pp. 883–887.

[16] F. Hellman, M. Messer, and E. N. Abarr), Journal of Applied Physics vol. 86,number 2 15 July 1999,

[17] Kirchmayr, H. R., Burzo, E.: 2.4.1.2 Phase diagrams. Crystal structure. Wijn, H.P.J. (ed.). SpringerMaterials - The Landolt-Börnstein Database

[18] H.R. KIRCHMAYR and C.A. POLDY; Journal of Magnetism and Magnetic Materials 8 (1978) l-42

[19] Landolt-Bornstein, Group IV Physical Chemistry - Phase Equilibria, Crystallographic and Thermodynamic Data of Binary Alloys, Volume 5

[20] Johansson B 1979 Phys. Reu. B 19 6615

[21] Wertheim G K and Crecelius G Physical Review Letters 40 813(1978)

[22] Allen J W, Johansson L I, Bauer R S, Lindau I and Hagstrom S B M 1978 Physical Review Letters 41 1499

[23] Laubschat C, Perscheid B and Schneider W-D 1983 Phys. Rev. B, Condens. Matter 28 4342

[24] Schneider W-D, Laubschat C, Nowik I and Kaindl G 1981 Physical Review B 24 5422

[25] W. Burian, J. Szade, Physical Review B 74, 113110 (2006)

[26] K. Inoue a,., y. Nakamura, A.V. Tsvyashchenko, L. Fomicheva, Journal of Magnetism and Magnetic Materials 140-144 (1995) 797-798

[27] Kazuko Inoue, Yoji Nakamura, A.V. Tsvyashchenko; Journal of the Physical Society of Japan; Vol. 64, No. 6, June, 1995, pp. 2175-2182

[28] Landolt-Bornstein, Group IV Physical Chemistry - Phase Equilibria, Crystallographic and Thermodynamic Data of Binary Alloys, Volume

[29] J. Lettieri, V. Vaithyanathan, S. K. Eah, J. Stephens, V. Sih, D. D. Awschalom, J. Levy, and D. G. Schlom; Applied Physics Letters, vol. 83, no 54 (2003)

[30]Iwata N., Pindoria G., Morishita T., Kohn K.; Journal of the Physical Society of Japan vol. 69, No. 1, pp 230-236, (2000)

[31] X. Wang, P. Liu, K A. Fox, J. Tang, J. Michael An, K. Belashchenko, and P.A. Dowben, submitted to IEEE Tran. Mag. as well as presentation GF-09 at the11th Joint MMM/Intermag Conference

[32] M. Coldeaa, M. Neuman, St. Lütkehoff, S. Mähl, R. Coldea; Journal of Alloys and Compounds, Volume 278, Issues 1-2, 1 August 1998, Pages 72-79

[33] D. Givord and R. Lemaire, IEEE Trans. Magn., MAG-10 (1974) 109.

[34] D. Givord and R. Lemaire, C.R. Acad. Sci., Paris, Ser. B274 (1972) 1166.

[35] D. Givord, F. Givord and R. Lemaire, J. Phys. Paris, 32 (1971) Cl-668.

[36] Laubschat C, Perscheid B and Schneider W-D 1983 Phys. Rev. B, Condens. Matter 28 4342.

[37] Schneider W-D, Laubschat C, Kalkowski G 1983 Phys. Rev. B, Condens. Matter 28 2017.

[38] Cho E, Oh S, Suga S, Suzuki T 1996 J. Electron Spectrosc. Relat. Phenom. 77 173

[39] Wieling S, Molodtsov S and Laubschat C 2002 Rev. B, Condens. Matter 65 075415

[40] T. B. Reed and R. E. Fahey Journal of Crystal Growth 8 (1971) 3 37—340

[41] Miedema AR 1976 J. Less-Common Met. 46 167.

[42] Hangil Lee and J.-Y. Kim, K.-J. Rho, B.-G. Park, and J.-H. Park, Journal of Applied Physics 102, (2007) 053903.

[43] J. Szade, M. Neumann, J. Phys.: Condens. Matter 13 (2001) 2717-272

[44] S. S. P. Parkin et al., Proc. IEEE 91, 661 (2003).

[45] B. X. Liu, W. S. Lai and Z. J. Zhang; Advances in Physics, 2001, Vol. 50, No. 4, 367-429.

[46] B. Ouladdiaf C. Ritter, R. Ballou, J Deportes; Physica B 276-278 (2000) 670-671

[47] A. Cho, "Film Deposition by Molecular Beam Techniques," J. Vac. Sci. Tech., Vol. 8, pp.S31-S38, 1971.

[48] Alfred Cho; Molecular beam epitaxy; American Institute of Physics, (1994).

[49] A. Cho, J. Arthur, "Molecular Beam Epitaxy," Prog. Solid-State Chem., Vol. 10, pp. 157 192, (1975.)

[50] B.A. Joyce, D.D. Vvedensky, T.S. Jones, M. Itoh, G.R. Bell, J.G. Belk, Journal of Crystal Growth 201/202 (1999) 106-112

[51] J.R. Arthur; Surface Science 500 (2002) 189–217

[52] Z. Celinski, J. Vac. Sci. Techn. A. 19, 383 (2001)

[53] Crystal growth of materials for energy production and energy-saving applications, R. Fornari, L. Sorba, Eds. (Edizioni ETS, Pisa, 2001)

[54] J. W. Hartman, R. T. Brewer and Harry A. Atwater, Journal of Applied Physica volume 92, number 9, 1 November 2002.

[55] U Korte, G Meyer-Ehmsen, Surface Science Volume 232, Issue 3, 2 June 1990, Pages 367-378.

[56] Claire Marton, Advances in electronics and electron physics, Academic Press, (1981).

[57] Stéphane Andrieu , Patrick Fréchard , Surface Science Volume 360, Issues 1-3, 10 July 1996, Pages 289-296.

[58] L. B. Freund, Subra Suresh; Thin film materials: stress, defect formation, and surface evolution; Cambridge University Press, (2003) .

[59] D. K. Schroder; Analytical and diagnostic techniques for semiconductor materials, devices, and processes; The Electrochemical Society, (2007).

[60] C. Suryanarayana, M. Grant Norton; X-Ray diffraction: a practical approach; Springer, (1998).

[61] E. J. Mittemeijer, Paolo Scardi; Diffraction analysis of the microstructure of materials; Springer, (2004).

[62] Mario Birkholz,Paul F. Fewster,Christoph Genzel, Thin film analysis by X-ray scattering, Wiley-VCH, 2006 – 356.

[63] A. Gibaud, S.Hazra X-ray reflectivity and diffuse scattering Current Science, Vol.78 No.12,25 June 2000.

[64] Jean Daillant, Alain Gibaud; X-ray and neutron reflectivity: principles and applications; Springer, (2009).

[65] Isao Kojima, Boquan Li Structural characterization of thin films by X-ray Reflcetivity The Rigaku Journal vol. 16 no. 2 (1999).

[66] Stefan Hüfner; Photoelectron spectroscopy: principles and application; Springer, (2003).

[67] David Briggs, M. P. Seah; Practical Surface Analysis: Auger and X-ray photoelectron spectroscopy; Wiley, (1990).

[68] David Briggs; Handbook of x-ray and ultraviolet photoelectron spectroscopy; Heyden, (1977).

[69] Ohn Clarke, Alexi Braginski; SQUID Handbook, The application of SQUIDS and SQUID systems, Volume 1; Wiley-VCH.

[70] Antonio Barone; Principles and applications of superconducting quantum interference devices; World Scientific, (1992).

[71] Dieter K. Schroder; Semiconductor material and device characterization; John Wiley and Sons, 2006, pp. 2-34.

[72] Sorin Cristoloveanu, Sheng S. Li; Electrical characterization of silicon-on-insulator materials and devices; Springer, (1995).

[73] S.M. Sze, Physics of Semiconductor Devices, 2nd ed. (John Wiley & Sons, (1981).

[74] K. Balin, J. Szade, A. J. Hutchison, A. Nowak, A. Gibaud, and Z. Celinski; J. Appl. Phys. 107, 09E154 (2010).

[75] Hangil Lee and J.-Y. Kim, K.-J. Rho, B.-G. Park, and J.-H. Park, Journal of Applied Physics 102, (2007) 053903.

[76] J. Szade, W. Burian, Z. Celiński, T. O'Keevan, M. Zangrando, F. Bondino, E. Magnano Surface Science 580 (2005) 163.

[77] Paweł Maślankiewicz, Zbigniew Celinski2 and Jacek Szade J. Phys.: Condens. Matter 20 315006 (2008).

[78] B. Vysotskii; Hyperfine Interactions Volume 28, Numbers 1-4, 1059-1062.

[79] A V Tsvyashchenko and V I Krylov; J. Phys.: Condens. Matter 2 4507 (1990).

[80] N. Mårtensson, F.U. Hillebrecht, D.D. Sarma; Surface Science Volumes 152-153, Part 2, April 1985, Pages 733-742.

[81] J A D Matthew et al J. Phys.: Condens. Matter 4 8489, (1992).

[82] W.A. Henle, M.G. Ramsey, F.P. Netzer, K. Horn , Surface Science Volume 254, Issues 1-3, 2 August 1991, Pages 182-190.

[83] K. Balin, A. Nowak, A. Gibaud, J. Szade, and Z. Celinski; Journal of Applied Physics 109, 07E323 (2011).

[84] F. Jiménez-Villacorta and Y. Huttel ; Journal of Applied Physics 101, 113914 2007

[85] M.D. Mukadam, S.M. Yusuf, P. Sharma, S.K. Kulshreshtha; Journal of Magnetism and Magnetic Materials 272–276 (2004) 1401–1403.

[86] P.J. Jensen, K.H. Bennemann ;/Surface Science Reports 61 (2006) 129–199.

[87] Lettieri et al.; Applied Physics Letters, Vol. 83, No. 5, 4 August 2003.

[88] P. Wachter, Handbook on the Physics and Chemistry of Rare Earths (K. A. Gschneidner and L. Eyring, Elsevier, Amsterdam, 1979), vol. 2, p. 507.

[89] Gourieux T, Frechard S, Dulot F, Eugene J, Kierren B and Malterre D, Physical Review B 62, 7502 (2000).

[90] W. Burian, J. Szade, T. O'Keevan and Z. Celiński; Physica Status Solidi (b) Volume 241, Issue 4, pages R15–R18, March 2004.

[91] X. Wang, P. Liu, K. A. Fox, J. Tang, J. A. Colón Santana, K. Belashchenko, P. A. Dowben, and Y. Sui, IEEE Trans. Magn. (in press).

[92] Hsu, J.H. ; Alten, B.G. ; Childress, J.R. ; Gavrin, A. ; Chien, C.L.; Journal of Applied Physics; (United States); Journal Volume: 70:10, 1991 Nov 15.

[93] Z. Kurant, R. Gieniusz, A. Maziewski,, M. Tekielak, W. Stefanowicz, I. Sveklo, V. Zablotskii, A. Petroutchik, L.T. Baczewski, A. Wawro; Journal of Magnetism and Magnetic Materials 316 (2007) e511–e514.

[94] O. Toulemonde, V. Petrov, A. Nait Abdi, and J. P. Bucher; Journal of Appllied Physics, vol 95, NUMBER 11 1 JUNE 2004.

[95] Thomas Duden and Ernst Bauer; Physical Review B, vol59, no 1 1 JJanuary (1999).

[96] E. Liu, J. Z. Zhang, W. Zhang, P. K. J. Wong, L. Y. Lv, Y. Zhai, J. Wu,2 Y. B. Xu, and H. R. Zhai; Journal of Applied Physics 109, 07C121 (2011).

[97] Subhankar Bedanta and Wolfgang Kleemann, J. Phys. D: Appl. Phys. 42 (2009) 013001 (28pp).

[98] M. Sasaki, P. E. Jönsson, and H. Takayama, PHYSICAL REVIEW B 71, 104405 (2005).

[99] C. M. Soukoulis, K. Levin, Gary S. Grest; Physical Review B 28, no 3 (1983).

[100] Y. Oner, C. S. Lue, Joseph H. Ross, Jr., K. D. D. Rathnayaka, and D. G. Naugle; Journal of Applied Physics, vol 89, 7044 (2001).

[101] URL: http://nanoscience.huji.ac.il/researchers/felner.htm

[102] J. Imry and S.-K. Ma, Physical Review Letters 21, 1399 (1975).

[103] D. Fiorani, et al., J. Magn. Magn. Mater. 196–197 (1999) 143.

[104] Y. Ying, J. M. Kim and Y. P. Lee, J. H. Kang; Journal of the Korean Physical Society, Vol. 58, No. 4, April 2011, pp. 969-972.

[105] Mahmud Khan, Igor Dubenko, Shane Stadler, and Naushad Ali; Journal of Applied Physics 102, 113914 (2007).

[106] S. Das, M. Patra, S. Majumdar, S. Giri, Journal of Alloys and Compounds 488 (2009) 27–30.

[107] J. Nogues, D. Lederman, T. J. Moran, and I. K. Schuller, Phys. Rev. Lett. 76, 4624 (1996).

[108] C. Leighton, J. Nogues, H. Suhl, and I. K. Schuller, Phys. Rev. B. 60, 12837 (1999).

[109] F. R. de Boer, R. Boom, W. C. M. Mattens, A. R. Miedema, A. K. Niessen, Cohesion in metals: transition metal alloys (Cohesion and structure, Vol. 1); North-Holland, Amsterdam – Oxford – New York – Tokyo, (1988).

[110] B. X. Liu, W. S. Lai, Z. J. Zhang, Adv. Phys. 50, 367 (2001).

[111] A W Weeber J. Phys. F: Met. Phys. 17 809 (1987).

[112] A.E. Clark in Ferromagnetic Materials, vol. 1, Ed. E.P. Wohlfart, North Holland, (1980).

[113] L. Shlapbach (Editor) Hydrogen in Intermetallic Compounds Springer Verlag, Topics in Applied Physics, vol. 63 and 64, (1992).

[114] Carey, R. Newman, D.M. Thomas, B.W.J. ; New Materials for Information Storage; 30 Apr 1991.

[115] Chaudhari, P., Cuomo, X X, Gambino, R. X, IBM J. Res. Dev. 17, 66, (1973).

6. Appendices

Appendix A: List of abbreviations.

ABBREVIATIONS	DEFINITION
AFM	Atomic Force Microscopy
CEMS	Conversion Electron Mössbauer Spectrometer
FM	Frank-van der Merwe
GMR	Giant Magneto Resistance
LEED	Low Energy Electron Diffraction
MBE	Molecular Beam Epitaxy
MFM	Magnetic Force Microscopy
MOKE	Magnetooptical Kerr Effect
RE	Rare Earth
RHEED	Reflection High Energy Electron Diffraction
SK	Stranski–Krastanov
SQUID	Superconducting Quantum Interference Device
TM	Transition Metal
TMO	Thermo-Magneto-Optical
TMR	Thermo-Magnetic Recording
VW	Wolmer-Veber
XMCD	X-ray Magnetic Circular Dichroism
XPS	X-ray Photoelectron Spectroscopy
XRD	X-ray Diffraction
XRR	X-ray Reflectivity

Appendix B: List of analyzed samples.

Where: * original designation of the sample,

** TM in this column represents selected transition metal Mn, Fe or Cr.

Sample symbol	Eu_xTM_y	Substrate	Total thickness**			Partial thickness **						
			Total	TM	Eu	TM	Eu	TM	Eu	TM	Eu	TM	Eu
A-Mn *276	$EuMn_2$	MgO	58.5	19.6	38.9	5.6	18.3	5.6	20.6	8.4	-	-	-
B-Mn *321	$EuMn_5$	Si+300Å of Mo	35	19.6	15.4	4.9	7.8	9.8	7.6	4.9	-	-	-
C-Mn *317	$EuMn_2$	Si+300Å of Mo	58.4	19.7	38.7	5.7	18.4	5.6	20.3	8.3	-	-	-
D-Mn *319	$EuMn_2$	Si+300Å of Mo	58.1	19.5	38.6	4.9	19.3	7.9	19.3	6.7	29.4	-	-
		Si+300Å of Mo	181.6	78.4	103.2	4.9	12.9	9.8	12.9	9.8	12.9	9.8	12.9
E-Mn *329	$EuMn_3$					-	12.9	9.9	12.9	9.8	12.9	9.7	12.9
								covered by 16.1Å of Cr					
		GaAs+300Å of Mo	307.6	210.2	97.4	5	4.1	8.8	4.4	8.7	3.7	8.7	4
						9	4.1	9.1	6	8.4	2.1	9	3.8
						8	4.3	8.9	4.5	8.5	4	8.7	3.6
F-Mn *374	EJu_2Mn_{17}					8.7	4.3	8.7	3.8	8.7	4.1	8.7	4
						8.7	6.2	8.7	2	8.7	4.3	8.7	4.1
						8.7	4.1	5	-	-	-	-	-
								covered by 11Å of Mo and 23.4Å of Au					
G-Mn *377	Eu_xMn_y	GaAs+300Å of Mo	300					co-deposition					
								covered by 4.1Å of Mo and 30Å of Au					
		MgO	436.4	298	138.4	25	23.2	49.5	22.3	49.9	23.5	49.7	22.2
H-Mn *307	Eu_2Mn_{17}					48.9	23.3	49.1	23.9	25.9	-	-	-
								covered by16Å of Au					
I-Mn *382	Eu_xMn_y	GaAs+300Å of Mo	200					co-deposition					
								covered by 34 Å of Au					
		GaAs+300Å of Mo	307.6	210.7	96.5	5.4	4.1	8.6	4	8.7	4.1	8.7	4.4
						8.7	4.4	8.7	3.5	8.7	4	8.7	4.1
						8.7	4.6	9.2	3.5	8.2	4	8.7	4.1
J-Mn *375	Eu_2Mn_{17}					8.5	4	8.8	5.4	8.6	2.8	9	4.2
						8.4	3.9	9.4	3.5	8.8	3.7	7.9	4.1
						8.7	4.1	5.1	-	-	-	-	-
								covered by 12.5Å of Mo and 23.5 Å of Au					

K-Mn *328	Eu_2Mn_{17}	Si+300Å of Mo	143.5	98	44.5	4.9	4.6	9.8	4.5	9.8	4.6	9.8	4.5
						9.8	4.6	9.8	4.5	9.8	4.6	9.8	4.5
						9.8	4.6	9.8	4.5	4.9	-	-	-
									covered by 20.4 Å of Cr				
L-Mn *327	$EuMn_5$	Si+300Å of Mo	140,1	78,4	61,7	4,9	7,8	9,9	7,9	9,7	7,6	9,8	7,6
						9.8	7,8	9,8	7,6	9.8	7,7	9,8	7,7
						4.9	-	-	-	-	-	-	-
									covered by 20.1 Å of Cr				
M-Mn *300	Eu_2Mn_{17}	MgO	266.7	182	84.7	8.4	4.2	8.5	4.2	8.3	4.4	8.4	4.1
						8.4	4.1	8.5	4.0	8.3	4.2	8.4	4.0
						8.6	4.0	8.4	4.2	8.6	4.0	8.2	4.1
						8.1	4.3	9.3	4.1	8.6	4.1	8.6	4.1
						8.6	4.1	8.6	4.1	8.6	4.1	10.3	6.3
						10.3	-	-	-	-	-	-	-
									covered by 10.4Å of Ag				
N-Mn *358	Eu_2Mn_{17}	Si+500Å of Mo	43.1	29.4	13.7	5.0	4.6	9.7	4.5	9.8	4.6	4.9	-
O-Mn *18	$EuMn_2$	Si+35Å of Mo	103.9	68.6	35.3	4.9	19.4	9.8	19.3	9.8	19.3	9.8	19.3
						9.8	19.3	9.8	19.3	9.8	19.3	4.9	-
									covered by 40Å of Mo				
"P-Mn" *283	EuMn	MgO	96.8	19.5	77.3	-	25.7	8.3	24.7	11.2	27.9	-	-
		Si+500Å of Mo	248.6	190	58.6	5.9	3.1	9.9.	3.1	9.9	3	10	3.1
						9.9	3.0	9.9	3.2	9.9	3.0	9.9	3.1
						9.9	3.5	9.9	2.9	9.9	3.1	10	3.1
"R-Mn" *371	$EuMn_5$					10.2	3.2	9.7	2.9	10.4	3.1	9.7	3
						9.9	3.1	10.3	3.1	9.7	3.3	9.7	2.7
						5.3	-	-	-	-	-	-	-
									covered by 4.6Å of Au and 29 Å of Au				
A-Fe *334	Eu_2Fe	Si+500Å of Mo	88.2	10.1	78.1	2.5	39.1	5	39	2.6	-	-	-
B-Fe *344	Eu_2Fe_{17}	Si+500Å of Mo	146.5	101	45.9	2.8	2.3	5	2.6	5	2.2	5	2.2
						5	2.2	5	2.5	5.1	2.3	5	2.3
						5.1	2.3	5	2.3	5.1	2.3	5	2.4
						5.2	2.2	4.9	2.3	5	2.3	5	2.3
						5.21	2.2	5	2.3	5	2.3	5	2.3

						2.6	-	-	-	-	-	-	-
						covered by 20.6 Å of Au							
		Si+500Å of Mo	161.2	90.9	70.3	2.6	3.9	5	3.9	5	3.9	5.1	3.9
						3.9	5.2	3.9	5	3.9	5	3.8	4
C-Fe *348	$EuFe_5$					5.2	4	5	3.9	5.2	3.8	5	4
						5	4.3	5	4.3	5	3.8	5	3.8
						5	3.8	-	-	-	-	-	-
						covered by 12 Å of Mo and12.9 Å of Au							
		Si+500Å of Mo	147.5	30.3	117.2	2.9	19.6	5	19.5	4.9	19.5	5	19.8
D-Fe *353	EuFe					5	19.5	5	19.3	2.6	-	-	-
		covered by 20.4Å of Au											
E-Fe *384	Eu_xFe_y	Si+500Å of Mo	100	co-deposition									
		covered by 45.1Å of Au											
		Si+500Å of Mo	115.4	50.5	64.9	3.1	6.5	4.6	6.5	5.1	6.5	5.1	6.5
F-Fe *352	$EuFe_3$					5.0	6.5	5.0	6.6	5.0	6.4	5.1	6.8
						4.9	6.2	5.0	6.4	2.6	-	-	-
		covered by 22.1 Å of Au											
		Si+500Å of Mo	176.5	20.3	156.2	2.5	39.0	5.0	39.1	5.0	39.1	5.1	39.0
G-Fe *347	Eu_2Fe					2.7	-	-	-	-	-	-	-
		covered by 0.8Å of Mo and 20.4Å of Au											
			222.3	75.8	146.5	2.6	9.7	5	9.8	5	9.8	5.1	9.8
						5	10	5	9.5	5.1	9.8	5.1	9.9
H-Fe *385	$EuFe_2$					5	9.6	5	9.7	5	9.8	5	9.8
						5	9.8	5	9.7	5.1	9.8	2.8	
		covered by 30.5Å of Au											
I-Fe *19	Fe_xO_y	Si+20 Å of Mo		10		10 Å thick Fe grown on Si+20 Å of Mo has been oxidized and later covered by additional 20 Å thick layer of Mo							
		covered by 30.5Å of Au											
A-Cr *336	$EuCr_5$	GaAs+300Å of Mo	36.3	20.2	16.1	5.3	8.1	9.9	8	4.9	-	-	-
B-Cr *337	Eu_2Cr_{17}	GaAs+300Å of Mo	29.7	20.2	9.5	5.1	4.8	10.1	4.7	5	-	-	-
C-Cr *338	Eu_2Cr	GaAs+300Å of Mo	90.9	10.1	80.8	2.5	40.4	5	40.4	2.6	-	-	-
D-Cr *339	EuCr	GaAs+300Å of Mo	49.7	10.1	39.6	2.5	20.9	5	19.5	2.6	-	-	-
E-Cr *340	$EuCr_2$	GaAs+300Å of Mo	45.4	25.2	20.2	2.5	10.1	5	10.1	2.6	15.1	-	-

F-Cr *355	EuCr	GaAs+300Å of Mo	151.5	30.3	121.2	2.6	20.2	5	20.4	5.1	20	5	20.2
						5.1	20.2	4.9	20.2	2.6	-	-	-
		covered by 20.7Å of Au											
G-Cr *356	$EuCr_2$	GaAs+300Å of Mo	121.2	40.9	80.3	2.7	10.1	5.0	10.3	5.0	9.9	5.1	10.1
						5.0	10.2	5.1	10.0	5.0	10.1	5.0	10.1
						2.6	-	-	-	-	-	-	-
		covered by 7.7Å of Mo and 17.8Å of Au											
H-Cr *354	Eu_2Cr	GaAs+300Å of Mo	181.8	20.2	161.6	2.7	40.5	5	40.4	5	40.4	5	40.3
						2.3	-	-	-	-	-	-	-
		covered by 20.9Å of Au											

Appendix C: List of figures

Appendix D: List of tables

Appendix E: Binary Diagrams for Eu-TM system

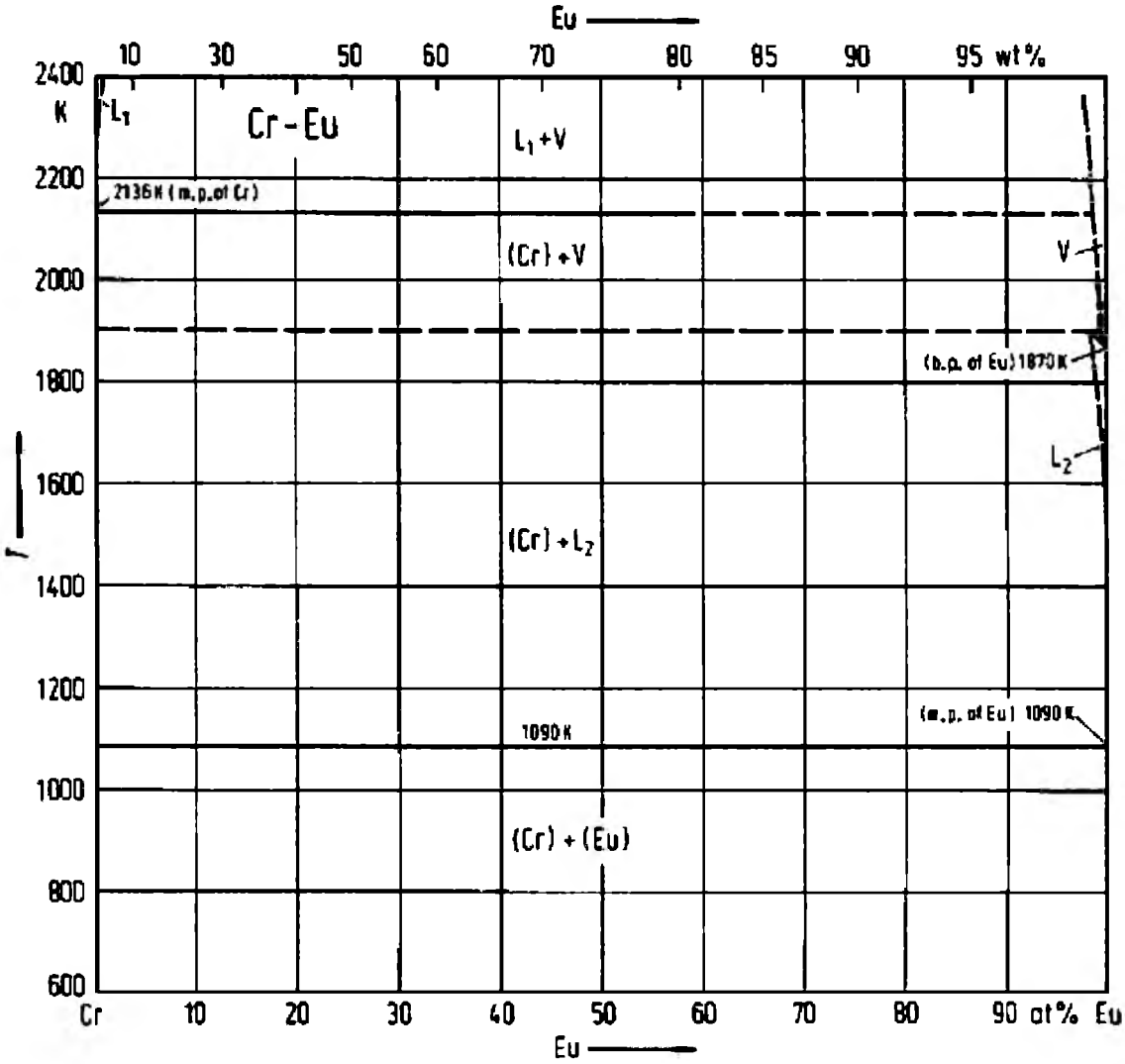

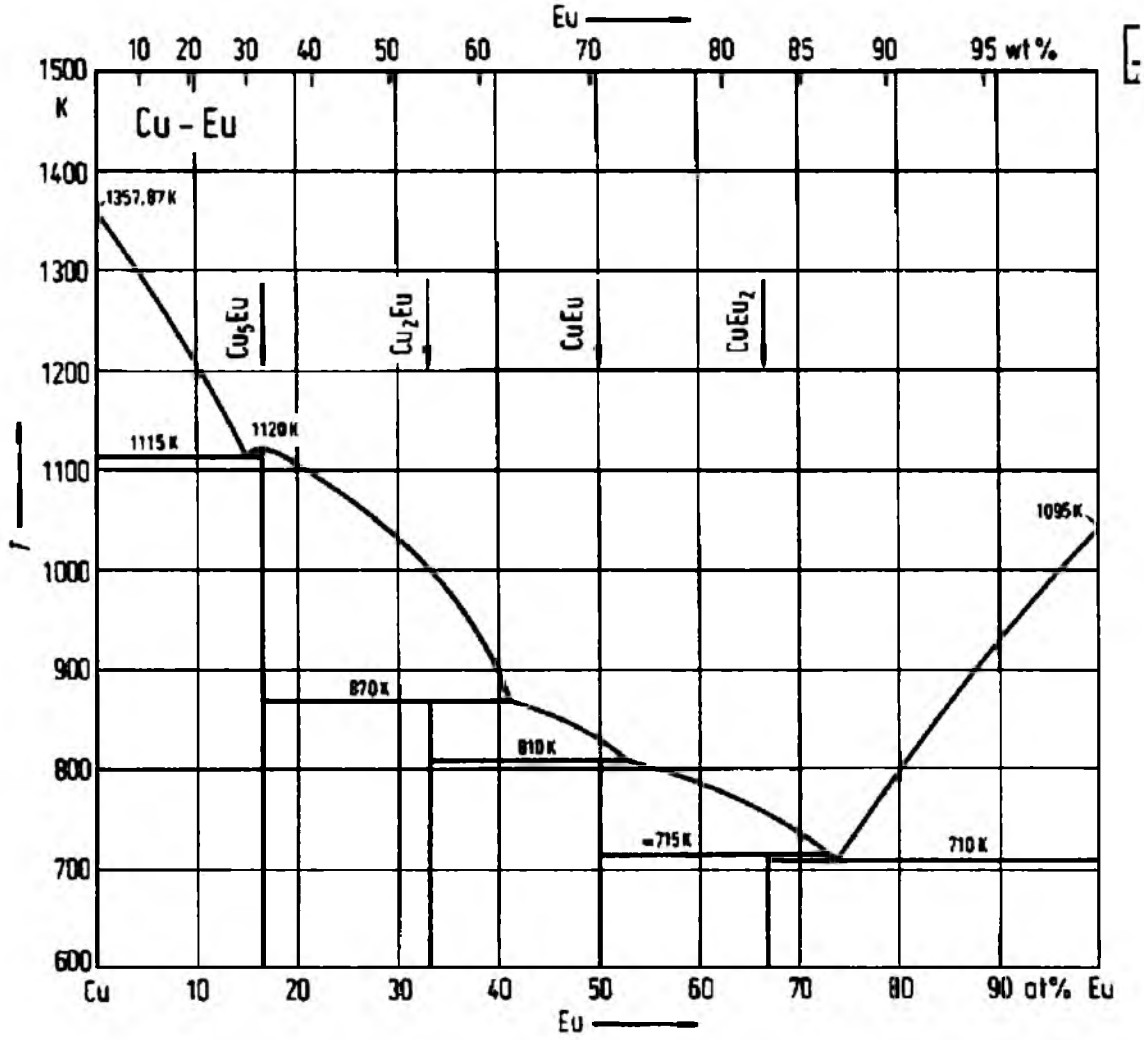
Eu
10 20 30 40 50 60 70 80 85 90 95 wt %
1500
K
Cu - Eu
1400
1357.87K
1300
Cu5Eu
Cu2Eu
CuEu
CuEu2
1200
1115K
1120K
1100
1095K
T
1000
900
870K
810K
800
715K
710K
700
600
Cu 10 20 30 40 50 60 70 80 90 at% Eu
Eu

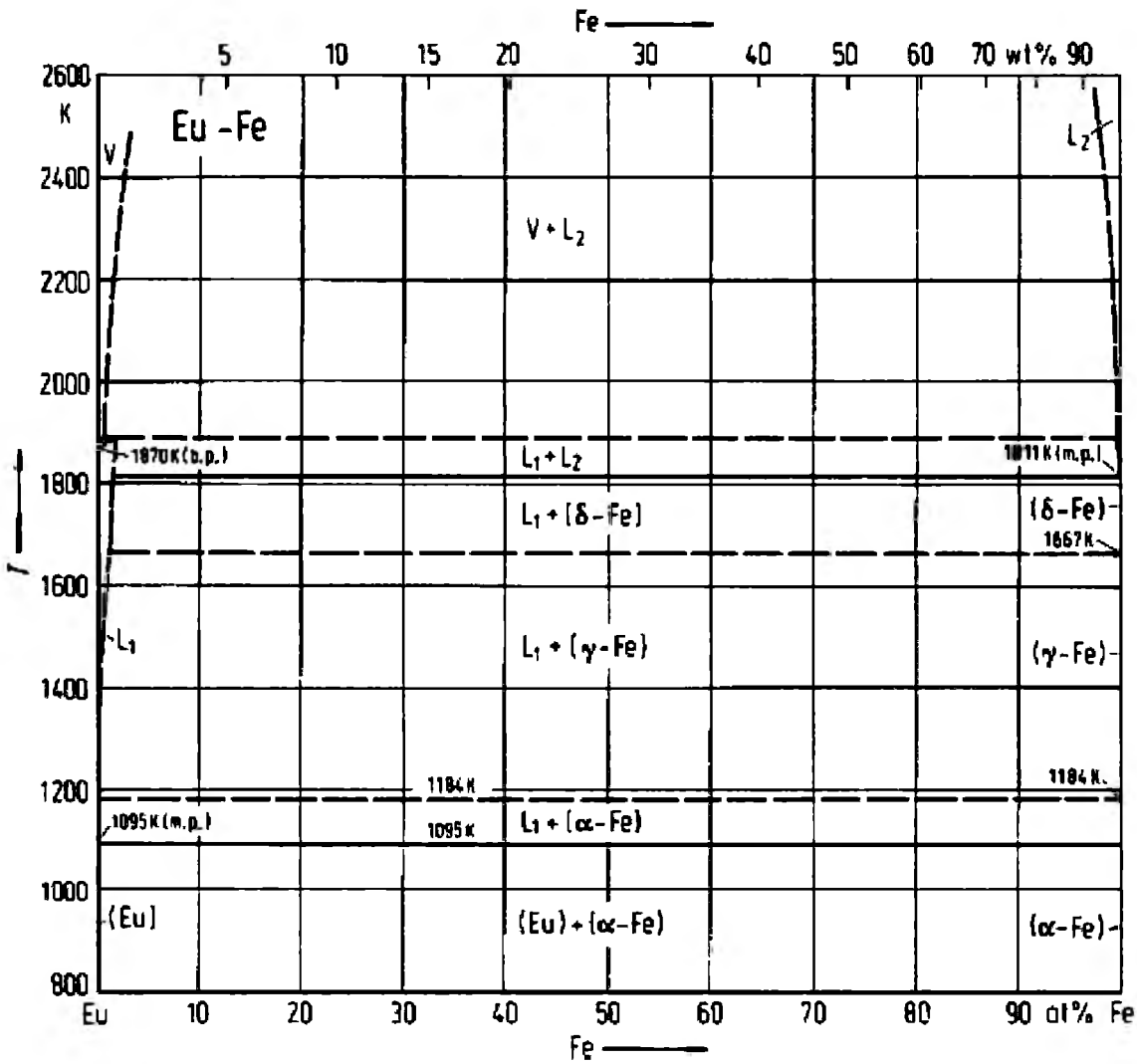
Fe
5
10
15
20
30
40
50
60
70 wt% 90
2600
K
2400
2200
2000
1800
1600
1400
1200
1000
800
T
Eu - Fe
V
L2
V + L2
1870K (b.p.)
L1 + L2
1811K (m.p.)
L1 + (δ-Fe)
(δ-Fe)
1667K
L1
L1 + (γ-Fe)
(γ-Fe)
1184K
1184K
1095K (m.p.)
1095K
L1 + (α-Fe)
(Eu)
(Eu) + (α-Fe)
(α-Fe)
Eu
10
20
30
40
50
60
70
80
90 at% Fe
Fe

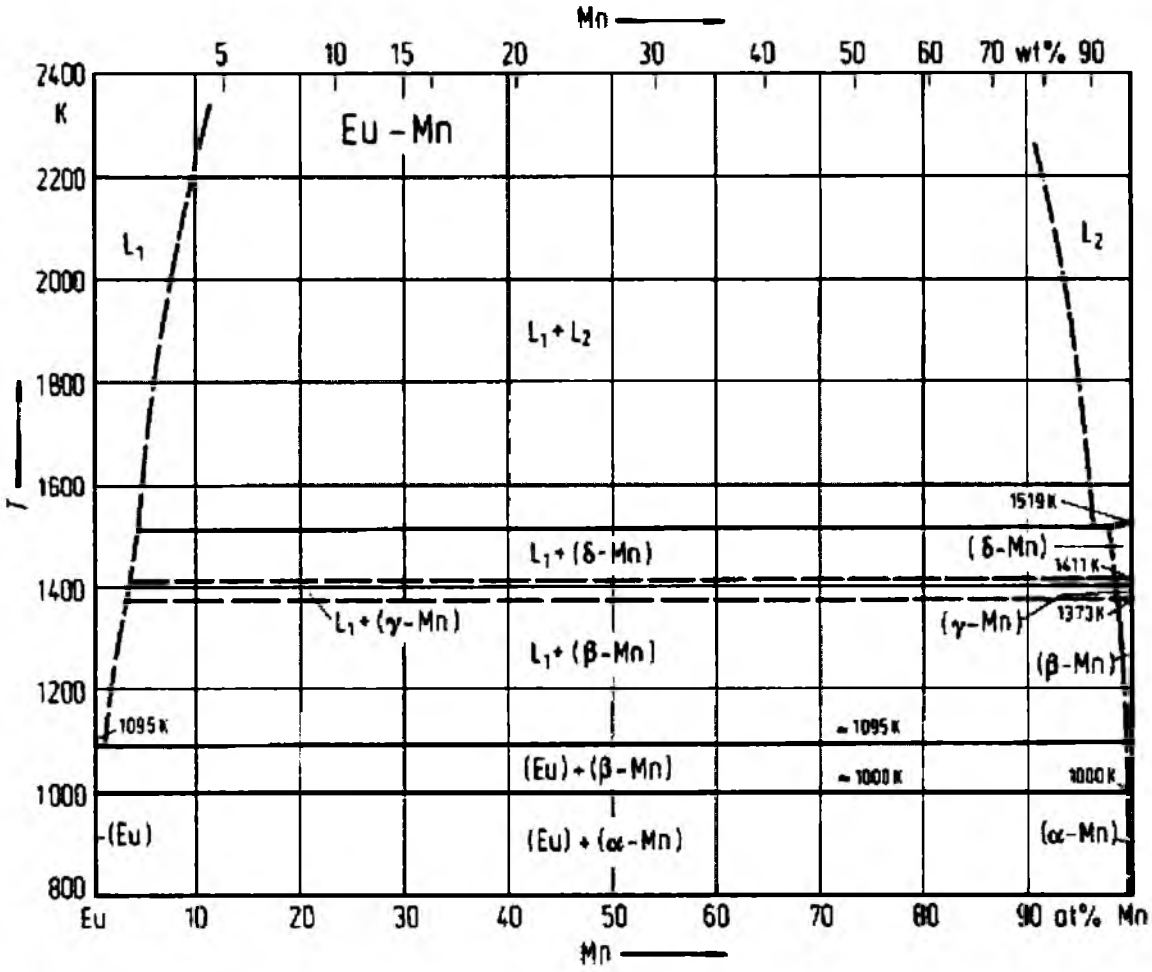
Mn
5
10
15
20
30
40
50
60
70 wt% 90
2400
K
2200
2000
1800
1600
1400
1200
1000
800
T
Eu - Mn
L1
L2
L1 + L2
L1 + (δ-Mn)
(δ-Mn)
1519 K
1411 K
L1 + (γ-Mn)
(γ-Mn)
1373 K
L1 + (β-Mn)
(β-Mn)
1095 K
≈ 1095 K
(Eu) + (β-Mn)
≈ 1000 K
1000 K
(Eu)
(Eu) + (α-Mn)
(α-Mn)
Eu
10
20
30
40
50
60
70
80
90 at% Mn
Mn

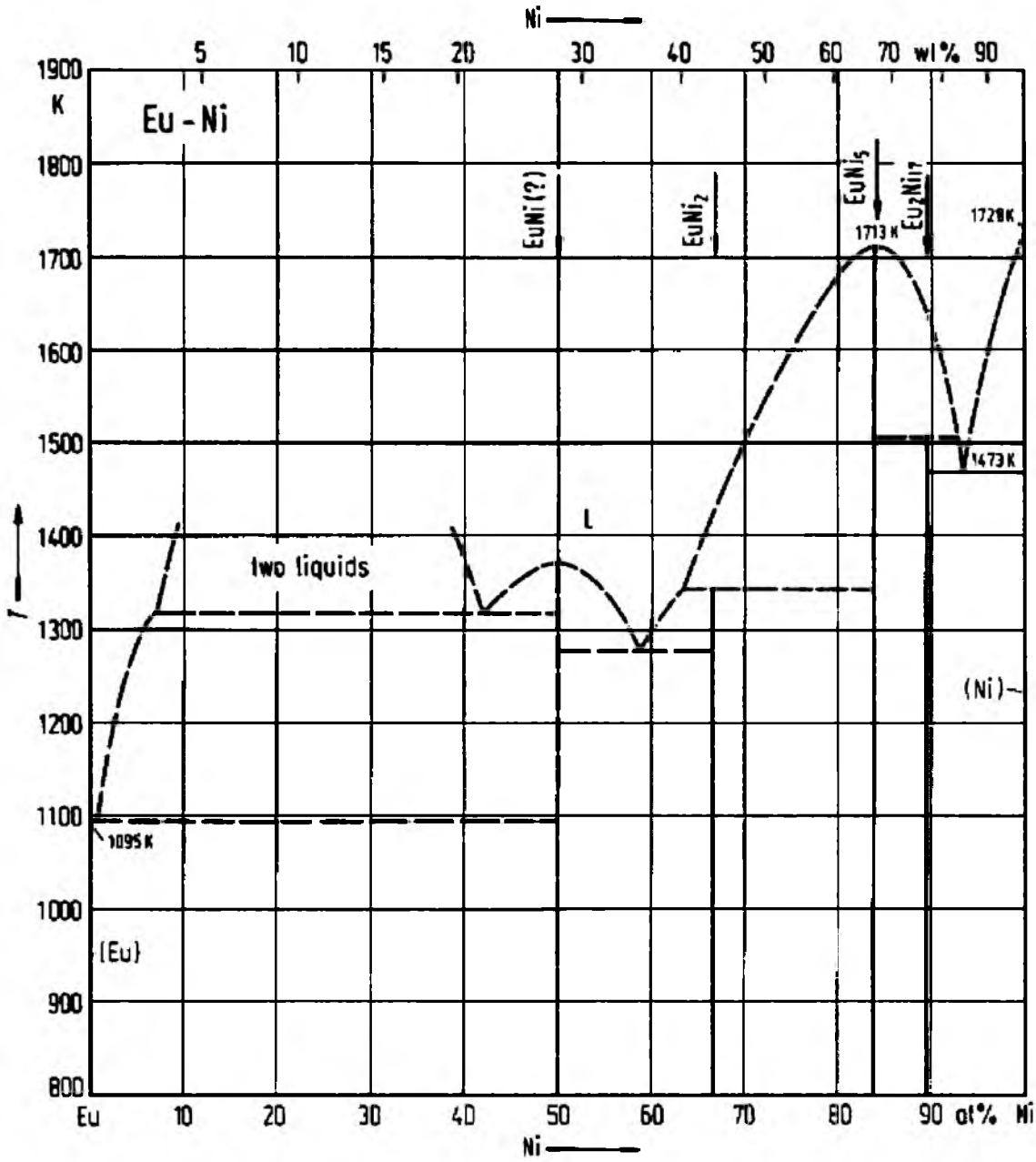
Ni
5 10 15 20 30 40 50 60 70 wt% 90
1900 K
1800
1700
1600
1500
1400
1300
1200
1100
1000
900
800
Eu - Ni
EuNi(?)
EuNi2
EuNi5
Eu2Ni17
1729K
1713 K
1473K
L
two liquids
(Ni)
1095K
(Eu)
Eu 10 20 30 40 50 60 70 80 90 at% Ni
Ni

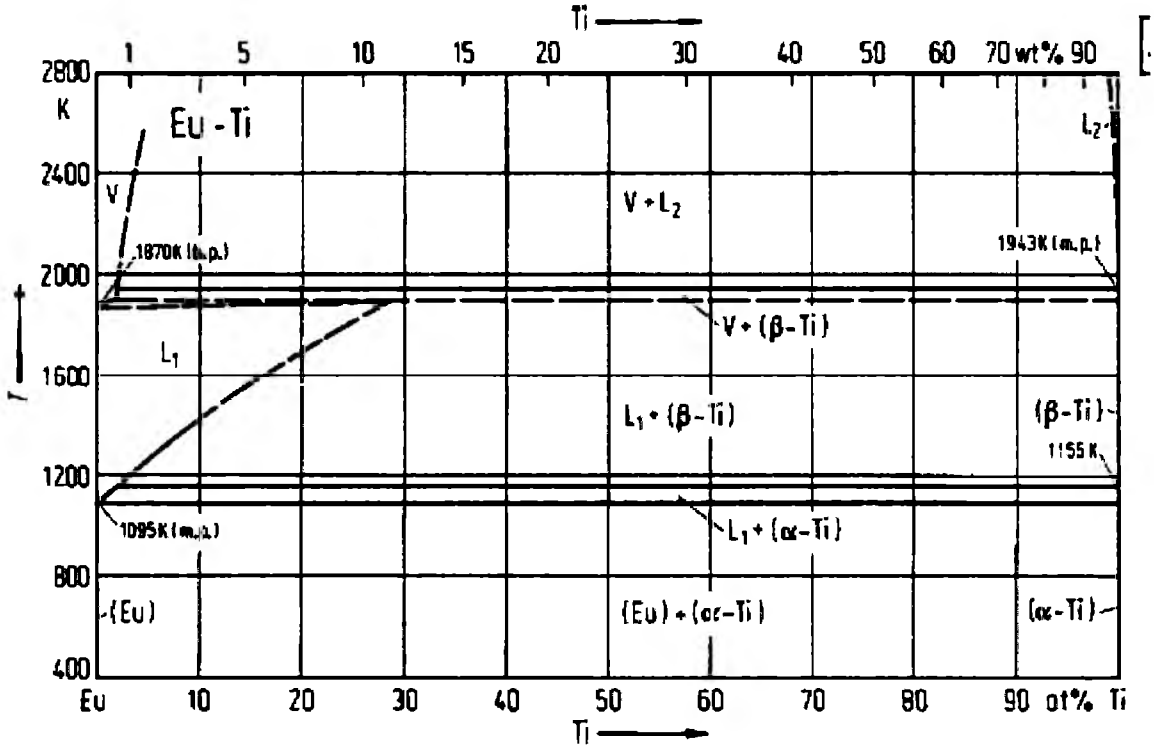
Ti
1 5 10 15 20 30 40 50 60 70 wt% 90
2800 K
2400
2000
1600
1200
800
400
Eu - Ti
V
V + L2
L2
1870K (m.p.)
1943K (m.p.)
L1
V + (β-Ti)
L1 + (β-Ti)
(β-Ti)
1155K
1095K (m.p.)
L1 + (α-Ti)
(Eu)
(Eu) + (α-Ti)
(α-Ti)
Eu 10 20 30 40 50 60 70 80 90 at% Ti
Ti

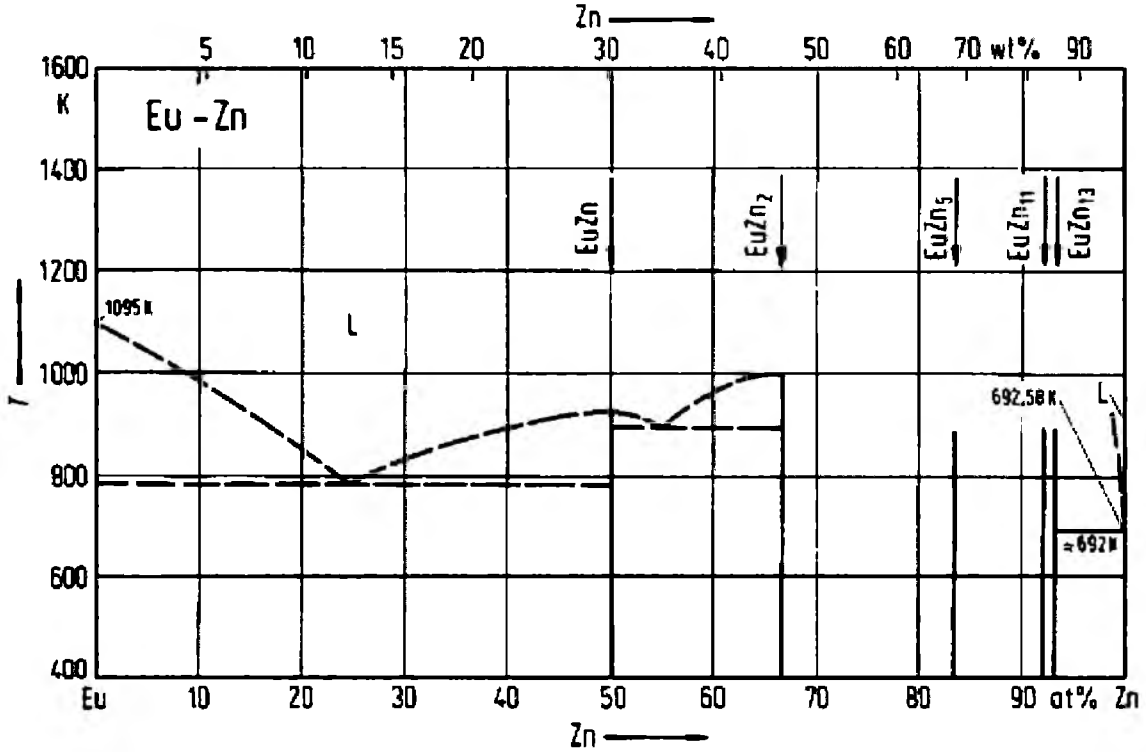
Zn
5 10 15 20 30 40 50 60 70 wt% 90
1600 K
1400
1200
1000
800
600
400
Eu - Zn
EuZn
EuZn2
EuZn5
EuZn11
EuZn13
1095 K
L
692.58K
L1
≈692K
Eu 10 20 30 40 50 60 70 80 90 at% Zn
Zn

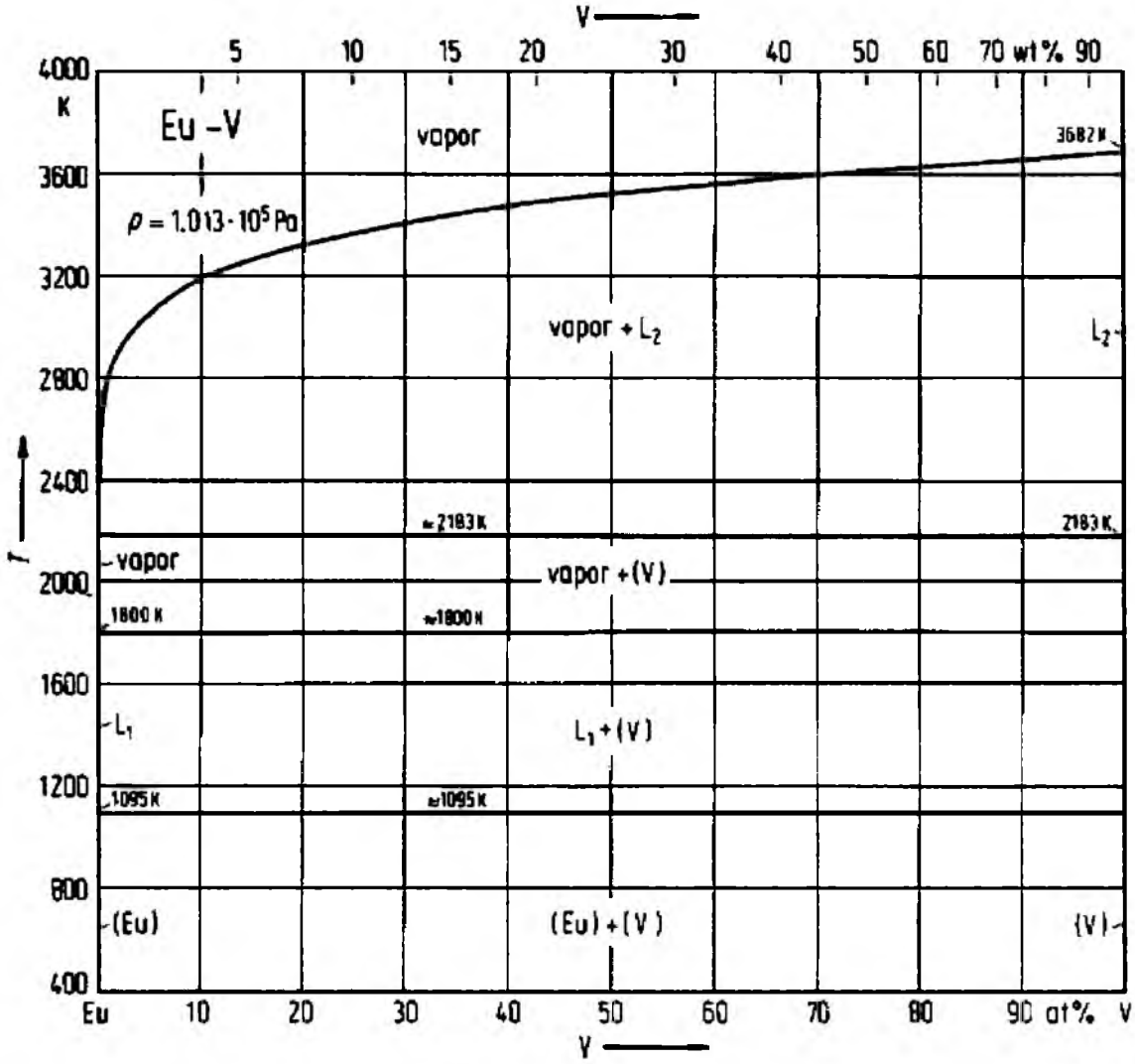
V
5
10
15
20
30
40
50
60
70 wt% 90
4000
K
3600
3200
2800
2400
2000
1600
1200
800
400
T
Eu –V
vapor
3682 K
p = 1.013 · 10⁵ Pa
vapor + L2
L2
≈2183 K
2183 K
vapor
vapor + (V)
1800 K
≈1800 K
L1
L1 + (V)
1095 K
≈1095 K
(Eu)
(Eu) + (V)
(V)
Eu
10
20
30
40
50
60
70
80
90 at% V
V

Appendix F: Published Work, Conference Presentations, Seminars

Bolded are associated with the PhD thesis.

1. **K. Balin. A. Nowak. A. Gibaud. J. Szade. and Z. Celinski; *Properties of molecular beam epitaxy grown Eu_x(transition metal)$_y$ films (transition metals: Mn. Cr)*; Journal of Applied Physics v.109. 2011. p. 07E323.**
2. Nie. Yan; Harward. I.; Balin. K.; Beaubien. A.; Celinski. Z.; *Preparation and characterization of barium hexagonal ferrite thin films on a Pt template*; Journal of Applied Physics. Volume 107. Issue 7. pp. 073903-073903-5 (2010).
3. **K. Balin. J. Szade. A. J. Hutchison. A. Nowak. A. Gibaud. and Z. Celinski. *Electronic structure. crystallographic. magnetic. and transport characterization of $EuMn_2$ films*; Journal of Applied Physics. v.107. 2010. p. 09E154.**
4. J Pištora. M Lesňák. E Lišková. Š Višňovský. I Harward. P Maslankiewicz. K Balin. Z Celinski. J Mistrík. T Yamaguchi. R Lopusnik and J Vlček; *The effect of FeF_2 on the magneto-optic response in FeF2/Fe/FeF2 sandwiches*; J. Phys. D: Appl. Phys. 43 155301 (2010).
5. S. Widuch. Z. Celinski. K. Balin. R. Schafer. L. Schultz. D. Skrzypek. J. McCord; *Variation in ferromagnetic domain density and domain asymmetry in Fe/FeF_2 exchange bias structures*. Physical Review B vol 77. n 18. 184433 (2008).
6. A.Winiarski. K.Balin. W.Moras. J.Heimann and E.Teper. *Crystal structure and some physical properties of $BaPb_{0.7-x}M_xBi_{0.3}O_{3-\delta}$ (M = In. Sb)*. Acta Crystallographica A63 (2007) 224-225.
7. **European Conference on Surface Science, ECOSS28; *Magnetic properties of MBE Grown Eu-Fe Films*; (K. Balin. A. Nowak . J. Szade. and Z. Celinski);28.08.11-02.09.11 Wrocław.**
8. **X Katowicko-Krakowskie Seminarium „Fizyka Fazy Skondensowanej"; *Właściwości ultracienkich warstw EuTM (TM = Mn. Fe)* (K. Balin. A. Nowak. J. Szade. Z. Celinski); 20-21.05.2011 Kraków.**
9. **TEAM workshop; *Growth and Characterization of Eu-Fe Films.* (K. Balin. J. Szade. A. Nowak. P. Gibaud. Z.J. Celinski); 12-16.04.10 Zakopane.**

10. **55th Annual Conference on Magnetism and Magnetic Materials; *Properties of MBE Grown EuxTMy Thin Films (TM=Mn. Cr)* (K. Balin. J. Szade. A.J. Hutchison. A. Nowak. P. Gibaud. Z.J. Celinski); 14-18.11.10 Atlanta, USA.**
11. **IEEE 7th International Symposium on Metallic Multilayers; *Characterization of Eu_xTM_y (TM=Mn. Cr) films grown by MBE.* (K. Balin. J. Szade. A.J. Hutchison. A. Nowak. P. Ruello. Z.J. Celinski) ; 19-24.09.10 Berkley, USA.**
12. **European Conference on Surface Science ECOSS27; *Growth and Characterization of Eu_xTM_y thin films (TM=Mn. Fe. Cr)* (K. Balin. J. Szade. .J. Hutchison. A. Nowak. P. Ruello. Z.J. Celinski); 30.08.10 – 05.09.10 Groningen, Holandia.**
13. **IX Katowicko-Krakowskie Seminarium „Fizyka Fazy Skondensowanej" *Strukturalne i magnetyczne własności nowych cienkowarstwowych związków międzymetalicznych Eu_xTM_y (TM = Mn. Fe. Cr);* 11-12.06.10 Rychwald.**
14. **11th Joint MMM/Intermag Conference; *Electronic structure. crystallographic. magnetic and transport characterization of EuMn2 films.*(K. Balin. J. Szade. .J. Hutchison. A. Nowak. P. Ruello. Z.J. Celinski); 18-22.01.10 Washington, USA.**
15. 11th Joint MMM/Intermag Conference; *Dynamic exchange anisotropy for exchange bias structures: Fe/KNiF3. Fe/MnF2 and Fe/FeF2.* (S.Widuch. N.Yan. K. Balin. R.L. Stamps i Z. Celinski); 18-22.01.10 Washington, USA.
16. 11th Joint MMM/Intermag Conference; *Magnetic characterization of hexagonal ferrite thin films grown by metallo-organic decomposition on a Pt template.* (I.R. Harward. Y. Nie. K. Balin. A. Beaubien i Z.J. Celinski); 18-22.01.10 Washington, USA.
17. Gliwice Scientific Meetings; *Zinc Octacarboxyphthalocyanine – a possible photosensitizer for photodynamic therap;* (B.Boroń; A. Szurko; M. Rams; A.Sochanik; R. Wrzalik; Z. Ujma; J. Nackiewicz. K. Balin; A. Ratuszna); 20-21.10.09, Gliwice.
18. **53rd Annual Conference on Magnetism and Magnetic Materials; *Electronic Structure. Magnetic and Transport Characterization of Eu - Mn Intermetallic Alloys.*(K. Balin. J. Szade. .J. Hutchison. Z. Celinski) 10-14. 11.08. Austin, USA.**
19. **IEEE Magnetic Society Summer School; *Electronic Structure of Europium - Manganese Alloys.* (K. Balin. J. Szade. A.J. Hutchison. Z. Celinski) 3-8. 08.08; Colorado Springs, USA.**